TOPICS IN THE THEORY OF GLASSES

A dissertation presented to
the faculty of
the College of Arts and Sciences of Ohio University

In partial fulfillment
of the requirements for the degree
Doctor of Philosophy

De Nyago Tafen
August 2005

This dissertation entitled

TOPICS IN THE THEORY OF GLASSES

BY

De Nyago Tafen

has been approved for
the Department of Physics and Astronomy
and the College of Arts and Sciences of Ohio University by

David Drabold
Professor of Physics and Astronomy

Benjamin M. Ogles
Interim Dean, College of Arts and Sciences

TAFEN, DE NYAGO. Ph.D. August 2005. Department of Physics and Astronomy

Topics in the Theory of Glasses (140pp.)

Director of dissertation: David Drabold

In this work, we present the results of large scale computer simulations using different approaches ranging from the usual quench from the melt to the building blocks method. We also present structural models of binary chalcogenide glasses, $GeSe_4$, $GeSe_9$, $GeSe_{1.5}$, $GeSe_2$ and $SiSe_2$, amorphous silica and models of Ge-Se glasses heavily doped with Ag $(GeSe_3)_{0.90}Ag_{0.10}$, $GeSe_3)_{0.85}Ag_{0.15}$ through *ab initio* molecular dynamics simulation. $GeSe_4$ and $GeSe_9$ models are in good agreement with all the structural properties, vibrational properties and electronic density of states. The defect sites causing localization of electronic eigenstates in the band gap region are characterized. A detailed analysis of the atomic structure of these glasses shows that the Ge-centered tetrahedra are the predominant coordination motifs in g-$GeSe_4$ and that the structure of g-$GeSe_9$ consists of Se-chain segments which are cross-linked by $Ge(Se_{1/2})_4$ tetrahedra.

Having reliable models of $(GeSe_3)_{0.90}Ag_{0.10}$ and $(GeSe_3)_{0.85}Ag_{0.15}$, we study the dynamics of the network of these glasses with an emphasis on the Ag ions. We highlight the existence of trapping centers and explicitly illustrate the trapping and release process from thermal MD simulation. We show that first principles simulation is a powerful tool to reveal the motion of ions in glass. The models appear to be in excellent agreement with an array of experiments and should be useful for subsequent studies of these interesting materials.

For certain binary IV-VI glasses, especially silica, we show that decoration of bond-centered column VI atoms on tetrahedral amorphous networks leads with appropriate re-scaling and relaxation to highly realistic models of IV-VI binary glasses. The

models obtained present some additional features such as a proper asymptotic behavior in S(Q) for large Q. The method is used to produce other models such as $GeSe_2$ and $SiSe_2$. We also show that the combination of a reverse Monte Carlo approach with approximate first-principles molecular dynamics is effective for a challenging material g-$GeSe_2$.

Approved:

David Drabold
Professor of Physics and Astronomy

To my mother, brothers, sisters, wife, and late father

Acknowledgments

First and foremost I would like to thank my creator for the many experiences that he has brought me through and to, words cannot express my thankfulness. Special thanks to my advisor, Dr. David Drabold, for his patience, dedication, commitment, guidance and rigor. I was extremely lucky to find an advisor who can take on the multiple roles of editor, friend and mentor.

My warm thanks to Dr. Normand Mousseau for his inputs and helpfull discussions. I would like to thank Dr. J. C. Phillips and Dr. M. Mitkova for their helpful comments and insights, particularly in the area of silver diffusion. Thank you to my dissertation committee, Drs Ingram, Hla, Castillo and Butcher, for their constructive comments. My profound gratitude to Dr. Partha for countless stimulating discussions and for his help with the RMC code. My gratitude to Ray Atta-fynn and Tesfaye Abtew for their help and discussions. My thanks to Ohio University for giving me the opportunity to accomplish my Ph.D., especially the Physics Department including faculty, staff, and peers. I would like to acknowledge the support of the NSF and Axon Technologies, Inc. Warm thanks to Dr. J. M. B. Ndjaka, professor of physics at the University of Yaounde I. Special thanks to my amazing wife, Denise Hughes-Tafen, who has been with me every step along the way. Thanks for your patience, love and encouragement. Thanks to my extended family including Goldine Dickenson, Yvonne Gordon, Dr. Balde, Ayanna Jordan, Kelly Vassel, Youssouf Diallo, Gerard Akindes, Beidy Sow, Tyrone Carr, and Akil Houston for their friendship and support. Finally I would like to thank my mother, brothers, sisters, aunts. Their love and creativity were and will always be a constant source of my life.

Table of Contents

List of Figures

List of Tables

Chapter 1

Introduction

1.1 Amorphous Materials and Glasses

Nearly all materials (except elemental metals) can, if cooled fast enough and far enough, be prepared as amorphous solids. By definition, an amorphous solid is a material which is topologically disordered (positions of the atoms no longer coincide with a crystalline lattice) and does not possess the long-range translational (periodicity) characteristic of a crystal. A glass is an amorphous solid which exhibits a glass transition. In the literature these two terms are often interchangeable.

The lack of long-range order in amorphous materials does not imply randomness in the entire material, but randomness at large separations. On a shorter length-scale (0 - 5 Å) there exists a high degree of local order, namely short range order (SRO). Beyond the SRO, there may be an intermediate range order (IRO), also termed medium-range order (MRO), occurring at about 5 - 20 Å. In general, the SRO is associated with the nearest-neighbor environment of atoms. In covalently bonded materials, the SRO is well defined and characterized by the nearest-neighbor bond length, coordination number and bond angle. The absence of translational periodicity makes it impossible to extract atomistically detailed structure information and physical properties (e.g. atomic diffusion) from diffraction experiments. In that cases, computer simulations may be the only way to acquire the necessary information. Computer simulations are also useful to *predict* new structures of materials and their properties.

1.2 Chalcogenide Amorphous Materials

Chalcogenide amorphous semiconductors are disordered materials containing one or more of the chalcogen elements, S, Se, or Te from column VI. The chalcogenide glasses are preferred amorphous semiconductors for applications. They have well defined niches in fiber optics[1], optical recording[2], phase change memory[3], and other technological uses. Ge-Se glasses have been particularly studied because of their ready glass formation, easy synthesis requirements, high transformation temperature and chemical stability. The basic structural units are Se chains and Ge-Se tetrahedra, that depending on the Ge content, could be combined into corner sharing, edge sharing, ethane-like or distorted rock-salt structure to form network glass that in some cases self-organize[4]. This system was one of the first in which formation of an intermediate phase has been demonstrated[5]. The intermediate phase is characterized by a vanishing non-reversing heat-flow (i.e. a vanishing latent heat of melting), suggesting that glass compositions in this phase are configurationally close to their liquid counterparts, i.e. self-organized. In binary Ge_xSe_{1-x} glasses, the self-organized phase extends in the $0.20 < x < 0.254$ range, with glasses at $x < 0.20$ regarded as floppy while those at $x > 0.26$ are stressed rigid. In the self-organized phase, it is suggested that the backbone consists of corner-sharing (CS) $GeSe_4$ and edge sharing (ES) $Ge(Se_{1/2})_4$ tetrahedra. Raman mode-frequencies of CS and ES tetrahedra vary sub-linearly. A peculiarity of these local structural units is that a count of mechanical constraints due to bond-stretching and bond-bending forces per atom (n_c) exactly equals 3, the degrees of freedom associated with an atom in a 3D network. That match between n_c and the dimensionality of the network has consequences to the physical behavior of the backbone in the $0.20 < x < 0.254$ range. Dynamic calorimetry studies on the intermediate phase have suggested that it does not age[6], a feature that is likely to be of importance in application of these materials.

1.3 Structural Analysis Methods

1.3.1 Structural correlation function

The structure of simple monoatomic amorphous materials is characterized by a set of distribution functions for the atomic positions. The simplest of these is the pair correlation function $g(r)$. This function describes the probability of finding a pair of atoms a distance r ($\vec{r} = \vec{r_i} - \vec{r_j}$) apart, relative to the probability expected for a completely random distribution at the same distance. One can write the correlation function in the following form:

$$g(r) = \rho^{-2}\langle \sum_i \sum_{i \neq j} \delta(\vec{r_i})\delta(\vec{r_j} - \vec{r})\rangle = \frac{V}{N^2}\langle \sum_i \sum_{i \neq j} \delta(\vec{r} - \vec{r_{ij}})\rangle \tag{1.1}$$

where N is the number of particles in the system; $\rho = \frac{N}{V}$ is the number density. Taking the angular average of Eq. 1.1 we get:

$$\begin{aligned} g(r) &= \frac{V}{4\pi N^2} \sum_i \sum_{i \neq j} \int d\theta d\phi \frac{1}{r r_{ij}} \delta(r - r_{ij})\delta(\theta - \theta_{ij})\delta(\phi - \phi_{ij}) \\ &= \frac{V}{4\pi r^2 N^2} \sum_{i \neq j} \delta(r - r_{ij}) \end{aligned} \tag{1.2}$$

For a crystal lattice with each atomic nucleus frozen in its equilibrium position, $g(r)$ is a sum of delta functions, with each term corresponding to a coordination shell. In the case of amorphous materials, $g(r)$ exhibits its major peak close to the average atomic separation of neighboring atoms. With increasing r, $g(r)$ exhibits damped oscillations which rapidly merge to 1 reflecting a lack of long-range spatial correlation.

The pair correlation function is widely used to characterize, albeit incompletely, the structure of glasses. The utility of this characterization derives from the fact that it is derivable, via Fourier transformation, from the results of diffraction experiment. It yields crucial information about the all-important short-range order and the nature of the chemical bonding. It also serves as a key test of different structural models. Researchers usually measure the structure factor of the material from either X-ray or neutron elastic scattering experiments. For an isotropic material, the static structure

factor S(Q) is related to $g(r)$ by

$$S(Q) = 1 + 4\pi\rho \int_0^\infty (g(r) - 1)\frac{sin(Qr)}{Qr} r^2 dr \tag{1.3}$$

where Q is the momentum transfer.

1.3.2 Structural correlation functions for binary systems

For binary systems (systems with two species α and β), the two-body structural correlations are often calculated through the partial pair correlation functions and partial static structure factors. Partial pair correlation functions are calculated from

$$\langle n_{\alpha\beta}(r)\rangle \Delta r = 4\pi r^2 \Delta r \rho c_\beta g_{\alpha\beta}(r), \tag{1.4}$$

where $n_{\alpha\beta}(r)\Delta r$ denotes the number of particles of species β in a shell between r and $r + \Delta r$ around a particle α. The angular brackets represent the ensemble average and an average over all the particles of species α. c_β=N_β/N ($N = N_\alpha$+N_β) is the concentration of species β. The total pair correlation will be the sum of all partial contribution

$$g(r) = \sum_{\alpha\beta} c_\alpha c_\beta g_{\alpha\beta}(r). \tag{1.5}$$

Partial structure factors are directly linked to partial pair correlation functions via Fourier transforms. One can write:

$$S_{\alpha\beta}(Q) = \delta_{\alpha\beta} + 4\pi\rho(c_\alpha c_\beta)^{1/2} \int_0^\infty (g_{\alpha\beta}(r) - 1)\frac{sinQr}{Qr} r^2 dr, \tag{1.6}$$

and the total structure factor is given by

$$S(Q) = \sum_{\alpha\beta} (c_\alpha c_\beta)^{1/2} S_{\alpha\beta}(Q). \tag{1.7}$$

$S_{\alpha\beta}(Q)$ defined in Eq. 1.6 is usually termed as Faber-Ziman structure factors[7]. Experimentalist usually uses Faber-Ziman structure factor to extract the pair correlation functions.

1.3.3 Neutron-scattering correlation functions

The neutron-scattering static structure factor can be obtained from the partial static structure factor by weighting them with coherent neutron-scattering lengths:

$$S_N(Q) = \frac{\sum_{\alpha\beta} b_\alpha b_\beta (c_\alpha c_\beta)^{1/2}[S_{\alpha\beta}(Q) - \delta_{\alpha\beta} + (c_\alpha c_\beta)^{1/2}]}{[\sum_\alpha b_\alpha c_\alpha]^2}, \tag{1.8}$$

where b_α denotes the coherent neutron-scattering length of species α. The other structural correlation function that is often used in the analysis of neutron-diffraction data is

$$g_N(r) = \frac{\sum_{\alpha\beta} c_\alpha b_\alpha c_\beta b_\beta g_{\alpha\beta}(r)}{[\sum_\alpha b_\alpha c_\alpha]^2}. \tag{1.9}$$

Throughout our work we used the following scattering lengths b_A (A=Ge, Se, Si, O) for germanium (Ge), selenium (Se), silicon (Si) and oxygen (O): b_{Ge}=8.185 fm, b_{Se}=7.970 fm, b_{Si}=4.149 fm and b_O=5.803 fm (1fm=10^{-15}m).

1.4 Vibrational Properties

In a crystal, vibrational modes can be classified in terms of the wavevector because of lattice periodicity. This gives rise to dispersion relations which describe the dependence of the vibrational frequency on the wavevector. Since amorphous solids have no real-space periodic lattice, consequently no reciprocal lattice either, this classification is not possible. Vibrations in this case are usually described in terms of the vibrational density of states (VDOS) g(ω), which is the number of vibrational states having frequencies between ω and ω+dω. For an amorphous solid, the VDOS is a sum of $3N$ (N is the number of atoms) delta functions corresponding to the allowed frequency modes, i.e.

$$g(\omega) = \sum_k \delta(\omega - \omega_k), \tag{1.10}$$

where k is simply a label for the modes and has no other physical significance. In simulation, the vibrational energies (vibrational modes) are obtained from the dynamical matrix, which is determined by displacing each atom by 0.03 Å in three orthogonal directions and then performing *ab initio* force calculations for all the atoms for each such displacement[8]. Each such calculation yields a column of the force constant

matrix. The vibrational eigenvectors and eigenvalues of the supercell are then easily obtained. The VDOS are determined from the eigenvalues by summing Gaussian centered at each eigenvalue.

1.5 Electronic Structure Analysis

A general expression for the total electronic density of states (EDOS), valid for all types of materials, is as a sum of delta functions

$$g(E) = \sum_{E_i} \delta(E - E_i), \tag{1.11}$$

where E_i is the energy associated to an eigenstate.

For disordered materials with different types of atoms in the basis, it is often informative to know the *local* density of states, i.e. that associated with a particular single atom. It provides insight into the origin of specific features in the total density of sates. The *local* density of states associated with a particular atom n, can be obtained by projecting the contributions to the total quantity onto the atom in question. Therefore, one can write

$$d_n(E) = \sum_{E_i} P_n^i \delta(E - E_i), \tag{1.12}$$

where P_n^i is the probability of finding an electron in an atomic state localized on atom n.

In order to connect localized eigenstates to particular topological/chemical irregularities, one often measure the inverse participation ratio (IPR), which we denote by $\mathcal{I}$. The IPR

$$\mathcal{I}(E) = \sum_{n=1}^{N} q(n, E)^2 \tag{1.13}$$

indicates the localization of electronic eigenvalues. Here N is the number of atoms in the model and $q(n, E)$ is the Mulliken charge localized on atomic site n in a certain eigenstate E. Hence, $\mathcal{I}$ is a measure of the inverse number of sites involved in the state with energy E. For a uniformly extended state, the Mulliken charge contribution per site is uniform and $\mathcal{I}(E)$=$1/N$. For an ideally localized state, only one atomic site

contributes all the charge and $\mathcal{I}(E)$=1. Therefore a larger value of $\mathcal{I}$ means that the eigenstate is more localized in real space.

In amorphous materials, the density of states is qualitatively different from that displayed by the corresponding crystals. Electronic states at the edges of bands of allowed states are spatially localized. This localization is different from the strongly localized nature of impurity or defect gap states.

1.6 Organization of Dissertation

The outline of the dissertation is as follows. In Chapter 2 we give a brief review of conventional modeling schemes and earlier calculations. We also compare two *ab initio* force codes FIREBALL and SIESTA. In Chapter 3, we carry out first-principles molecular dynamics simulations using the quench from the melt regime to study the structural, dynamical, and electronic properties of $GeSe_4$ and $GeSe_9$. Good agreement with experiment is obtained for the structural properties and for the electronic density of states. We also present models of Ge-Se glasses heavily doped with Ag obtained from *ab initio* simulation and study the dynamics of the network with an emphasis on the motion of Ag^+ ions. The models are analyzed with partial pair correlation functions, static structure factors and novel wavelet techniques. Ag diffusion is observed directly from thermal simulation. The most diffusive Ag^+ ions move preferentially through low density regions of the network and the existence of well-defined trapping centers is confirmed. New modeling schemes for binary IV-VI glasses are presented in Chapter 4. We show that for certain binary IV-VI (especially silica), decoration of bond-centered column VI atoms on tetrahedral amorphous networks leads with appropriate re-scaling and relaxation to highly realistic models of the IV-VI glass. In particular the problem of freezing in too much liquid-like character seems to be significantly ameliorated. We also propose a novel approach to model amorphous materials using a hybrid reverse Monte Carlo approach in conjunction with approximate first-principles molecular dynamics. We illustrate the method by studying the complex binary glassy material g-$GeSe_2$. Also, by developing the notion of inferring

complex "building blocks" we made a realistic model of $GeSe_{1.5}$ glass (g-$GeSe_{1.5}$). The concluding remarks are given in Chapter 5.

Chapter 2

Conventional Modeling Schemes and Earlier Calculations

2.1 Quench from the Melt Method

MD simulation mimics the experimental procedure of constructing of an amorphous structure from its liquid phase via quenching. It consists typically of disordering the crystalline phase at high temperature so that the system "forgets" its crystalline origin, equilibrating a liquid, then quenching it, and finally performing annealing cycles to bring the system to a local energy minimum state. We name this "quench from the melt" also informally as "cook and quench". The major limitation of the quench from the melt technique is the short time scale, since the time scale of quenching materials in the laboratory is dramatically longer than the time scale that we simulate on the computer. Because of this, the simulation cannot explore a similar volume of configuration space as that visited by experiment.

There have been successes for quench from the melt. Drabold *et al*[9] found that the method can work quite well for As-Se glasses with a suitably simplified *ab initio* density functional Hamiltonian. Moreover, the method has been successfully applied to silica and certain chalcogenide glasses. Studies conducted on a variety of Se alloy glasses have convinced us that it is relatively easy to construct realistic models (meaning in adequate agreement with experiment) for stoichiometric compositions (such as

As_2Se_3 or $GeSe_2$), but that it is more challenging to construct models at compositions far from stoichiometry. Almost certainly, the ease of constructing quality models at these special compositions is connected to the similarity of the topological (and chemical) order in the liquid, not far above the melting point, and the glass. This probably accounts for the failure of producing experimentally realistic models of amorphous silicon by quenching from the melt due to the fact that the liquid is $\sim$6-fold coordinated and a metal[10], whereas the amorphous phase is a tetrahedral insulator.

2.2 WWW Method

In 1985, Wooten, Winer and Weaire proposed a Monte Carlo scheme for the generation of tetrahedrally bonded, four-fold coordinated, amorphous structures[11]. This method (named the WWW method) was used to generate networks of amorphous silicon but has since been applied to other materials. In its original form, one starts from the diamond structure with periodic boundary conditions build in, then repeatedly rearrange the structure by an elementary process, bond switch, in which the tetrahedral bonding is preserved while five- and sevenfold rings (a characteristic structural feature of the CRN) are introduced.

Monte Carlo moves are accepted in Metropolis fashion with Keating springs (classical springs) as the interatomic potential. In practice, the method is not trivial to implement: one has to randomize the crystalline network sufficiently (create sufficient disorder) so that subsequent annealing will not lead the system back to the crystalline state, and perform a proper simulated annealing scheme to produce the optimal structure of the amorphous material in order to prevent the system getting stuck in an unphysical local minimum. Recently, Mousseau and Barkema[12] have introduced an improved version of WWW method. They have shown that starting with a completely random configuration leads ultimately to topologically identical networks as those obtained from the randomized crystal.

The WWW method and its variants are very successful in generating high quality amorphous networks. These models agree remarkably well with experiment on structure, electronic structure and dynamics. The success of the method arises from the

fact that the WWW moves are quite physical[13] on time scales beyond molecular dynamics (MD) simulations, and the constraint that the atoms should be four-fold forcing the bond angles close to the tetrahedral angle.

2.3 Reverse Monte Carlo Methods

A difficulty with most of the traditional methods is that they require some kind of interatomic model potential between the particles, which is difficult to construct for most materials, and are often not accurate enough to be able to accurately reproduce the experimental data. The Reverse Monte Carlo (RMC) approach overcomes these problems with its ability to model disordered materials without the need of any potentials.

In one's imagination, the general idea lying behind RMC approach[14, 15] is to form an atomistic model that agrees with all acceptable experiments by filling a large box with atoms, and moving them in some way until the coordinates reproduce all the known experiments. At its simplest, it is a technique for generating structural configurations based on experimental data. The method was originally developed by McGreevy & Pusztai[16] for liquid and glassy materials for lack of different routes to explore experimental data but in recent years progress has been made toward modeling crystalline systems as well[17].

Biswas *et al*[18] have significantly improved the original RMC. Starting with a suitable configuration, atoms are displaced randomly using the periodic boundary condition until the input experimental data (either the structure factor or the radial distribution function) match with the data obtained from the generated configuration. This is achieved by minimizing a cost function which consists of either structure factor or radial distribution function along with some appropriately chosen constraints to restrict the search space. Consider a system having N atoms. One can construct a generalized cost function for an arbitrary configuration by writing :

$$\xi = \sum_{j=1}^{K} \sum_{i=1}^{M_K} \eta_i^j \{F_E^j(Q_i) - F_c^j(Q_i)\}^2 + \sum_{l=1}^{L} \lambda_l P_l \tag{2.1}$$

where η_i^j is related to the uncertainty associated with the experimental data points as well as the relative weight factor for each set of different experimental data. Here K and M_K respectively stand for the total number of different experimental data sets employed and data points for the Kth set. L is the number of additional (non-experimental) constraints included. The quantity Q is the appropriate generalized variable associated with experimental data $F(Q)$ and $P_l > 0$ is the penalty function associated with each constraint and λ_l is a (positive) weight factor for each constraint. Such "additional" constraints can be of many different forms (for example, one may impose chemical or topological ordering, or phase separated units within a continuous random network). The coordinates of atoms are changed according to Monte Carlo moves, which is akin to a simulated annealing minimization of our cost function ξ. In order to avoid the atoms from coming too close to each other, a certain cut-off distance is also imposed which is typically of the order of interatomic spacing and is usually obtained from the radial distribution function.

Although RMC has been applied to many different systems - liquids, glasses, polymer and magnetic materials, it suffers from two major problems that raise questions about the reliability of the results. Firstly, RMC does not produce a unique structure, but rather a plausible structure (this problem is acute when only radial distribution or structure factor is used to obtain structure with no or a few constraints). Secondly, there is no guarantee that the generated structure corresponds to a local minimum on the multidimensional true energy landscape. Consequently, RMC tends to produce the most disordered structure that is consistent with the experimental data (and the constraints).

The method is easy to implement, though care must be taken to include the minimum number of independent constraints possible to reduce the likelihood of getting "stuck" in spurious minima.

2.4 Interatomic Interactions

2.4.1 Empirical potentials

Much effort has been invested in deriving simple analytic potential models for covalent materials such as silicon, applicable amorphous materials. In order to investigate theoretically these systems, it is necessary to model the interactions as accurately as possible, and ensure that the calculations remain computationally feasible. The simplest approaches rely upon the use of empirical potentials. The intuitive picture of an empirical potential is to "guess" a functional form with free parameters and to then determine the parameters by fitting to various experimentally obtained properties, such as lattice constant and bulk modulus. If the energy functional was chosen with enough of the "underlying physics", then the functional may provide a reasonably transferable description of the energetics and interatomic forces.

At a practical level, the success of the empirical approaches relies on their simplicity and their computational efficiency. If such potentials are used carefully, they can answer questions about model systems that are extremely large. An *ab initio* computation of atomic motion is prohibitively expensive to calculate for more than a few hundred atoms, even on the fastest computer. With simpler, empirical interatomic potentials, the same computers can perform simulations of millions of particles, making possible atomistic studies of incredibly complicated processes like melting, diffusion, amorphization, surface growth, plastic and cracking deformation in single crystal.

Although simulations with empirical potentials are fast, their uses are limited by the accuracy of the parametrisation, and correspondingly, their transferability to other environments can be poor (they do not reliably provide correct description for properties that are not explicitly included in the fitting database). Electronic structure information cannot be obtained, nor can we expect these potentials to accurately describe phenomena where quantum mechanical interference effects are essential.

Modelling interactions with no *a priori* knowledge of the bonding present requires the use of sophisticated *ab initio* methodologies, in which one attempts to solve

the Schrödinger equation which *ultimately* determines the atomic dynamics. Most commonly, one employs the density functional theory (DFT) due to Kohn, Hohenberg and Sham[19].

2.4.2 Density functional methods

In density functional theory (DFT), the ground state properties of a quantum many body system can be expressed in terms of single particle electron density, rather than many body wave functions. This concept leads to a remarkable reduction in difficulty. The foundation of zero-temperature DFT is governed by two fundamental statements. In the first statement, the ground state energy of a many electron system is a functional of the electron density $n(\vec{r})$:

$$E[n] = \int V_{ext}(\vec{r})n(\vec{r})d^3r + F[n], \tag{2.2}$$

where V_{ext} is an external potential which contains the contribution of electron-ion interactions and ion-ion interactions (but not electron-electron interactions), and $F[n]$ is a *universal* functional of the density, independent of the external potential concerned. The exact density dependence of this functional is, however, unknown.

Concerning the second statement, the functional $E[n]$ is minimized by the true ground state density. Variation of the total energy functional $E[n]$ with respect to the electron density, subject to the constraint of fixed particle number, yields to the decomposition of the functional $F[n]$ in the form:

$$F[n] = T[n] + E_H[n] + E_{xc}[n]. \tag{2.3}$$

Here, the term $E_H[n]$ is the electrostatic (Hartree) interaction of the electrons and may be written as

$$E_H[n] = \frac{e^2}{2}\int\int \frac{n(\vec{r})n(\vec{r'})}{|\vec{r}-\vec{r'}|}d^3rd^3r'. \tag{2.4}$$

The two other terms, T and E_{xc} are respectively the kinetic energy of a *noninteracting* electron gas of density n and the *exchange-correlation* energy (unknown functional which includes nonclassical effects of the interacting electrons).

To evaluate the kinetic term, Kohn and Sham provided a paradigm by introducing single-particle orbitals "Kohn-Sham orbitals", $\langle\chi_i|$, into the problem, such that the charge density of the physically relevant interacting system is given by:

$$n(\vec{r}) = 2\sum_{iocc} |\langle\vec{r}|\chi_i\rangle|^2 \tag{2.5}$$

Thus the independent-particle kinetic energy T can be written as

$$T = \sum_{iocc}\langle\chi_i| - \frac{\hbar^2}{2m}\nabla^2|\chi_i\rangle. \tag{2.6}$$

One must now solve the following self-consistent Kohn-Sham equations (using the constraint that $\langle\chi_i|\chi_j\rangle = \delta_{ij}$)

$$\{-\frac{\hbar^2}{2m}\nabla^2 + V_{eff}[n(\vec{r})]\}|\chi_i\rangle = \varepsilon_i|\chi_i\rangle \tag{2.7}$$

where V_{eff} is an effective local potential

$$V_{eff}(\vec{r}) = V_{ext}(\vec{r}) + e^2\int\frac{n(\vec{r'})}{|\vec{r}-\vec{r'}|}d^3r' + \frac{\delta E_{xc}[n(\vec{r})]}{\delta n(\vec{r})}. \tag{2.8}$$

The equations have the form of independent-particle equations with a potential that must be found self-consistently with the resulting density. These equations are independent of any approximation to the functional $E_{xc}[n]$, and would lead to the exact ground state density and energy for the interacting system, if the exact functional $E_{xc}[n]$ were known. To make practical use of these equations one requires sufficiently accurate and simple approximations to $E_{xc}[n]$. Fortunately these exist. The simplest is the local density approximation (LDA) which take the electron density to be *locally* uniform. In LDA, E_{xc} is defined as

$$E_{xc}^{LDA}[n] = \int\epsilon_{xc}[n(\vec{r})]n(\vec{r})d^3r \tag{2.9}$$

where $\epsilon_{xc}[n]$ is the exchange-correlation energy per particle of a uniform electron gas of density n. Despite its apparent simplicity it has been found to be very useful.

Plane-wave LDA

In order to accurately describe the electron wavefunctions of the system being studied, it is necessary to choose a suitable set of simple basis functions in terms of

which one can write a series expansion of the electronic wavefunctions. One approach is to employ a basis set more suitable for a momentum space description of the material, namely plane waves. In the plane waves basis, the eigenstates of the Kohn-Sham equations in LDA satisfy the eigenvalue equation

$$\mathcal{H}|\chi_i\rangle = \{-\frac{\hbar^2}{2m}\nabla^2 + V_{eff}(\vec{r})\}|\chi_i\rangle = \varepsilon_i|\chi_i\rangle \tag{2.10}$$

where the eigenfunction $|\chi_i\rangle$ can be expanded in the complete set of Fourier components (states obeying periodic boundary conditions)

$$|\chi_i\rangle = \sum_{\vec{G}} C_{i,\vec{G}} \frac{1}{\sqrt{\Omega}} exp(i\vec{G}.\vec{r}) \equiv \sum_{\vec{G}} C_{i,\vec{G}}|\vec{G}\rangle. \tag{2.11}$$

Ω is the cell volume and $\vec{G}$ labels reciprocal lattice vectors. Since plane waves with small kinetic energy are typically more important than those with large kinetic energy, the sum can be truncated to include only plane waves that have kinetic energies less than some particular cutoff energy (wavelength small enough). In this representation the kinetic energy is diagonal and the matrix elements of V_{eff} are obtained by fast Fourier transforms, which makes the plane-wave approach tractable.

The first *ab initio* molecular dynamics simulation using plane-waves was performed in mid eighties by Car and Parinello. They combined a plane wave basis and an iterative minimization scheme to solve the self-consistent LDA equations and simultaneously evolve the atomic coordinates.

Local basis

A local orbital representation involves a set of orbitals, usually centered on atoms. Here the eigenvectors are expressed in terms of the local orbitals, which is helpful in interpreting the physical meaning of the results. The matrix elements including the hamiltonian matrix and the overlap matrix can be divided into one-, two-, and three-center terms. To improve the efficiency of the approach, the two and three-center matrix elements can be tabled, avoiding computing integrals during an MD simulation or electronic structure calculation; rather making many calls to one and two dimensional interpolators[20].

Local orbitals can be used as a basis to carry out a full self-consistent solution of independent-particle equations and have the ability to perform exact diagonalization which is valuable for systems with states in the gap and particularly metallic systems. In this real-space approach, no artificial periodicity is ever imposed, making the approach more suitable to describe isolated clusters of atoms, to investigate properties of large molecules or of isolated defects in bulk materials, where plane waves become expensive to use.

Comparison between FIREBALL and SIESTA

For some of the simulations reported in this work, we used FIREBALL[21] and SIESTA[22], two force and energy codes that produce different results for the same system. Our wish is to understand why this happens. Let us first give a brief description of the codes and then give an example.

The first code, FIREBALL, is a density functional code in the LDA developed by Sankey and coworkers. This is an approximate *ab initio* local density approach to electronic structure, force and dynamical simulation that derived from density functional theory using the Harris [23] functional and a minimal basis set. Because the code employs the Harris functional, no self-consistent field iterations are required, which is of great benefit to the code's efficiency. This is a relevant point for glassy materials which require the use of large supercell models [24]. The basis set is minimal (for these systems, one s and three p slightly excited pseudoatomic orbitals per site or "single zeta" in the language of quantum chemistry). In its original form [21] only weakly ionic systems may be treated; self-consistent versions have been developed recently by Lewis and coworkers[25]. This improved version, FIREBALL2000, uses separable pseudopotentials, and allows for double-zeta (DZ) numerical basis sets and polarization orbitals. The calculation is undertaken entirely in real space (unlike the code SIESTA), which provides substantial computational efficiency. Hamiltonian and overlap matrix elements are precalculated on a numerical grid and the specific values needed for a particular instantaneous conformation are extracted from the tabulated values via interpolation. Naturally, the integral tables need to be generated only once, for a given set of atomic species, rather than performing quadratures "on the fly"

during a MD run. These approximations perform exceptionally well for chalcogenide systems.

The other code, SIESTA, has broad flexibility with respect to basis set, density functional, and simulation regime. It uses the standard Kohn-Sham selfconsistent density functional method in the local density approximation (LDA), local spin density (LSD) or generalized gradient (GGA) approximations and uses norm-conserving pseudopotentials in its fully nonlocal (Kleinman-Bylander) form. The basis set allows arbitrary angular momenta, multiple-zeta, polarized and off-site orbitals. The electron wavefunctions and density are projected onto a real-space grid in order to calculate the Hartree and exchange-correlation potentials and their matrix elements. Besides the standard exact diagonalization method, it allows the use of localized linear combinations of the occupied orbitals (valence-bond or Wannier-like functions), making the computer time and memory scale linearly with the number of atoms.

To model GeSe glasses with SIESTA, the first step is to construct a reliable pseudopotential. A pseudopotential is constructed to replace the atomic all-electron potential such that core states are eliminated and the valence electrons are described by nodeless pseudo wavefunctions. In doing so the principal objectives to consider are (i) the transferability of the pseudopotential (its ability to accurately describe the valence electrons in different atomic, molecular, and solid state environments). In self-consistent total energy calculations this means that the valence states have the proper energies and lead to a properly normalized electron distribution which in turn yields proper electrostatic and exchange-correlation potentials, particularly outside the core region, i.e. where the chemical bonds form. (ii) Their efficiency, that is to keep the computational workload in applications as low as possible, allowing computing wavefunctions and electron densities with as few basis functions and operations as possible. We constructed several pseudopotentials for the chalcogens Se: GGA with and without core corrections, and LDA with and without core corrections.

Having reliable pseudopotentials we used the state of the art first principles MD code, SIESTA to relax models of g-$GeSe_2$ obtained with FIREBALL. An appropriate cutoff energy was used especially for core corrections to properly handle the hard pseudopotential. We include double-zeta and polarized orbitals to quench the 216-atom

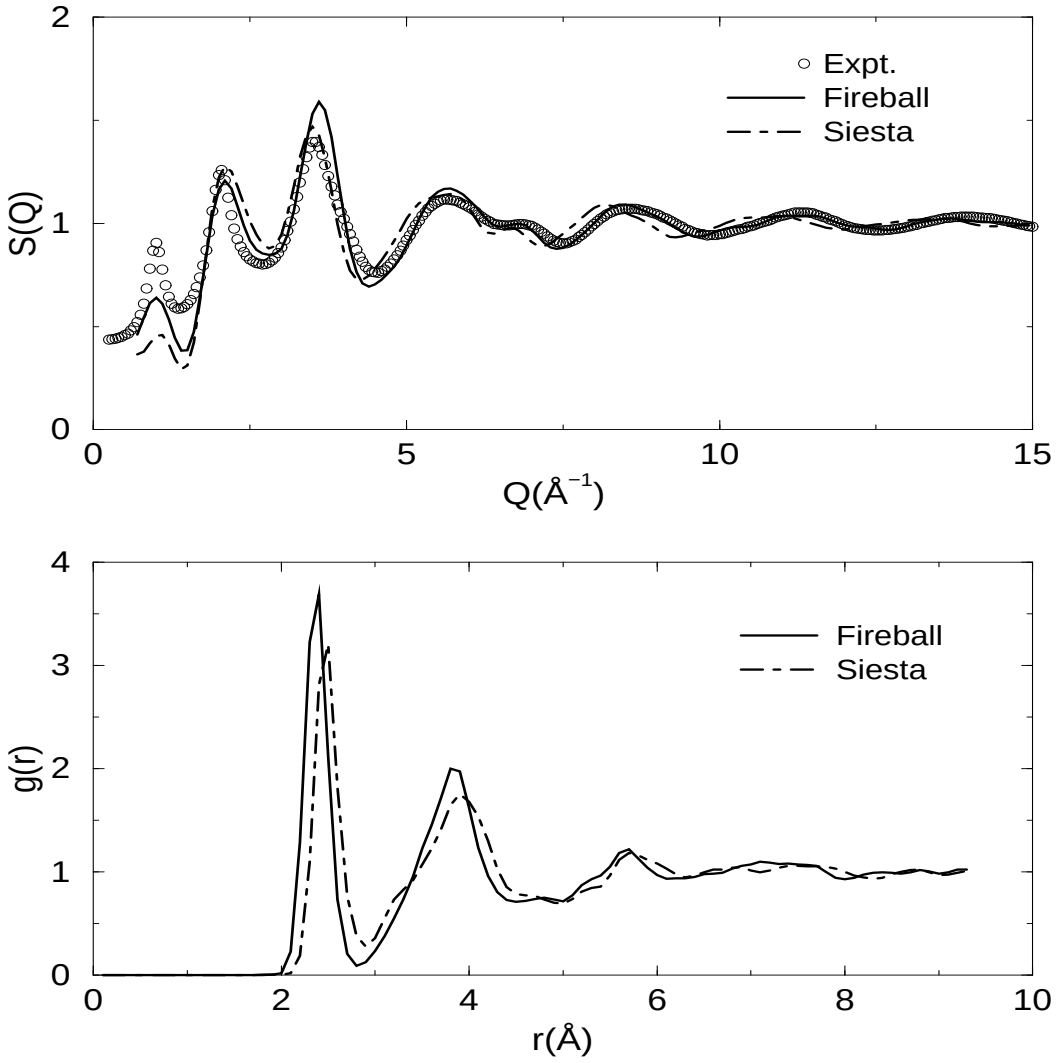

Figure 2.1: Static structure factor S(Q) and pair correlation function g(r) of 216-atom g-$GeSe_2$ from SIESTA, 216-atom g-$GeSe_2$ from FIREBALL and experiment[26]

Table 2.1: Position of the peaks in g(r) and S(Q) compared to experiments[26] . Q_1 and Q_2 are the positions of the FSDP and the second peak respectively in S(Q). r_1 and r_2 are the positions of the first and second peak respectively in g(r).

	S(Q)		g(r)	
	$Q_1(Å^{-1})$	$Q_2(Å^{-1})$	$r_1(Å)$	$r_2(Å)$
Experiment	0.99	2.02	2.35	3.87
Fireball	1.00	2.05	2.35	3.87
LDA + Harris + SZ	1.04	2.10	2.47	3.91
LDA + Harris + DZP	1.04	2.10	2.46	3.91
GGA + SC + SZP	0.88	2.29	2.60	3.93

model of g-$GeSe_2$. We did not observe any improvement to the structural properties of the model by this expensive calculation; we rather obtained a poor model compared to the FIREBALL models. The peaks' positions in the pair correlation function g(r) and static structure factor S(Q) have been shifted toward large r and large Q respectively. The intensity of the FSDP peak is poorly reproduced, very low compared to the experiment and the FIREBALL models (see Fig. 2.1). Table 2.1 indicates that SIESTA does very poorly in producing models of chalcogenide, especially in the GGA. In addition SIESTA always produces more disorder than FIREBALL. The statistics of the number of atoms of each type of coordination for the FIREBALL's model and SIESTA's models (LDA + Harris + SZ, LDA + Harris + DZP, GGA + SC + SZP) are listed in Table 2.2.

We found this expensive calculation with more accurate Hamiltonian achieves lesser than its counterpart FIREBALL. The CPU time spent on these calculations is more than 5 times longer than the time used in FIREBALL. The difference in the results might be linked to the difference in the basis sets, the pseudopotentials and Harris functional. However, it is still a puzzle to understand why one works and the other does not. Both codes are extremely valuable tools with subtle differences in their approximations which are somehow manifested in these systems.

Table 2.2: Coordination number (C.N.) distribution in 216-atom model of g-$GeSe_2$. Comparison between FIREBALL's model and SIESTA's models. The number in parentheses denotes the percentage of the atoms in this configuration.

		Number of atoms			
Atoms	C.N.	Fireball	LDA+Harris+SZ	LDA+Harris+DZP	GGA+SC+SZP
Se	1	15 (7.0%)	19 (8.8%)	19 (8.8%)	3 (1.4%)
	2	101 (46.7%)	92 (42.6%)	93 (43.1%)	85 (39.3%)
	3	28 (13.0%)	33 (15.2%)	32 (14.8%)	56 (25.9%)
Ge	2	-	1 (0.5%)	3 (1.4%)	9 (4.2%)
	3	13 (6.0%)	11 (5.1%)	11 (5.1%)	16 (7.4%)
	4	59 (27.3%)	60 (27.8%)	58 (26.8%)	38 (17.6%)
	5	-	-	-	9 (4.2%)

Chapter 3

Quench from the Melt Method

3.1 Binary Chalcogenide Glasses: Ge_xSe_{1-x}

In this section we discuss model calculations on Ge_xSe_{1-x} (x=0.1, 0.2) using the quench from the melt technique described below. To our knowledge there is little experimental and theoretical work on the structure and vibrational structure of g-$GeSe_4$ (x=0.2), and nothing on electronic structure. Compositions near g-$GeSe_4$ are used as a host for Ag^+ ions and the Programmable Metallization Cell[27]. In a joint experimental and theoretical study of g-$GeSe_9$ (x=0.1), Rao *et al* [28] limited their work only to the static structure factor and the pair distribution function. They have suggested that g-$GeSe_9$ consists predominantly of Se-chain segments interlinked with tetrahedra. Theirs is the first attempt to carry out theoretical work on the vibrational and electronic structure of $GeSe_9$ glass. We demonstrate the utility of our simulations by performing detailed comparison with diffraction data (where available) in real and k-space and by comparing to vibrational and electronic measurements where available.

3.1.1 Model formation

A 600-atom model of g-$GeSe_4$ was made using the quench from the melt technique. We randomly placed atoms in a cubic supercell with edge length 26.061 Å selected to produce the experimental number density[29] (ρ=0.0339 $Å^{-3}$). The initial temperature of our system was 2400 K. We equilibrated the cell at 1400 K for approximately

4 ps. After equilibration, we began quenching it down to about 700 K over 4 ps. As the final step, we steepest descent quenched the cell to 0 K with FIREBALL[21] and minimized the energy until all forces were smaller than 0.02 eV/Å in magnitude.

To model g-$GeSe_9$ we randomly placed atoms in a cubic supercell, (consisting of 40 Ge atoms and 360 Se atoms), with side length of 22.971 Å. This gives a total number density close to experiment (0.0330 $Å^{-3}$) [28]. Then we brought the temperature of the system to 2200 K. We took three steps to cool down the model. First, the cell was equilibrated at 1400 K for over 2 ps; then we cooled it at 300 K for over 3 ps. Finally the cell was steepest descent quenched to 0 K with FIREBALL[21].

All the calculations were performed at constant volume using the Γ ($\vec{k} = \vec{0}$) point to sample the Brillouin zone in order to compute energies and forces. Considering the large supercell volume it was reasonable to use Γ point alone.

3.1.2 Structural properties

Structural information can be extracted from the neutron static structure factor S(Q). S(Q) has been obtained by weighting the calculated partial structure factors with the neutron scattering lengths of the corresponding elements. The topology of our models is also analyzed with ring statistics. The ring structures in our models are determined by starting on a particular atom, moving to one of its neighbors, and then repeating this process for the neighbor until the original atom is located again after the desired number of iterations (making sure not to include any atom which is already part of the ring from a previous iteration since an n-fold ring consists of $2n$ alternating IV-VI bonds).

$GeSe_4$ glass

In Fig. 3.1 we compare the neutron static structure factor S(Q) to the experiment of Petri and Salmon [26]. The first sharp diffraction peak (FSDP) is present in the quench from the melt model at 1.12 $Å^{-1}$. The second peak depends on the next nearest neighbors at approximately 3.8 Å. From the partial structure factors, it is evident that the second peak is due to Se-Se correlations. There is still a slight

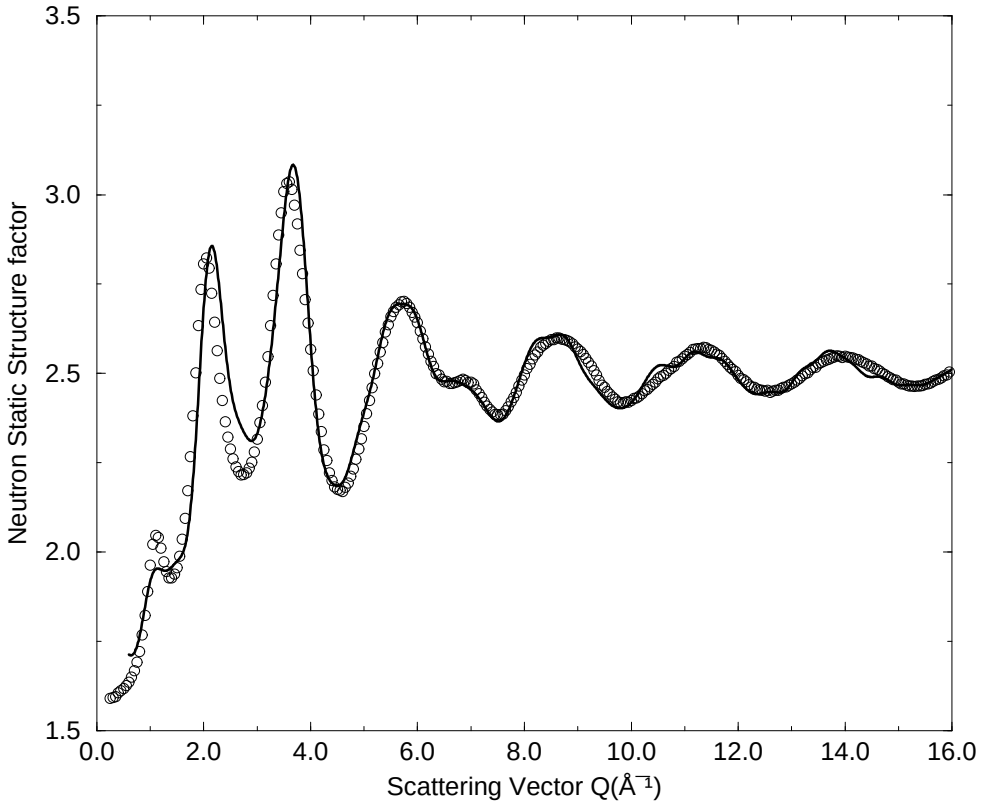

Figure 3.1: Calculated total neutron structure factor S(Q) of quench from the melt glassy $GeSe_4$ (solid line) compared to experimental [26] data (circles).

discrepancy between the experimentally observed strength of the second peak and that of our S(Q). Overall our calculated neutron structure factor is in agreement with the experimental results.

In our model the FSDP is clearly seen in $S_{CC}(Q)$ at around 1.08 $Å^{-1}$ which implies that the strong Ge-Ge intermediate-range order (IRO) correlations in g-$GeSe_4$ are reasonably well described. This feature does not, however, appear in classical molecular dynamics (MD) simulations [30] of amorphous $GeSe_2$ and it has proved possible to reproduce this feature using the first principles MD approach of Massobrio et *al* [31] only when a generalized gradient approximation (GGA) is used in the density functional.

Where coordination is concerned, we note that 88.5 % of Ge are fourfold coordinated and are mostly in $GeSe_4$ tetrahedral units, 8 % are threefold coordinated and 3.5 % are twofold and fivefold coordinated. Se is quite a different story: about 64 % of the Se are twofold coordinated, 19 % are threefold and about 17 % are onefold coordinated. Where chemical order is concerned, g-$GeSe_4$ has 64.23 % Ge-Se bonds, 0.9 % Ge-Ge bonds, and 34.87 % Se-Se bonds. In Table 3.1 we give a full description of the topology of our model. In Fig. 3.2 we plot the partial pair correlation function of g-$GeSe_4$. The peaks in $g_{\alpha\beta}(r)$ for distances larger than the nearest neighbor distance are a manifestation of the IRO in the system and $g_{Ge-Ge}(r)$ shows correlations between tetrahedra. There are two distinct peaks which correspond respectively to Ge-Ge first and second neighbors at 2.36 and 3.8 Å in $g_{Ge-Ge}(r)$. The broad peak between 3.0 and 4.3 Å in the $g_{Ge-Ge}(r)$ is caused by the presence of both corner sharing (CS) (the tetrahedra shares one Se atom) and edge sharing (ES) tetrahedra (the tetrahedra shares two Se atoms). In $g_{Ge-Se}(r)$ the first peak is located at 2.36 Å which is quite close to the crystal Ge-Se bond length of 2.355 Å (for α-$GeSe_2$). The next peak appears at 3.7 Å and it is associated with CS units. Another peak arises at 5.65 Å which indicates that there is some kind of IRO in our model; the strength and width of this peak suggest that its origin involves Ge correlations with Se on neighboring tetrahedra. The $g_{Se-Se}(r)$ nearest-neighbor peak is located at approximately 2.32 Å. The second peak at approximately 3.78 Å is close to the Se-Se separation distance in crystalline α-$GeSe_2$ [32]. Since the ratio of Ge-Se:Se-Se distances is 0.624,

close to the value of 0.612 expected for perfect tetrahedral coordination, the results indicate that there is a large number of tetrahedral $Ge(Se_{1/2})_4$ structural motifs.

We also obtain partial n_{Ge}, n_{Se}, and average n coordination numbers from the first neighbor coordination numbers n_{GeGe}, n_{GeSe}, n_{SeGe}, and n_{SeSe} (see Table 3.2) by integrating the partial pair correlation function $g_{\alpha\beta}(r)$. The theoretical Ge-Ge coordination number n_{GeGe} shows that each Ge atom has on average n_{GeGe}=0.12 nearest neighbors of the same species within a given shell of radius 2.8 Å. The predominant Ge-Se heteropolar bonding is expressed by a coordination number n_{GeSe}=3.80. The total Ge and Se coordination numbers, $n_{Ge}=n_{GeGe}+n_{GeSe}$, $n_{Se}=n_{SeSe}+n_{SeGe}$, are therefore 3.92 and 2.03 respectively. The average coordination number, $n=c_{Ge}n_{Ge}+c_{Se}n_{Se}$, gives a value n=2.41. The resulting values nearly satisfy the "8-N" rule. We know that there is not perfect chemical order - there are many Se-Se homopolar bonds. As this happens even in stoichiometric glasses, it is probably not due only to extra Se.

The topology of covalent glasses is commonly discussed in terms of rings. We have calculated the distribution of threefold to nine-fold rings. The distribution of rings for the model are given in Table 3.3. There is a predominance of fivefold and six-fold rings in the glass.

$GeSe_9$ glass

In Fig. 3.3 we compare the calculated neutron static structure factor S(Q) for g-$GeSe_9$ to the experimental results from neutron diffraction measurements [28]. The general trend complies with observation though the detailed structure departs from the experimental data. The FSDP appears only as a shoulder; and it is more pronounced in our calculation than in experiment (though it is quite weak in both). Experimental studies [26, 28] on Ge_xSe_{1-x} have shown that the intensity of FSDP first increases systematically with Ge concentration, then reaches its maximum at x=0.33, then subsequently decreases. The third peak and the features at higher Q depend mainly on the local environment. As soon as the nearest neighbor atoms are taken into account, the third peak appears. On the other hand, the second peak in S(Q) depends on the next-nearest neighbors at approximately 4.3 Å. The shoulder in S(Q) at around 1.04 $Å^{-1}$ is due to the cancellation between S_{GeGe}(Q) and S_{SeSe}(Q).

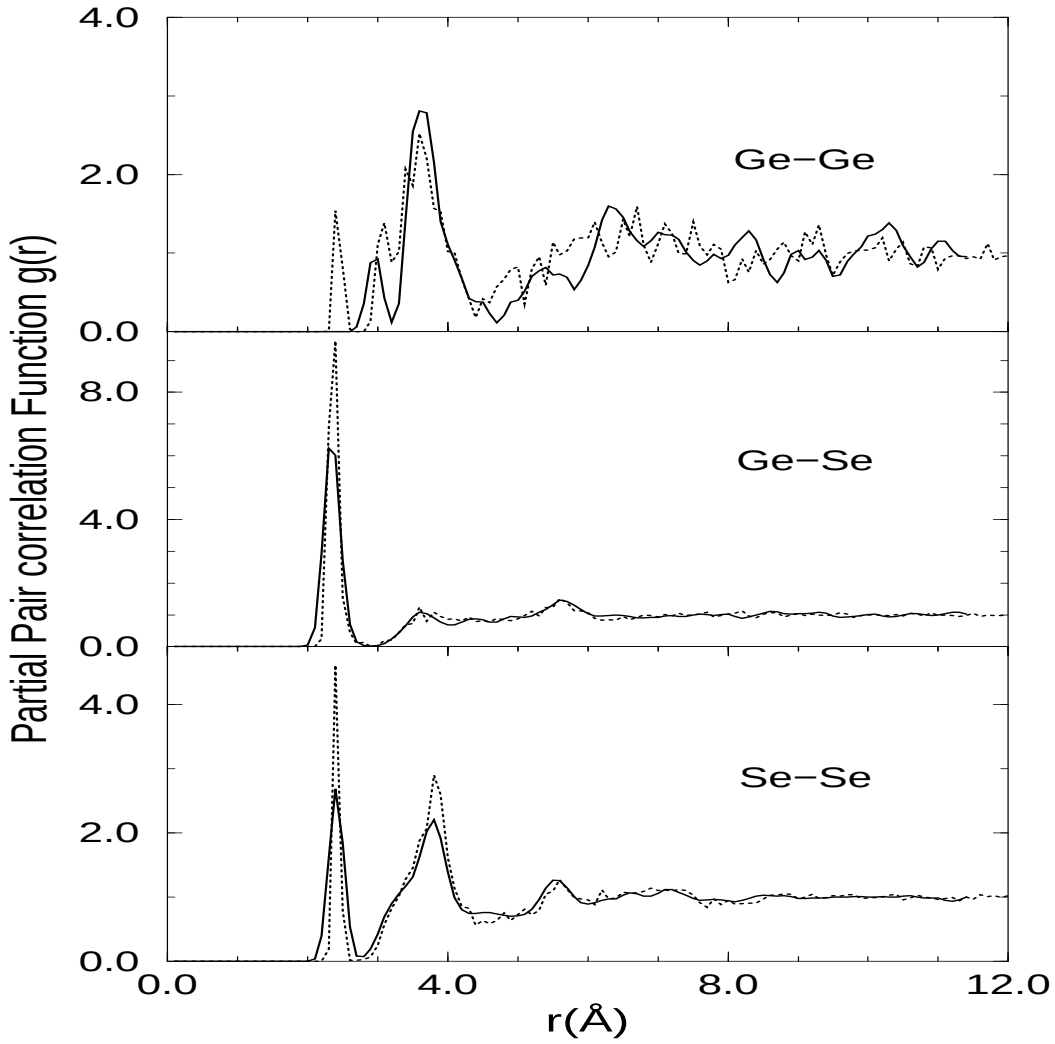

Figure 3.2: Partial pair distribution functions $g_{\alpha\beta}(r)$ vs r in g-$GeSe_4$ (dotted lines) and in g-$GeSe_9$ (solid lines).

Table 3.1: Average number $m_\alpha(l)$ (boldface characters, expressed as a percentage) of atoms of species α (α=Ge, Se) l-fold coordinated at a distance of 2.8 Å for $GeSe_4$. We also give the identity and the number of the Ge and Se neighbors for each value of $m_\alpha(l)$.

Ge	l=2	**2.5**	l=3	**8.33**	l=4	**88.34**	l=5	**0.83**
	Se_2	2.5	Se_3	8.33	$GeSe_3$	11.67	Se_5	0.83
					Se_4	76.67		
Se	l=1	**17.30**	l=2	**63.54**	l=3	**19.16**		
	Se	3.75	Se_2	19.79	Se_3	8.54		
	Ge	13.55	SeGe	25	Se_2Ge	3.54		
			Ge_2	18.75	$SeGe_2$	2.5		
					Ge_3	4.58		

Table 3.2: First and second peak positions in g-$GeSe_4$. Also first and second neighbor coordination numbers $n_{\alpha\beta}$ and $n'_{\alpha\beta}$. The integration ranges are 0-2.8 Å, 2.8-4.5 Å for Ge-Ge and Se-Se; 0-3.0 Å, 3.0-4.5 Å for Ge-Se and Se-Ge.

	First Shell		Second Shell	
Bond Type	r(Å)	$n_{\alpha\beta}$	r'(Å)	$n'_{\alpha\beta}$
Ge-Ge	2.36	0.12	3.8	2.26
Ge-Se	2.36	3.80	3.7	-
Se-Ge	2.36	0.91	3.7	-
Se-Se	2.32	1.12	3.78	9.74

Table 3.3: Ring statistics. The number of n-membered rings, n=3 through n=9.

Ring size	3	4	5	6	7	8	9
$GeSe_4$	5	20	39	30	9	13	8
$GeSe_9$	2	3	15	6	2	4	2

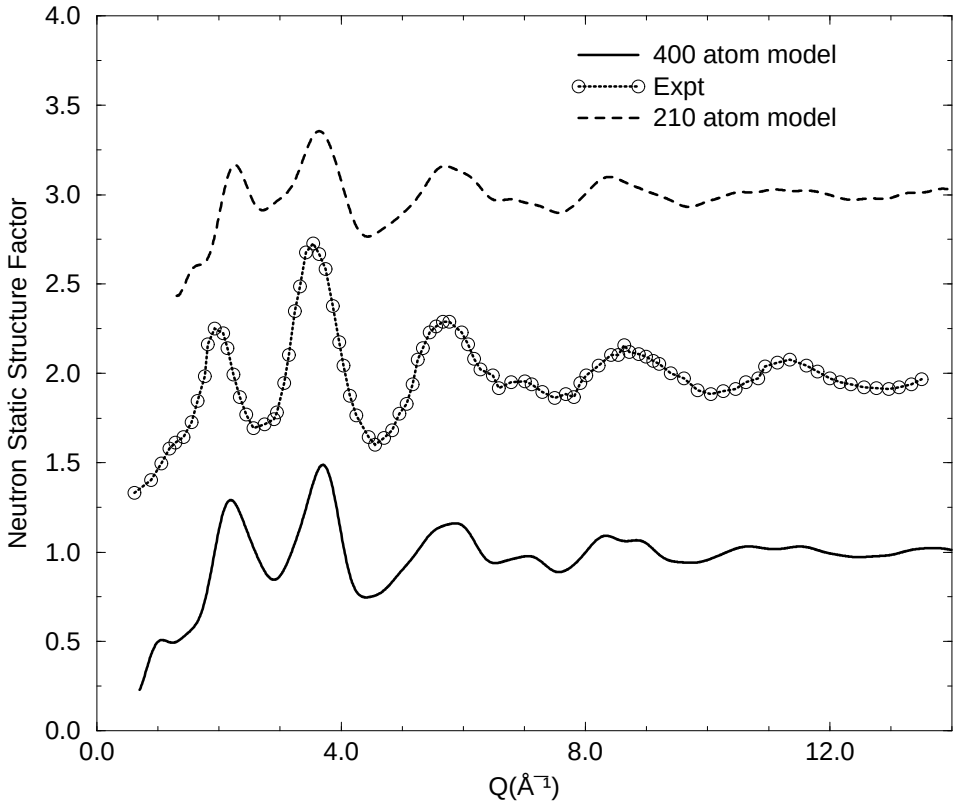

Figure 3.3: Calculated total neutron structure factor S(Q) of $GeSe_9$ (solid line) compared to experimental [28] data (circle).

Table 3.4: Average number $m_\alpha(l)$ (boldface characters, expressed as a percentage) of atoms of species α (α=Ge, Se) l-fold coordinated at a distance of 2.8 Å for $GeSe_9$. We also give the identity and the number of the Ge and Se neighbors for each value of $m_\alpha(l)$.

Ge	l=3	**2.5**	l=4	**92.5**	l=5	**5**
	Se_3	2.5	Se_4	92.5	Se_5	5
Se	l=1	**19.6**	l=2	**60**	l=3	**20.4**
	Se	7.1	Se_2	36.94	Se_3	16.78
	Ge	12.5	SeGe	16.94	Se_2Ge	3.06
			Ge_2	6.12	$SeGe_2$	0.28
					Ge_3	0.28

Partial pair correlation functions $g_{\alpha\beta}(r)$ are shown in Fig. 3.2. The Ge-Se pairs provide the dominant contribution to the first shell of the pair correlation function $g(r)$ whereas Ge-Ge does not have any effect. It is obvious that there exist Se-Se homopolar bonds in the model due to the surplus of Se atoms relative to the stoichiometric composition $GeSe_2$. Se-Se pairs make a strong contribution in the range of the second shell, whereas Ge-Ge pairs contribute most in the range of the third shell. In $g_{Ge-Ge}(r)$ there are two distinct peaks which correspond respectively to Ge-Ge second and third neighbors at 3.02 and 3.76 Å. In a-Ge the nearest neighbor Ge-Ge separation is known to be 2.463 Å [33]. The absence of a peak in the first shell of $g_{Ge-Ge}(r)$ is due to the absence of Ge-Ge homopolar bonds in our model. In $g_{Ge-Se}(r)$ the first peak is located at 2.36 Å, and the next peak appears at around 3.64 Å. The peak around 5.6 Å indicates that our model exhibits IRO.

About 92.5 % of Ge atoms are fourfold coordinated, 5 % are fivefold coordinated and 2.5 % are threefold coordinated. Also, only 60 % of Se atoms are twofold coordinated, 20.4 % are threefold and about 19.6 % are one-fold coordinated. Where chemical ordered is concerned, g-$GeSe_9$ has 36.3 % Ge-Se bonds and 63.7 % of Se-Se bonds. The Ge-Ge homopolar bonds are nonexistent in our model. The detailed

Table 3.5: First and second peak positions in g-$GeSe_9$. Also first and second neighbor coordination numbers $n_{\alpha\beta}$ and $n'_{\alpha\beta}$. The integration ranges are 0-2.8 Å, 2.8-3.23 Å for Ge-Ge; 0-2.8 Å, 2.8-4.1 Å for Ge-Se and Se-Ge; 0-2.8 Å, 2.8-4.34 Å for Se-Se.

	First Shell		Second Shell	
Bond Type	r(Å)	$n_{\alpha\beta}$	r'(Å)	$n'_{\alpha\beta}$
Ge-Ge	-	0.0	3.02	0.11
Ge-Se	2.37	3.99	3.64	3.66
Se-Ge	2.37	0.44	3.64	0.58
Se-Se	2.35	1.56	3.79	9.2

topology of our model is given in Table 3.4. Our results are in accordance with the chemically ordered continuous random network [34] which predicts that for $x < 0.33$, Se-Se bonds are present in addition to Ge-Se bonds. Similarly Ge rich glasses i.e. $x > 0.33$ contain Ge-Ge as well as Ge-Se bonds. The theoretical Ge-Ge coordination number, n_{GeGe}=0.0, confirms that each Ge atom does not have any nearest neighbors of the same species within a first shell of radius 2.8 Å. We also obtain partial n_{Ge}, n_{Se}, and average n coordination numbers (see Table 3.5 for details). The Ge and Se coordination numbers are respectively 3.99 and 2; that gives an average coordination number equal to 2.2. This number is quite reasonable since it lies between 2.16 for $x = 0.08$ and 2.24 for $x = 0.12$.

There is a significant amount of $Ge(Se_{1/2})_4$ tetrahedral units in our model. The structure of the glass consists of Se-chain segments which are cross-linked by $Ge(Se_{1/2})_4$ tetrahedra, as confirmed by n_{SeSe} and by visual inspection using XMOL [35]. We also note the presence of a few CS and a negligible fraction of ES. The structure of our model is also dominated by the presence of 5- and 6-member rings (see Table 3.3).

3.1.3 Dynamical properties

The vibrational properties are characterized by the vibrational density of states (VDOS) and species-projected vibrational density of states. Since the VDOS can be

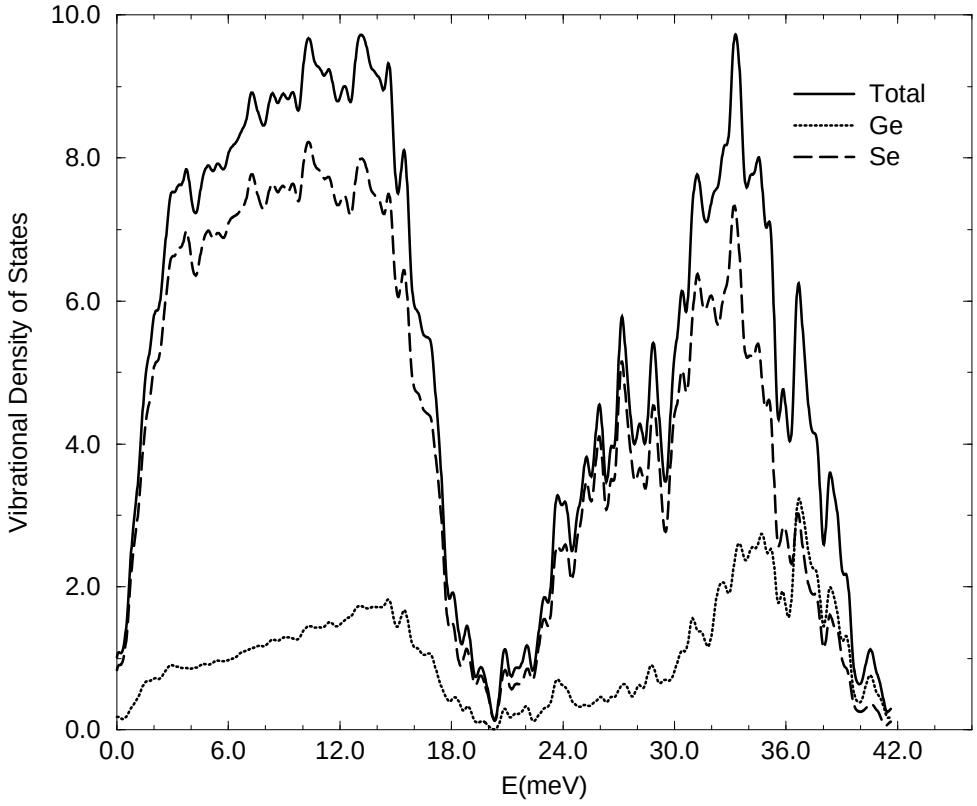

Figure 3.4: Vibrational density of states (solid lines) and species projected vibrational density of states for Se (dashed lines) and Ge (dotted lines) for g-$GeSe_4$.

determined through inelastic neutron scattering, it provides a straightforward test of our models. The method has been described in Chapter I.

$GeSe_4$ glass

The vibrational density of states is plotted in Fig. 3.4. We also plot the species-projected density of states for Se and Ge. Three bands can be distinguished: a low energy acoustic band which is strongly correlated to the connectivity of the network involving mainly extended inter-block vibrations and a high energy optic band which tends to strongly depend on the configurations of the building blocks, consisting of

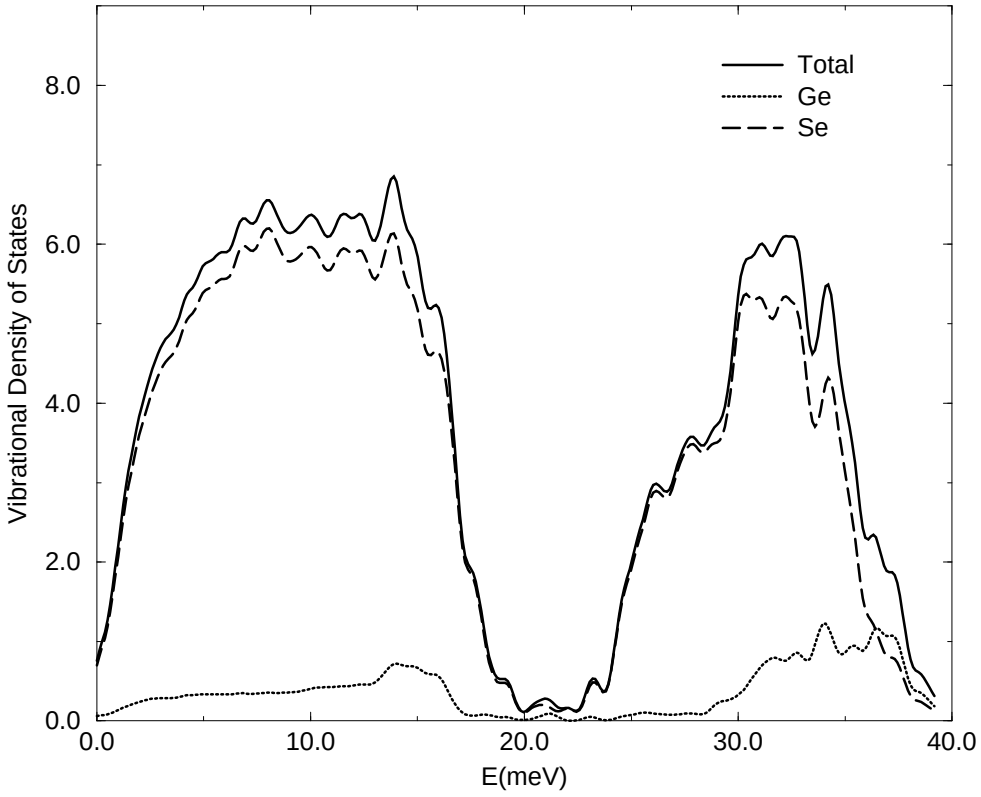

Figure 3.5: Vibrational density of states (solid lines) and species projected vibrational density of states for Se (dashed lines) and Ge (dotted lines) for g-$GeSe_9$.

more localized intrablock vibrations. The two main bands are clearly separated by the tetrahedral breathing (A_1-A_{1c}) band. The same features have been observed experimentally by Effey and Cappelletti [36], also by Kamitakahara et *al* [37]. Effey and Cappelletti concluded that the broad band below 20 meV (161.31 cm^{-1}) is dominated by modes extending widely over the entire network and not by modes localized on "molecular" features in the glass such as the tetrahedron giving rise to the A_1 mode. Low frequency and high frequency characteristics are well reproduced. The species projected VDOS for the Se atoms and Ge atoms clearly show that the Se atoms are responsible for most of the motion.

$GeSe_9$ glass

In Fig. 3.5 we display the calculated VDOS and the species projected density of states of g-$GeSe_9$. The VDOS can be divided mainly into two bands. The low-energy band goes up to 19 meV, and the high-energy band that decays near 40 meV. The shoulder around 19 meV and the sharp peak around 31 meV can be regarded, respectively, as the bond-bending and the bond-stretching vibrations. In the valley between the low-energy and the high-energy band, a feature arises at about 23.4 meV. This feature has been identified in Raman scattering measurements [38, 39] as an A_1 mode resulting from vibrations of Se atoms with their cross-linking Ge neighbors. This feature is absent in the spectrum of Se. Experimentally [37], it has been shown that the A_1 mode is a function of Ge concentration in the glass. As Ge concentration increases, the A_1 mode arises in the gap. Hence, it gives an explanation why the A_1 band in g-$GeSe_9$ (x=0.1) is weak compared to g-$GeSe_4$ (x=0.2) or g-$GeSe_2$ (x=0.33).

3.1.4 Electronic properties

The electronic properties of our models are analyzed through the electronic density of states (EDOS) and inverse participation ratio (IPR), which we denoted by $\mathcal{I}$. The EDOS was obtained by summing suitably broadened Gaussians centered at each eigenvalue. The IPR determines the localization of electronic eigenvalues (see Chapter I).

$GeSe_4$ glass

The calculated EDOS of g-$GeSe_4$ in Fig. 3.6 agrees quite well with experimental results obtained from x-ray photo-emission [40] (XPS). The substantial splitting between the first two peaks of the valence bands is also well-pronounced. The valence band exhibits three features. The two lowest bands between -15.64 eV and -6.5 eV originate from the atomic s-like states of Ge and Se. The next band contains p-like bonding states lying between -6.37 eV and -3.6 eV and predominantly p-like non-bonding states in the topmost valence region (our electronic eigenvalues have been shifted in order to place the valence band edge eigenvalue at zero).

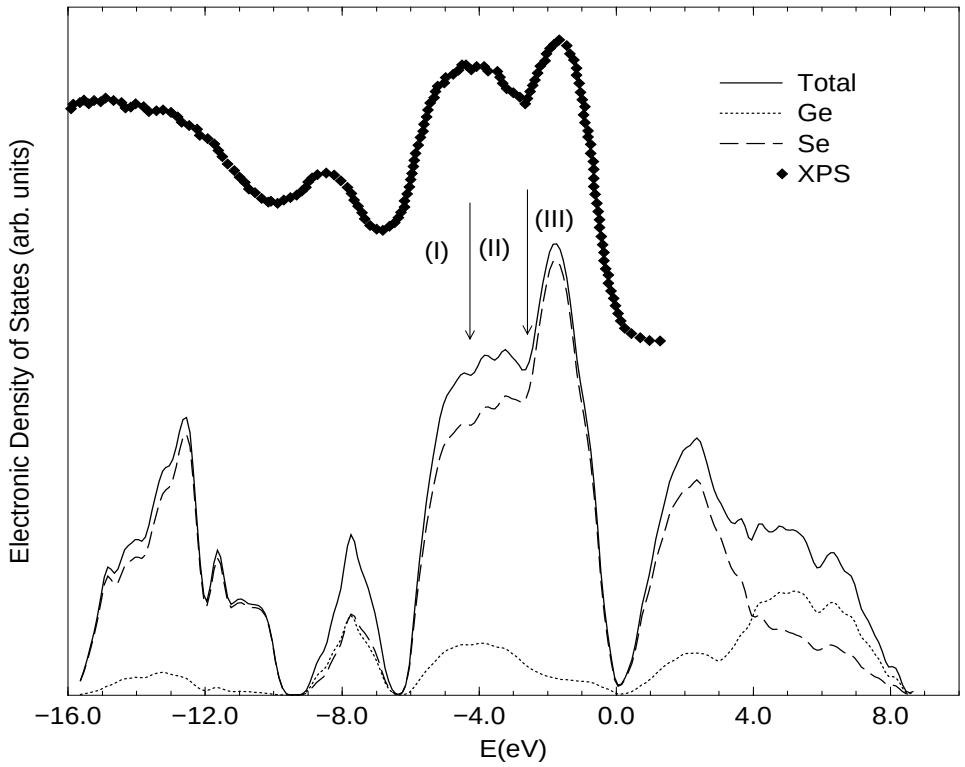

Figure 3.6: Electronic density of states (solid lines) and species projected electronic density of states for Se (dashed lines) and Ge (dotted lines) for g-$GeSe_4$ obtained from *ab initio* simulations (Gaussian broadened Kohn-Sham eigenvalues) and compared to the XPS [40] results. The Fermi level is at E=0.

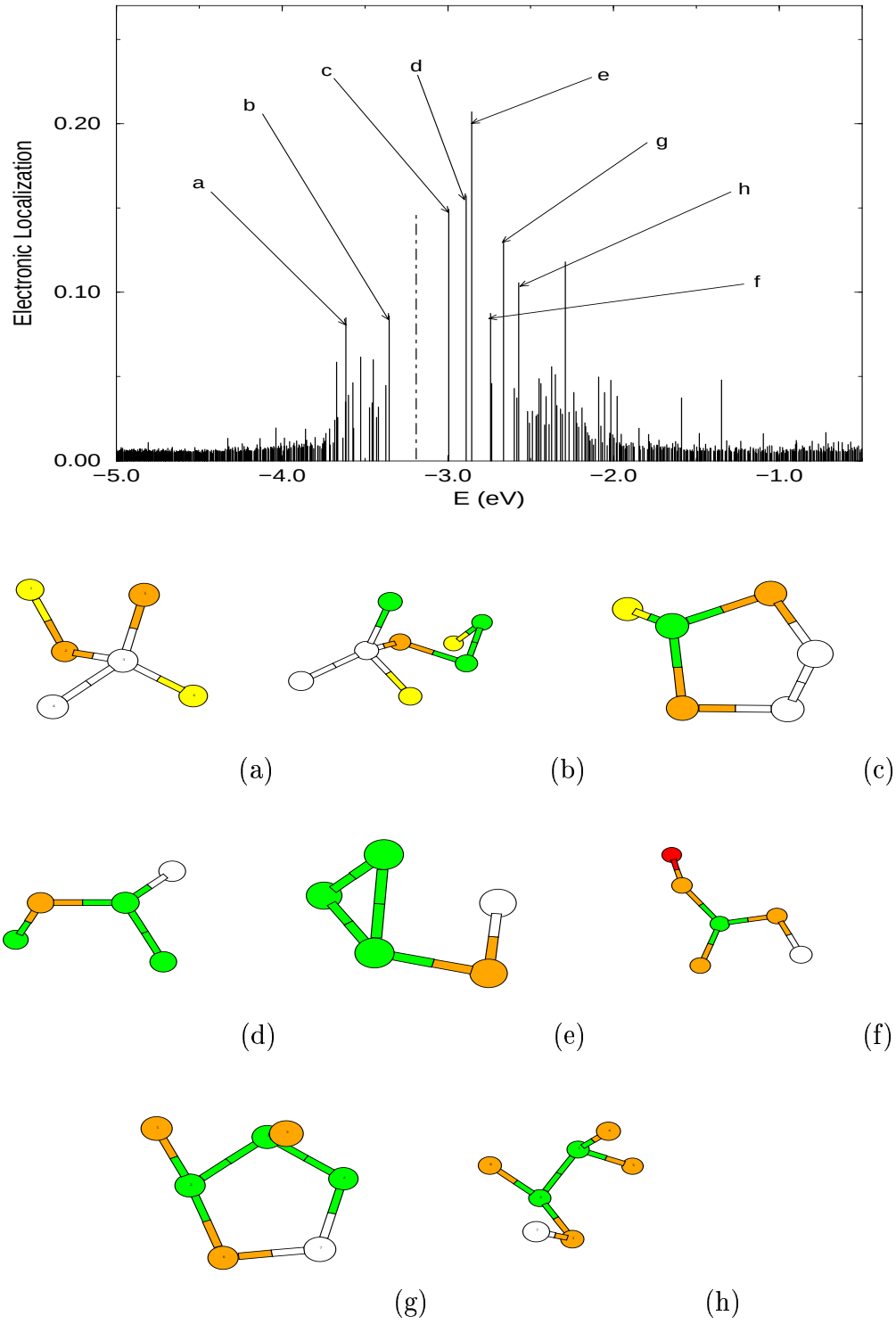

Figure 3.7: Inverse participation ratio along with the characteristic defect types causing localization of electronic eigenstates in the band gap region of g-$GeSe_4$. The vertical dotted lines indicates the position of the Fermi level. The color codes are defined as threefold Ge atoms (red), fourfold Ge atoms (white), threefold Se atoms (green), twofold Se atoms (orange), and onefold Se atoms (yellow).

The p band in g-$GeSe_4$ is represented by three distinct groups of peaks as indicated in the spectra of Fig. 3.6. The first group (I) contains all the bonding states whose energies fall within [-6.0, -4.09] eV. The second group (II) includes the bonding states with energies in [-4.09, -2.6] eV. The last group (III) is in the topmost region of [-2.6, 0.0] eV. There is a substantial splitting between groups (II) and (III) giving rise to two peaks. These characteristics have been observed in g-$GeSe_2$ [41] and have been named the A_1 and A_2 peaks respectively. By analogy to $GeSe_2$, the shoulder in group (I) has been identified as A_3 peak and the peak of the second lowest band as B peak. In Table 3.6 we compare the positions of the peaks in the EDOS to the experimental results of $GeSe_2$ [41].

In order to connect localized eigenstates to particular topological/chemical irregularities we plot in Fig. 3.7 the IPR in the band gap region along with the defect sites. It is valuable to know how the defect sites manifest themselves in the electronic eigenstates. A close look at the localized states at the band edges shows that the localized states at the top of the valence band are mostly associated with twofold and one-fold Se atoms with at least one homopolar bond, whereas the localization at the conduction band edge arises from over-coordinated (threefold) Se atoms involved with at least one homopolar bond and from twofold-coordinated Se atoms involved with at least one wrong bond. A detailed examination shows that the localization of the eigenstates is mostly due to Se-Se bonds - connected with some defect sites. Fig. 3.7 shows the typical defects structures causing the localization of eigenstates in the band gap region.

$GeSe_9$ glass

In Fig. 3.8 we plot the calculated EDOS and the species projected density of states of our model along with the XPS experimental results [40]. There is a good agreement between the experiment and the theory. All the relevant experimental features are found in the calculated EDOS, providing further support for the validity and accuracy of our model. The g-$GeSe_9$ EDOS is very close to the Se EDOS [42] other than the Ge bands. The species projected density of states show that Se atoms contribute most to the spectrum. Hence, the lowest bands [-15.0, -6.0] eV represent

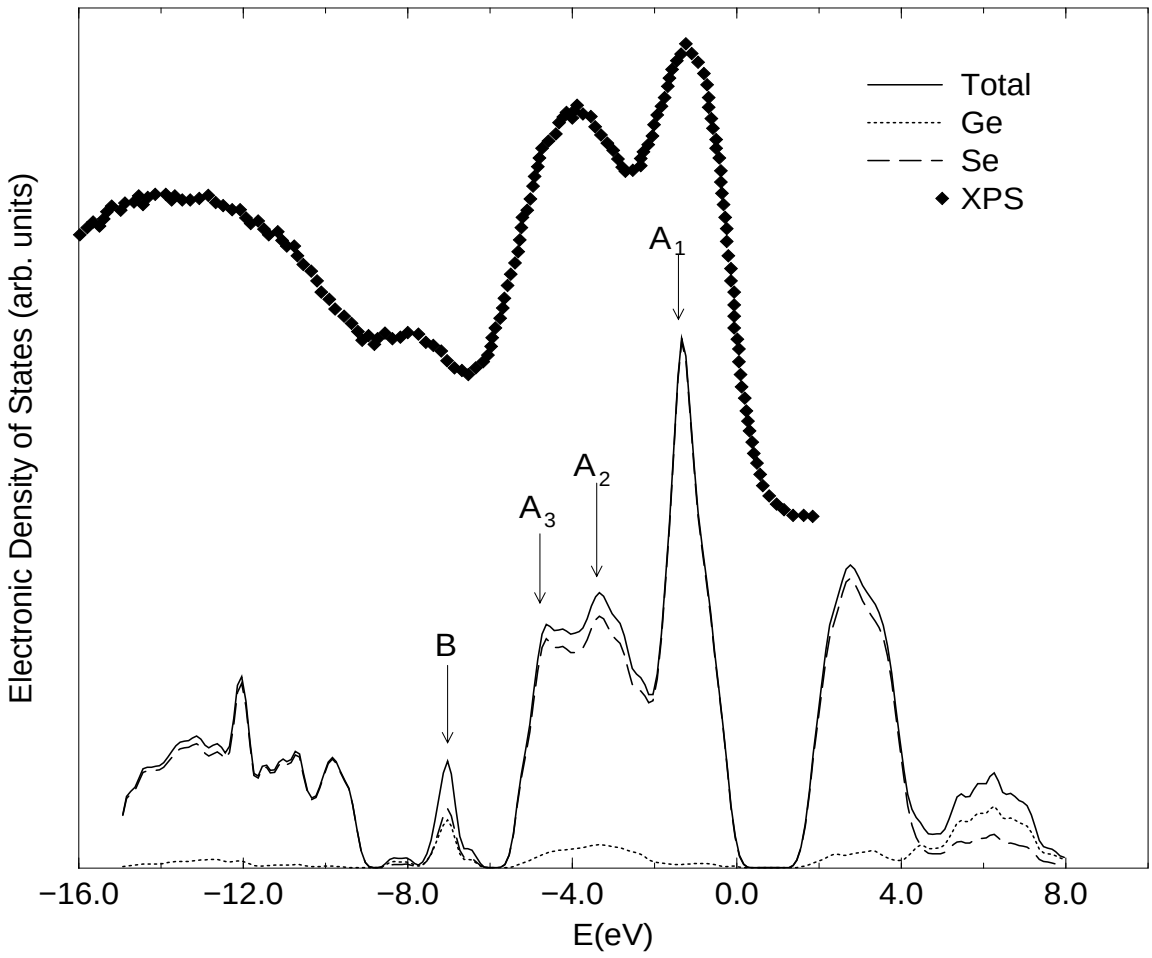

Figure 3.8: Electronic density of states (solid lines) and species projected electronic density of states for Se (dashed lines) and Ge (dotted lines) for g-$GeSe_9$ obtained from *ab initio* simulations (Gaussian broadened Kohn-Sham eigenvalues) and compared to the XPS [40] results. The Fermi level is at E=0.

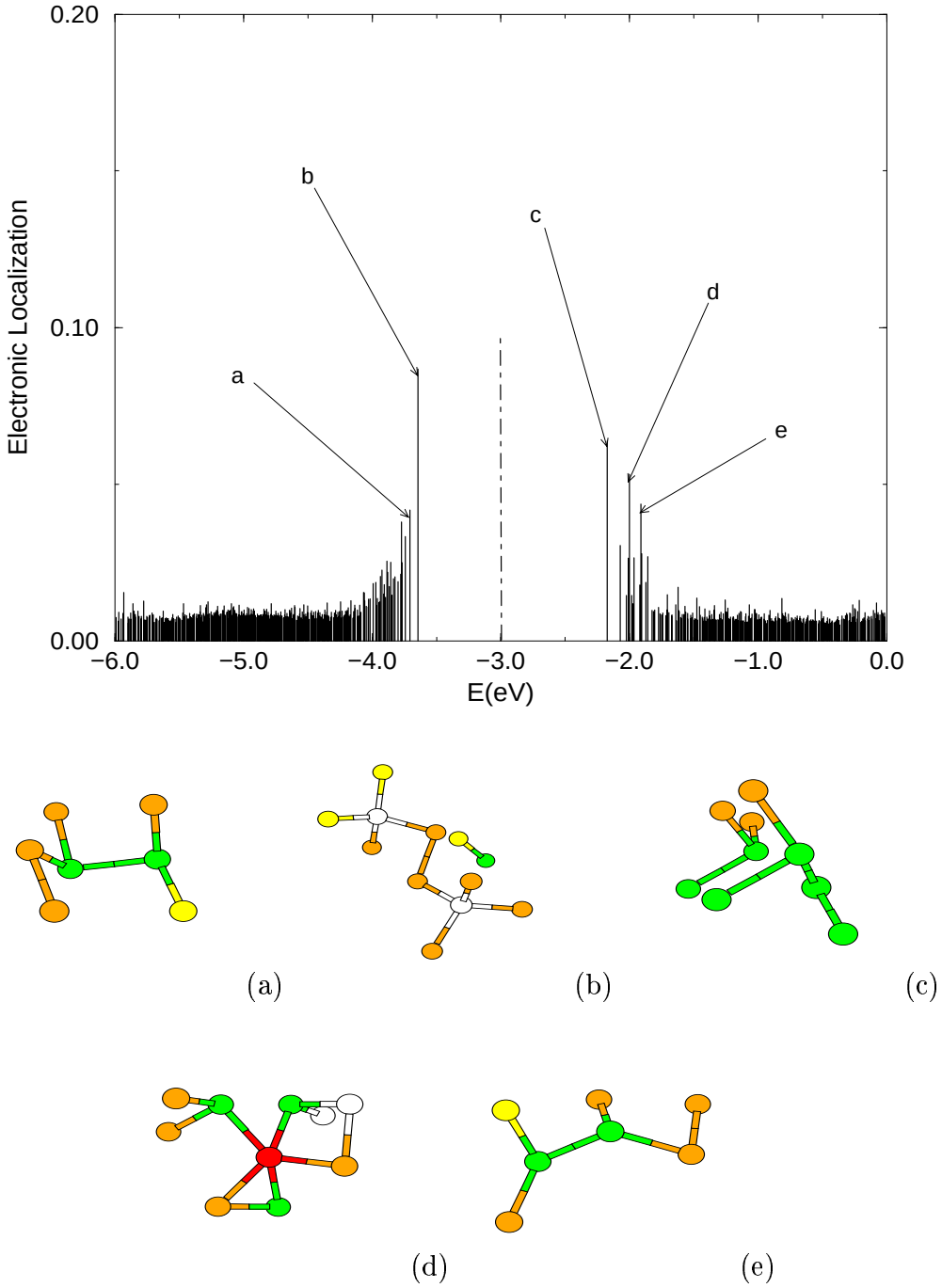

Figure 3.9: Inverse participation ratio along with the characteristic defect types causing localization of electronic eigenstates in the band gap region of g-$GeSe_9$. The vertical dotted lines indicates the position of the Fermi level. The color codes are defined as threefold Ge atoms (grey), fourfold Ge atoms (white), fivefold Ge atoms (red), threefold Se atoms (green), twofold Se atoms (orange), and onefold Se atoms (yellow).

Table 3.6: The positions of the A_1, A_2, A_3 and B peaks in the EDOS of $GeSe_4$ and $SiSe_2$ glasses compared to experimental results of $GeSe_2$ [41].

(eV)	A_1	A_2	A_3	B
Experiment $GeSe_2$	-1.38	-3.0	-4.6	-7.8
Quench from the melt $GeSe_4$	-1.7	-3.1	-4.6	-7.7
Quench from the melt $GeSe_9$	-1.36	-3.16	-4.62	-7.1

essentially the atomic s-like states of Se and Ge. The next band which lies between -6.0 and -2.2 eV contains p-like bonding states. Finally the topmost valence states are predominately nonbonding p-like in nature. Schlüter *et al* [42] have shown that the lower energy peak in the p-like bonding states of Se represents states involved in intrachain bonding whereas states in the higher energy peak of the p-like bonding states arise in part from hybridization and contribute to the inter-chain bonding in the crystal. This argument holds for our model due to the large contribution of Se in the EDOS. The calculated Γ point optical gap is of the order of 1.73 eV. It is rather interesting that there are no band-gap states in our EDOS. By analogy to g-$GeSe_2$, we can name the principal peaks as A_1, A_2, A_3, and B respectively. Their values are listed on Table 3.6.

In Fig. 3.9 we plot $\mathcal{I}$ along with the defect types causing localization of electronic eigenstates in the band gap region. The states near the band edge are well localized. It is found that the HOMO is localized on one-fold coordinated Se connected to threefold Se, and on Se_2 bridge tetrahedra units. The localization at the conduction band edge is partly due to the over-coordinated Se atoms associated with at least one Se-Se homopolar bonds, and one over-coordinated Ge atom connected to threefold Se atoms. In our g-$GeSe_9$ the electronic eigenstates are less localized compared to g-$GeSe_4$.

3.1.5 Composition-dependent trends in Ge_xSe_{1-x} glasses

Having fully analyzed the structural, vibrational and electronic properties of $GeSe_4$ and $GeSe_9$, we illustrate in this section the composition dependent trends in Ge_xSe_{1-x} glasses. Other studies on the composition dependence of the glass structure have been made using both direct and indirect methods, extended x-ray absorption fine structure (EXAFS)[33], x-ray emission [43] and Raman spectroscopy [38, 44, 45]. In both experiment and our work, the IRO associated with Ge-Ge correlations, which is manifested by an FSDP varies as a function of x (Ge concentration). In $GeSe_9$, this peak appears only as a shoulder as opposed to $GeSe_4$ where it is well pronounced. As x increases the intensity of the FSDP increases and reaches its maximum at x=0.33. Another relevant measure is the ratio of corner sharing (CS) to edge sharing (ES) tetrahedra as a function of x. The ratio of CS to ES tetrahedra increases with Ge concentration. In $GeSe_9$ (x=0.1) the structural motifs are Se-chain segments cross-linked by $Ge(Se_{1/2})_4$ with negligible ratio of CS to ES tetrahedra. The addition of Ge imposes the disappearance of Se chains and the existence of $Ge(Se_{1/2})_4$, and CS and ES tetrahedra.

The vibrational density of states of Ge_xSe_{1-x} glasses is also composition-dependent. Since the (A_1 - A_{1c}) band is associated to the breathing mode tetrahedra $Ge(Se_{1/2})_4$, it should vary as a function of Ge concentration. In $GeSe_9$, the A_1 band appears as a shoulder due to the small concentration of tetrahedra. As x increases, the A_1 mode arises in the gap.

In the same way the electronic density of states is a function of x. When x increases the intensity of the Ge band increases, but this band remains narrow. On the other hand, the width of the Se band remains constant, but its shape varies. The splitting between the A_1 and A_2 peaks becomes smaller, indicating the disappearance of Se chains.

This work supports the evidence of connectivity between the concentration of Ge, the atomic ordering associated with IRO, the (A_1 - A_{1c}) band, and the shape of the Ge and Se bands in Ge_xSe_{1-x} glasses.

3.2 Ge-Se-Ag Glasses

Metals and particularly Ag as an additive in base chalcogenide glasses Ge_xSe_{1-x} have attracted widespread interest in soft condensed matter science[46, 47]. The interest stems in part from the extensive bulk glass forming tendency in the Ge-Se-Ag ternary, from the spectacular enhancement (8 orders of magnitude) in electrical conductivity of these glasses with changing Ag content, and from light-induced effects such as photo-doping, photo-diffusion and photo-deposition. Although the mobile ions in amorphous materials have been a serious object of investigation[48] their dynamics in materials with disordered structure constitute one of the major unsolved problems in the field of solid state ionics. In addition their physical properties change continuously with change in chemical composition. Beside their practical application in memory devices[49], these materials can be used as model systems to study the effect of mobile ion content on ionic transport, as well as the relationship between the short and intermediate range order in the glass, on the one hand, and its transport properties, on the other[50]. The structure of the Ge-Se-Ag glasses has been investigated using several experimental methods, including X-ray diffraction[51, 52] neutron diffraction with isotopic substitution[53], EXAFS[54], differential anomalous X-ray scattering (DAS)[55, 56, 57] and Modulated Differential Scanning Calorimetry (MDSC) and Raman spectroscopy[46, 47]. Despite this large database, the structure of the ternary Ge-Se-Ag glasses has not yet been completely determined. There continues to be a debate on basic aspects of the glass structure (i.e. homogeneity and Ag coordination) especially for Se rich glasses with more than 67% Se. We focused on Ag-doped glasses containing Ge 25 at.% and Se 75 at.% that we label later as $GeSe_3$ which is of special practical interest since as mentioned earlier they present a backbone that is not aging and thus can contribute to formation of memory or other type of devices with very high reliability.

3.2.1 Model generation

Energy functional and interatomic forces

For the simulations reported in this section, we use FIREBALL2000 (discussed in Chapter 2) developed by Lewis and coworkers[25]. The exchange-correlation energy was treated within the LDA, using the results of Ceperley and Alder[58], as interpolated by Perdew and Zunger[59] (more intricate gradient corrected functionals are available if needed). The pseudopotential and pseudoatomic wave functions were generated in the Troullier-Martins form[60] employing the scheme of Fuchs and Scheffer[61].

Model formation

The models described here were generated using the conventional melt quenching method. We began by randomly placing atoms in a cubic supercell according to the desired composition [for $(GeSe_3)_{0.90}Ag_{0.10}$ 54 germanium atoms, 162 selenium atoms and 24 silver atoms; for $(GeSe_3)_{0.85}Ag_{0.15}$ 51 germanium atoms, 153 selenium atoms and 36 silver atoms] with the minimum acceptable distance between atoms 2 Å. The size of the cubic cells was chosen to make the density of these glasses close to experimental data. The box size of the 240 atom supercell of $(GeSe_3)_{0.90}Ag_{0.10}$ and $(GeSe_3)_{0.85}Ag_{0.15}$ are respectively 18.601 Å and 18.656 Å with corresponding density[52] 4.98 g/cm^3 and 5.03 g/cm^3. The structures were annealed and we obtained well thermalized melts at 4800 K. We took three steps to cool down the cells. First, the cells were equilibrated and cooled to 1100 K for 3 ps; then they were slowly cooled to 300 K for approximately 5 ps. The MD time step was 2.5 fs. Simple velocity rescaling was used for the dissipative dynamics. In the final step, the cells were steepest descent quenched to 0 K and forces smaller in magnitude than 0.02 eV/Å. All calculations were performed at constant volume using the Γ point to sample the Brillouin zone in order to compute energies and forces.

The use of MD to quench a model liquid is natural and *in principle* completely general, since it superficially mimics the process of glass formation. It has been utilized for structural calculations for $GeSe_2$[62], As_2Se_3[63], Ge-Se-Ag[64] and other

Table 3.7: Basic short range order parameters in models g-$(GeSe_3)_{0.90}Ag_{0.10}$ and g-$(GeSe_3)_{0.85}Ag_{0.15}$ and compared to available data. r_1 is the average bond length, $\bar{n}$ the average coordination number, and r_2 the second nearest neighbor distance. [a] Analytical calculation. [b] Monte Carlo method.

	Glass	r_1 (Å)	r_2 (Å)	$\bar{n}$
This Work	x=0.10	2.47±0.01	3.78±0.01	2.525±0.01
	x=0.15	2.48±0.01	3.82±0.01	2.775±0.01
Experiment[52]	x=0.10	2.46±0.02	3.80±0.05	2.471±0.002[a] 2.543±0.100[b]
	x=0.15	2.48±0.02	3.82±0.05	2.855±0.002[a] 2.852±0.100[b]

systems (though there are often hints that there is too much "liquid-like" character to the quenched models). With accurate force calculations, it has produced rather disappointing results for highly non-stoichiometric liquids such as GeSe[65] and ternary glasses such as AsGeSe[66]. We believe that the success with $(GeSe_3)_{1-x}Ag_x$ (x=0.1, 0.15) glasses is connected to the fact that we are in a weakly overconstrained glass forming part of the vibrational phase diagram[67]. The "cook and quench" method is less effective in the highly overconstrained regime. It is likely that hybrid schemes mixing experimental information and *ab intio* simulation (such as the "ECMR" method[68]) would be most effective in this composition regime.

3.2.2 Structural properties

Structural information can be extracted from the static structure factor S(Q) measured in scattering experiments and the pair correlation function $g(r)$, which is related to S(Q) via Fourier transform.

Short range order and defects

We define short range order (SRO) as order on length scale not longer than the second nearest neighbor distance. To analyze the SRO in our models, we study different parameters including bond length, coordination number, etc. Table 3.7 gives

Table 3.8: Nearest-neighbors distances in $(GeSe_3)_{0.90}Ag_{0.10}$ (x=0.10) and $(GeSe_3)_{0.85}Ag_{0.15}$ (x=0.15) glasses.

	correlation	Distance (±0.03 Å)	Ref. [52] (±0.05 Å)
x=0.10	Ge-Ge	2.38	
	Ge-Se	2.37	2.37
	Ge-Ag	2.35	
	Se-Se	2.36	2.37
	Ag-Se	2.63	2.67
	Ag-Ag	3.10	3.05
x=0.15	Ge-Ge	2.38	
	Ge-Se	2.37	2.37
	Ge-Ag	2.35	
	Se-Se	2.36	2.37
	Ag-Se	2.63	2.67
	Ag-Ag	3.21	3.05

an overview of the SRO in g-$(GeSe_3)_{0.90}Ag_{0.10}$ and g-$(GeSe_3)_{0.85}Ag_{0.15}$. The average bond length and average coordination number closely agree with the available data[52]. With increasing Ag concentration, the average coordination number increases to 2.8 in g-$(GeSe_3)_{0.85}Ag_{0.15}$ from 2.51 in g-$GeSe_3$[26]. Also listed is the second nearest neighbor distance. Table 3.8 lists the average bonding distances of different bonds present in the model. Different values of the Ag-Ag bond distance have been proposed. Using the differential anomalous scattering (DAS), Westwood *et al*[57] obtained a value of 3.35 Å for the Ag-Ag distance, a bit longer than our observation or other data[52].

Both models contain structural defects. In addition to the normally coordinated Ge_4 and Se_2: Ge_3, Se_3 and Se_1 are present in both models. Table 3.9 summarizes the statistical distribution of the main structural components. A look at the table shows that Ge-Se, Se-Se, Ag-Se and Ag-Ge correlations depend upon x with additional Ag

Table 3.9: The statistical distribution of the main structural components in g-$(GeSe_3)_{0.90}Ag_{0.10}$ (x=0.10) and g-$(GeSe_3)_{0.85}Ag_{0.15}$ (x=0.15) models. Percentage of a given component in the total configuration is given in parentheses. Here the subscript number indicates the coordination number. For example, Ag_2 means the two-bonded Ag sites.

	g-$(GeSe_3)_{0.90}Ag_{0.10}$	g-$(GeSe_3)_{0.85}Ag_{0.15}$
Ge_4	35 (65%)	34 (66.7%)
Ge_3	17 (31.5%)	13 (25.5%)
Se_2	86 (53.1%)	85 (55.6%)
Se_3	56 (33.9%)	57 (37.2%)
Se_1	17 (11.8%)	11 (7.2%)
Ag_2	24 (100%)	31 (86.1%)
Ag_3	-	4 (11.1%)
Ge-Se	64%	57.1%
Se-Se	21%	19.2%
Ag-Se	13%	18.2%
Ag-Ge	1.5%	5.2%

modifying the Ge-Se and Se-Se bonding. By integrating the partial pair correlation function $g_{\alpha\beta}(r)$ (Fig. 3.13), we estimate the average coordination number of Ag in the models. We found an average coordination of 2.0 and 2.9 in g-$(GeSe_3)_{0.90}Ag_{0.10}$ and g-$(GeSe_3)_{0.85}Ag_{0.15}$ respectively. We note that this is hard to estimate without ambiguity because of the lack of a well-defined deep minimum in $g(r)$ after the first peak especially for the x=0.15 model.

When discussing the coordination of Ag we can follow the arguments of Kastner[69] who was the first to describe the bonding of metal atoms in chalcogenide glasses. However, we have to consider the fact that in addition to the covalent bond that is expected to form with the chalcogens, Ag offers three empty $s-p$ orbitals and is surrounded by the lone-pair electrons of its chalcogen neighbors. The latter offer the opportunity for the formation of up to three coordinate bonds. A coordinate bond is similar to a covalent bond and has similar strength but the bonding electrons are supplied by one bonding partner (the chalcogen atom)[70]. As a result, the lowest energy-bonding configuration for Ag in chalcogenide glasses is an overall neutral complex with Ag positively charged with the negative charge located on neighboring chalcogen or chalcogens[71]. The coordination of Ag thereby can vary but the expected value would be in average close to three - with one covalent bond and up to 2 coordinated bonds. The opportunity for four-fold coordination also exists as there is one more free $s-p$ orbital at the Ag atom but evidently this does not satisfy the requirements of the lowest energy configuration and the electronegativity of the entire complex in the presence of other cations in the system so that the probability for this type of bonding is lower. Our simulations appear to be consistent with these chemical considerations, as all of the Ag is two-fold in the 10% model, with the addition of three-fold Ag in the 15% Ag model.

Intermediate range order

Fig. 3.10 shows the calculated static structure factors for $(GeSe_3)_{0.90}Ag_{0.10}$ and $(GeSe_3)_{0.85}Ag_{0.15}$ and the comparison with the experimental data from ref. [52]. As we did not include *a priori* information in the model formation process, the fact that the peak positions and most spectral weight of S(Q) agree well with experimental data

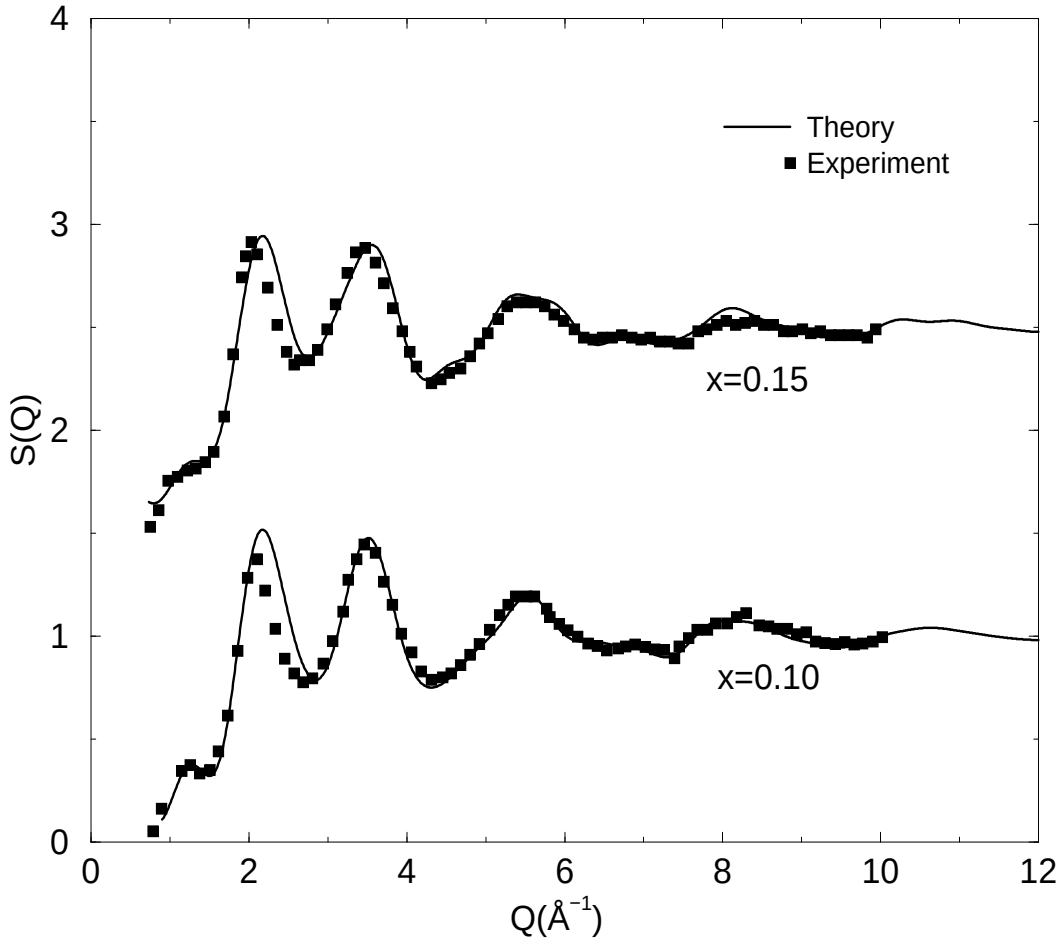

Figure 3.10: Total structure factor S(Q) of $(GeSe_3)_{0.90}Ag_{0.10}$ and $(GeSe_3)_{0.85}Ag_{0.15}$ glasses compared to experiment[52].

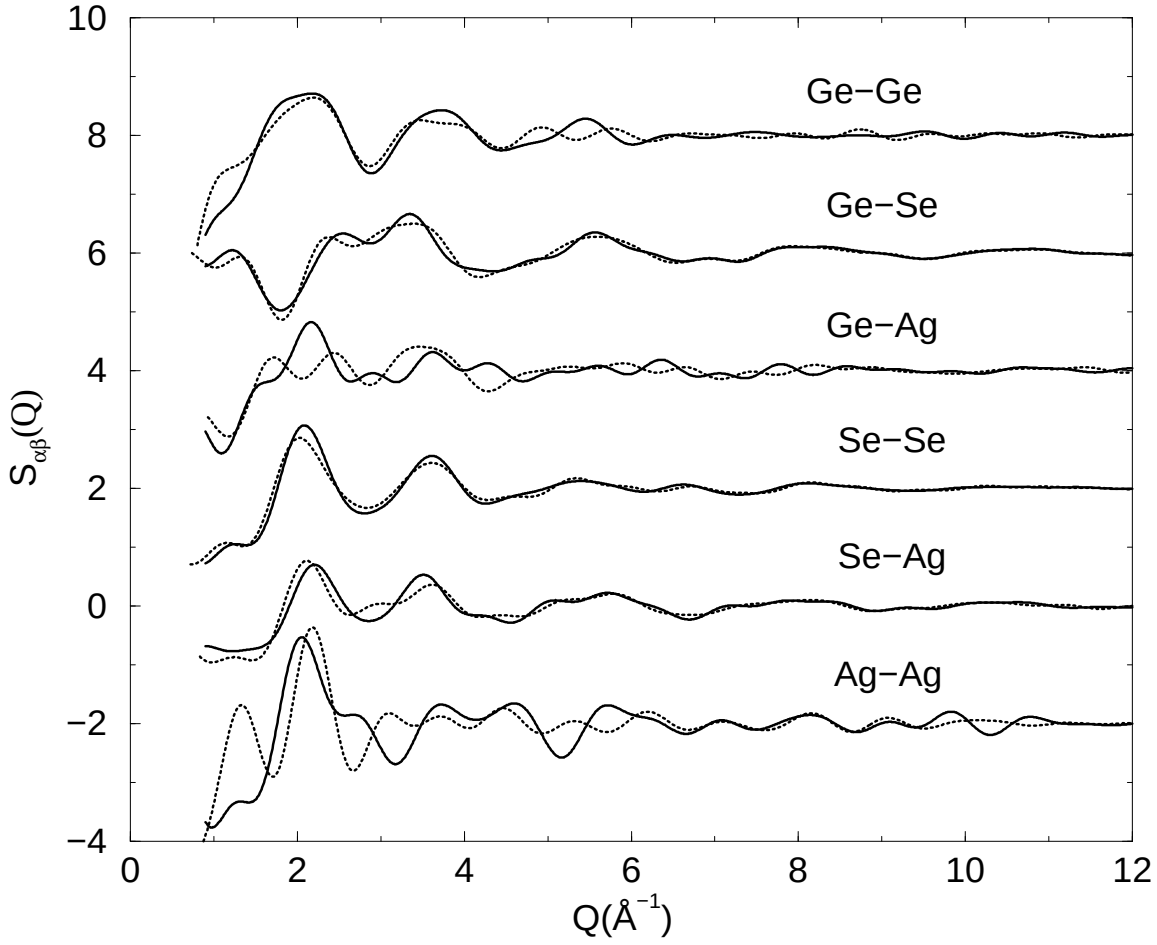

Figure 3.11: Partial structure factors $S_{\alpha\beta}(Q)$ of $(GeSe_3)_{0.90}Ag_{0.10}$ (solid lines) and $(GeSe_3)_{0.85}Ag_{0.15}$ (dotted lines) glasses.

is encouraging. The third and fourth peaks are a result of the short range order in the models. The position of the second peak does not depend on the Ag concentration (though its width does). This peak is located at Q≅2.09 $Å^{-1}$ in both models. By contrast the third peak decreases with increasing Ag. This peak is located at Q≅3.49 $Å^{-1}$ in $(GeSe_3)_{0.90}Ag_{0.10}$ and at Q≅3.41 $Å^{-1}$ in $(GeSe_3)_{0.85}Ag_{0.15}$; whereas in $GeSe_3$ (x=0, concentration of Ag in $(GeSe_3)_{1-x}Ag_x$) this peak appears near[52, 26] 3.53 $Å^{-1}$. In Fig. 3.11 the partial structure factors show that $S_{GeGe}(Q)$ and $S_{GeSe}(Q)$ tend to cancel each other.

Both models reveal a feature in S(Q) near 1.07 $Å^{-1}$. This is a harbinger of a First Sharp Diffraction Peak (FSDP), that becomes explicit in more Ge-rich materials. Piarristeguy *et al*[52] show that this peak varies as a function of Ag content. As Ag concentration increases, the FSDP decreases due to a change of the IRO. Moreover, Ag disturbs the $GeSe_{4/2}$ network, and leads to the fragmentation of $GeSe_{4/2}$ tetrahedrons. From the partial structure factors it is apparent that the "proto-FSDP" has contributions from all of the partials. To elucidate the intermediate range order more quantitatively, we have used the wavelet-based methods of Harrop and coworkers[72]. This is a promising scheme for interpreting structure factor data based upon continuous wavelet transforms[73] (CWT). In Fig. 3.12, we illustrate the results of the wavelet analysis extracted from the experimental data[52]. The most obvious feature is the extended range real-space correlations associated with the diffraction peak near 3.5$Å^{-1}$ for the 10% Ag model. This is connected to the narrowness of the peak for the 10% glass relative to the 15% material: in the latter case the correlations disappear by about 15$Å^{-1}$, whereas the correlations extend to at least 25 Å for the 10% glass. A similar state of affairs also accrues for the peak near 5.5$Å^{-1}$ and for a similar reason. This work emphasizes that simple associations of the reciprocal of the peak position of the FSDP to real-space length scales is misleading, particularly if the peak is narrow as discussed by Uchino and coworkers in studies of silica glass[72].

In Fig. 3.13 we plot the partial pair correlation function of both models. The Ge-Se and Se-Se pairs provide the dominant contribution to the first shell of the pair correlation function $g(r)$ whereas Ag-Se contribute to the second peak, Ag-Ag to the third and Se-Se (second nearest neighbors) to the fourth peak.

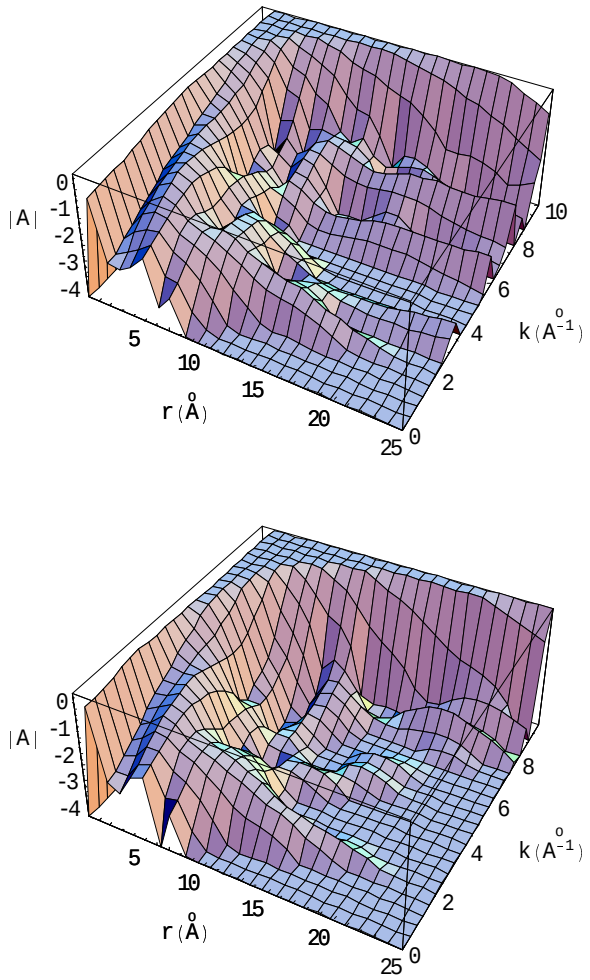

Figure 3.12: Three-dimensional $r - k$ diagrams of the instantaneous amplitude A of the continuous wavelet transform of the experimental structure factors[52] for $(GeSe_3)_{0.90}Ag_{0.10}$ (top) and $(GeSe_3)_{0.85}Ag_{0.15}$ (bottom) glasses, using the methods of Harrop and coworkers[72]. On the z-axis read Log|A| instead of |A|.

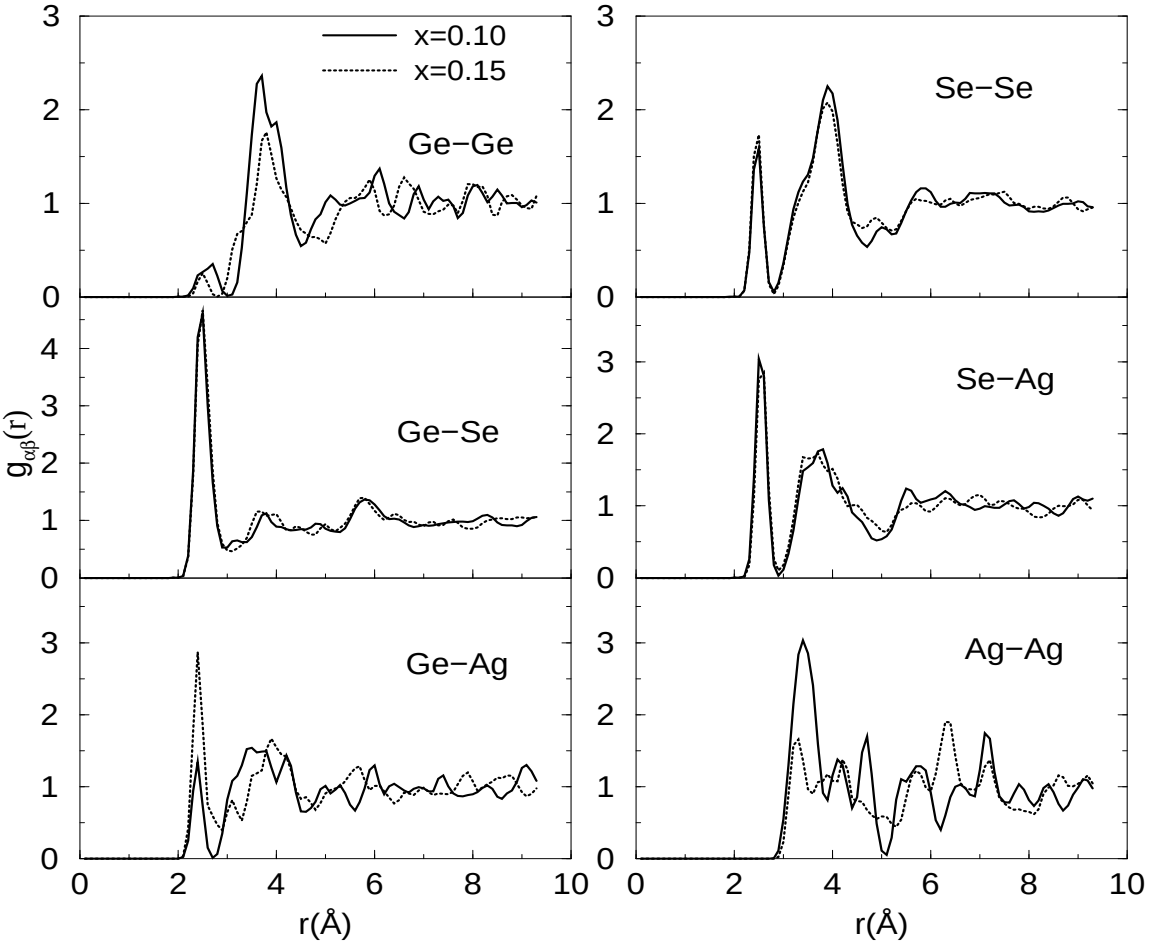

Figure 3.13: Partial pair correlation functions $g_{\alpha\beta}(r)$ of $(GeSe_3)_{0.90}Ag_{0.10}$ (solid lines) and $(GeSe_3)_{0.85}Ag_{0.15}$ (dotted lines) glasses.

3.2.3 Electronic properties

Having studied structural properties, we now analyze electronic properties of our models. Since structural and electronic properties are intimately related, an examination of electronic density of states provides additional insight about the properties of these materials. The electronic density of states (EDOS) of both models are calculated and analyzed by the inverse participation ratio $\mathcal{I}$ (IPR). The EDOS are obtained by convoluting each energy eigenvalue with suitably broadened Gaussian. In Fig. 3.14 we report the calculated EDOS and the species projected density of states of $(GeSe_3)_{0.90}Ag_{0.10}$ and $(GeSe_3)_{0.85}Ag_{0.15}$ glasses. It should be noted that the spectra of both models are very similar and closely related to the EDOS of Ge_xSe_{1-x} ($x > 0.15$). With the addition of Ag into g-$GeSe_3$, an intense peak, due to the Ag $4d$ electrons appears at about -3.47 eV as shown in Fig. 3.14. The valence band exhibits three features. The two lowest bands between -14.8 eV and -7.0 eV originate from the atomic $4s$-like states of Ge and Se partially hybridized to form bonding states to Ag atoms. The next band lying between -7.0 and 0.0 eV contains p like bonding states of Ge and Se and d like bonding states of Ag. The peak in the topmost valence region is due to the lone-pair $4p$ electrons of Se atoms. The Γ point optical gaps of g-$(GeSe_3)_{0.90}Ag_{0.10}$ and g-$(GeSe_3)_{0.85}Ag_{0.15}$ are respectively of the order of 1.20 and 1.26 eV. As the Ag content increases, the optical band gap increases. A plausible explanation of the variation of the optical gap could be explained by assuming that Ag atoms may intercalate between the layered structure of $GeSe_3$ rather than destroying it and forming a new band. To our knowledge, experimental information about the EDOS of both models is unavailable, so the curve in Fig. 3.14 is actually a *prediction.* This is an interesting contrast to the work of Simdyankin and coworkers[74], who show that for *low* concentrations of Cu, the gap *decreases* with addition of Cu in AsS and AsSe glasses. Care is needed in comparing these results since the hosts and transition metals are different, and our models have far higher metal content.

In order to connect localized eigenstates to particular topological/chemical regularities we plot in Fig. 3.15 the IPR in the band gap region. We found that the localization in the valence band is mainly due to Se atoms and in the conduction band to Ge atoms in both models. A close look at the localized states at the band edges

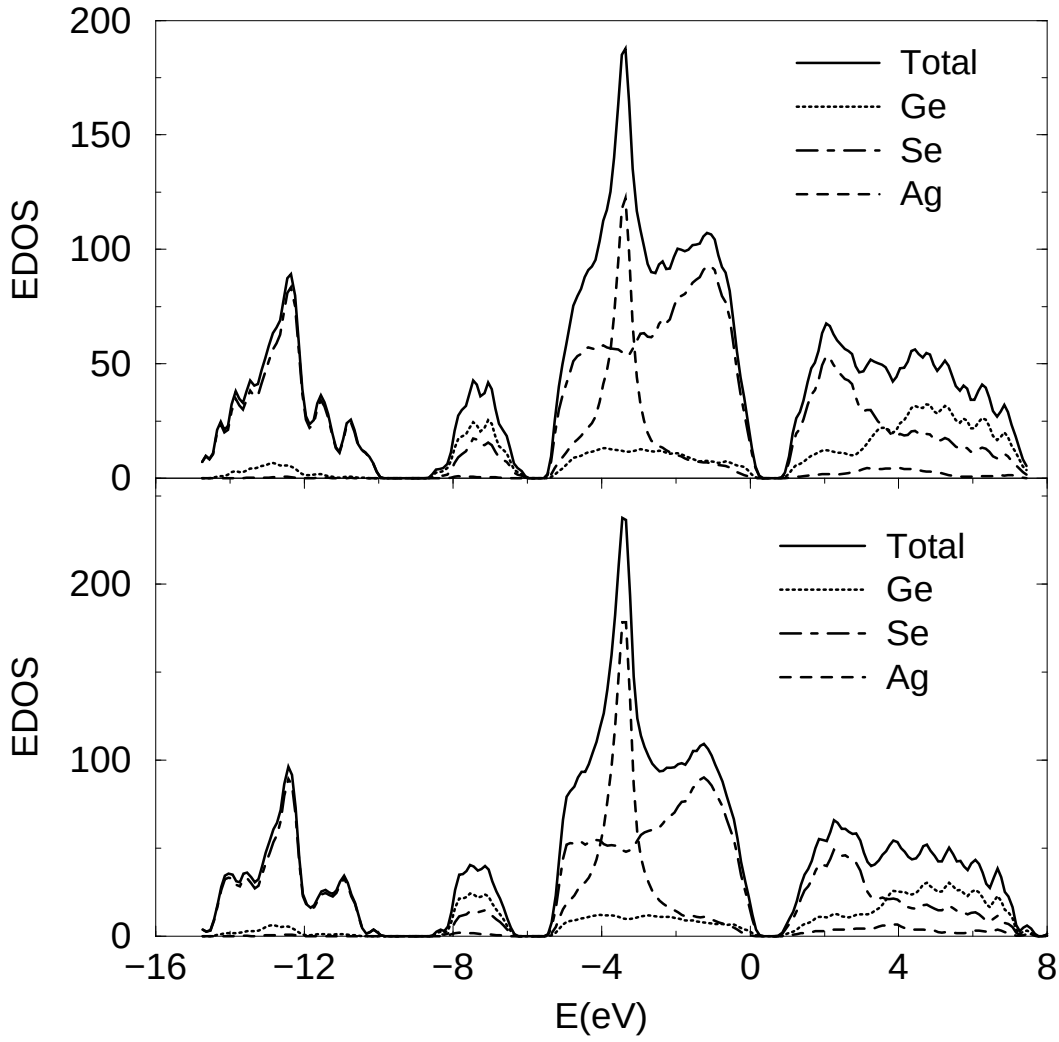

Figure 3.14: Electronic density of states and species projected electronic density of states for Se, Ge, and Ag for $(GeSe_3)_{0.90}Ag_{0.10}$ (top panel) and $(GeSe_3)_{0.85}Ag_{0.15}$ (bottom panel) glasses.

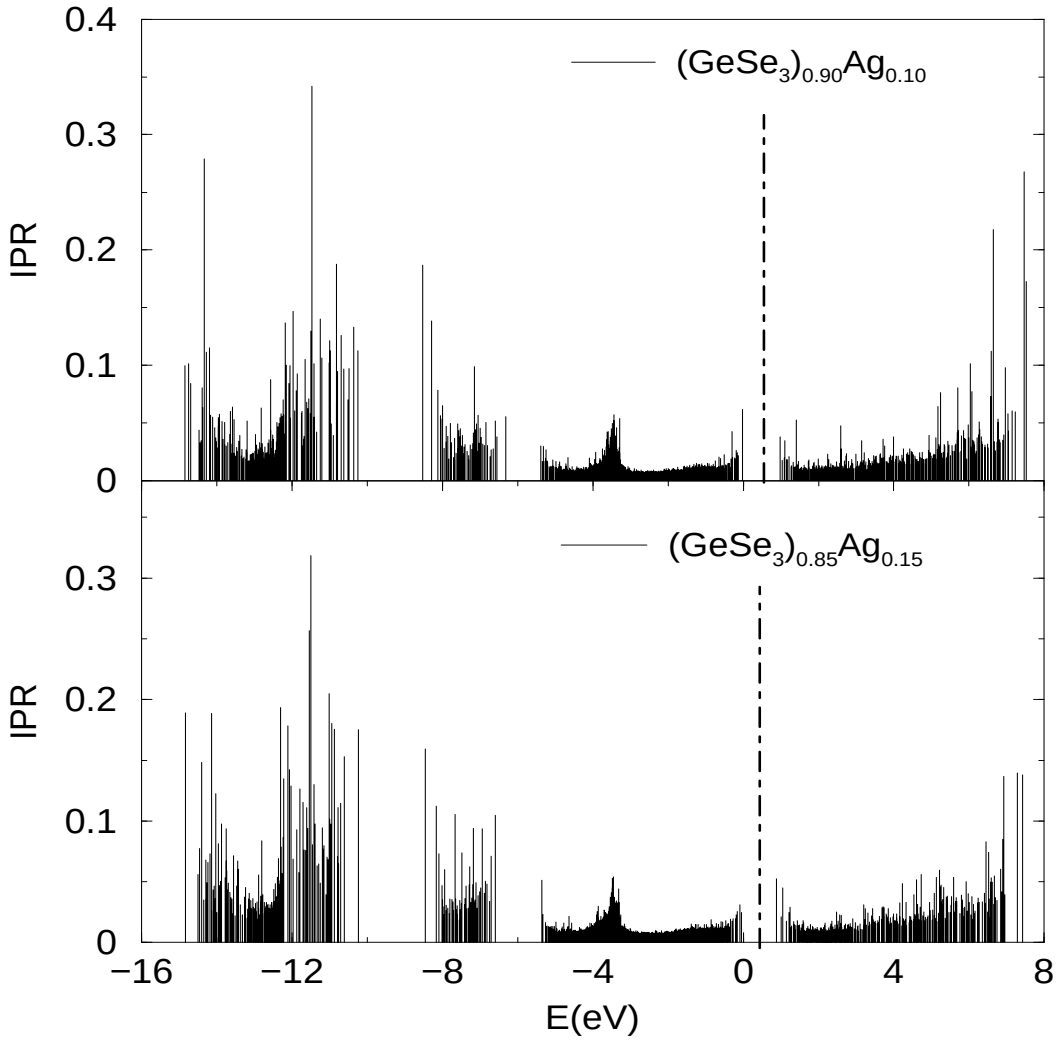

Figure 3.15: IPR of $(GeSe_3)_{0.90}Ag_{0.10}$ (top panel) and $(GeSe_3)_{0.85}Ag_{0.15}$ (bottom panel) glasses. The vertical dot-dashed line indicates the position of the Fermi level.

shows that the localized states at the top of the valence band of g-$(GeSe_3)_{0.90}Ag_{0.10}$ are mostly associated with two- and three-fold coordinated Se atoms with homopolar bonds, whereas the localization at the conduction band edge arises from overcoordinated Se associated with homopolar bonds and four-fold coordinated Ge connected to Se atoms involved with Se-Se homopolar bonds. By contrast, the top of the valence band of g-$(GeSe_3)_{0.85}Ag_{0.15}$ is quite extended; the conduction band edge shows very few localized states due to the overcoordinated Ge and Se. This explains the results of Kawasaki[75] showing dominance of the ionic conductivity related to Ag ions at these particular compositions.

3.2.4 The dynamics of silver ions

Diffusion of Ag in chalcogenide glasses is of special interest because of its great technological importance. This is related to the fact that the glass network holding Ag ions is very flexible. No matter how high the Ag coordination is, it forms only 1 covalent bond with its chalcogenide neighbors. So Ag ions can move to a new position without breaking the coordinate bond because the 2 sets of lone-pair electrons can rotate in the plane normal to the covalent bond. One other factor contributing to the high diffusivity of Ag is its high quadrupolar defomability[71]. A qualitative characteristic of Ag diffusivity in the particular compositions regarded in this work can be achieved by estimating the mean square displacement (MSD) function.

The mean-square displacement (MSD) functions for all of the atomic constituents of an ion-exchanged glass is defined by

$$\langle r^2(t)\rangle_\alpha = \frac{1}{N_\alpha}\sum_{i=1}^{N_\alpha}\langle|\vec{r_i}(t) - \vec{r_i}(0)|^2\rangle \tag{3.1}$$

where the time averaging is to be understood as an average over time and the summations are over atomic constituents. The MSD were calculated for Ge, Se and Ag ions for both models and are shown in Fig. 3.16. The MSD of Ag ions increases rapidly with time, whereas that of the Ge and Se show a very slight slope. We chose a temperature of 1000 K to illustrate the diffusion, and later discuss behavior at selected temperatures.

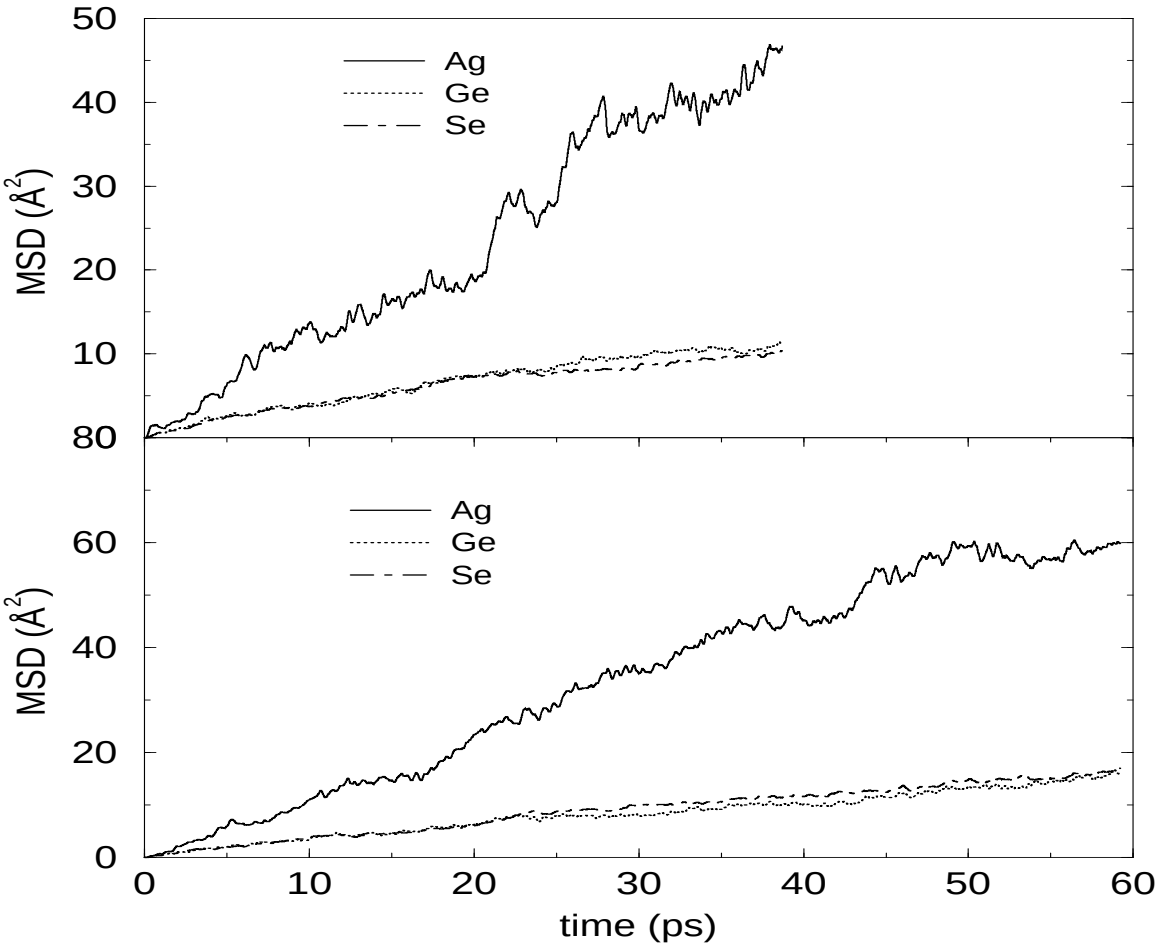

Figure 3.16: Mean square displacement for all of the atomic species in $(GeSe_3)_{0.90}Ag_{0.10}$ (top panel) and $(GeSe_3)_{0.85}Ag_{0.15}$ (bottom panel) glasses simulated at T=1000 K.

To explain the mechanism of diffusion of silver, we examine the trajectories of these particles. We obtained 2.5×10^4 steps of time development, for a total time of 62.5 ps and a fixed temperature of 1000 K. Fig. 3.17 illustrates 2D projections of trajectories of the most and least mobile Ag atoms in the x=0.15 model. We notice that for short times, the MSD of the most mobile atoms increases due to the diffusive motion of Ag. At intermediate time scales, the atoms may be trapped in a cage formed by their neighbors, and at the longest times we can explore, they can escape such traps and diffuse again. Thus our trajectories can largely be separated into vibration around stable trapping sites and hops between such sites. In both glasses, a fraction of Ag atoms do move large distances (see Fig. 3.18). In $(GeSe_3)_{0.90}Ag_{0.10}$, about 91.67 % of silver atoms move on an average distance greater than 2.5 Å for a time scale of 39 ps. Among them 25 % have an average displacement greater than 5 Å. By contrast only 4.2 % of Ag atoms move less than 2 Å. On the other hand, about 89 % of Ag atoms move on an average distance greater than 2.5 Å in $(GeSe_3)_{0.85}Ag_{0.15}$ for the same period of time. 36.1% of those atoms have an average displacement greater than 5 Å. The most mobile Ag atoms move on an average distance of 8.2 Å. These numbers illustrate the high ionic mobility of Ag ions in these complex glasses and are suggestive for a significant contribution of correlated hops of Ag^+ in the diffusion process.

Based on these trajectories, thermal transport coefficients such as diffusion coefficients can be evaluated. Generally one either uses the Green-Kubo formula [76] where the velocity autocorrelation (VAC) is integrated overtime or the Einstein relation [76] where the MSD is differentiated with respect to time. Since transport coefficients are equilibrium properties, the system must be properly thermalized before the transport properties can be estimated. Our simulations show that at time t>4 ps the systems are well equilibrated. The Einstein relation for self-diffusion reads:

$$\langle|\vec{r}(t)-\vec{r}(0)|^2\rangle = 6Dt + C \tag{3.2}$$

where C is a constant, D is the self-diffusion coefficient and $\langle|\vec{r}(t)-\vec{r}(0)|^2\rangle$ is the mean-square distance from initial position at time t, averaged over atoms of a given species. Direct simulation of the atomic trajectory and simple fitting yields C and

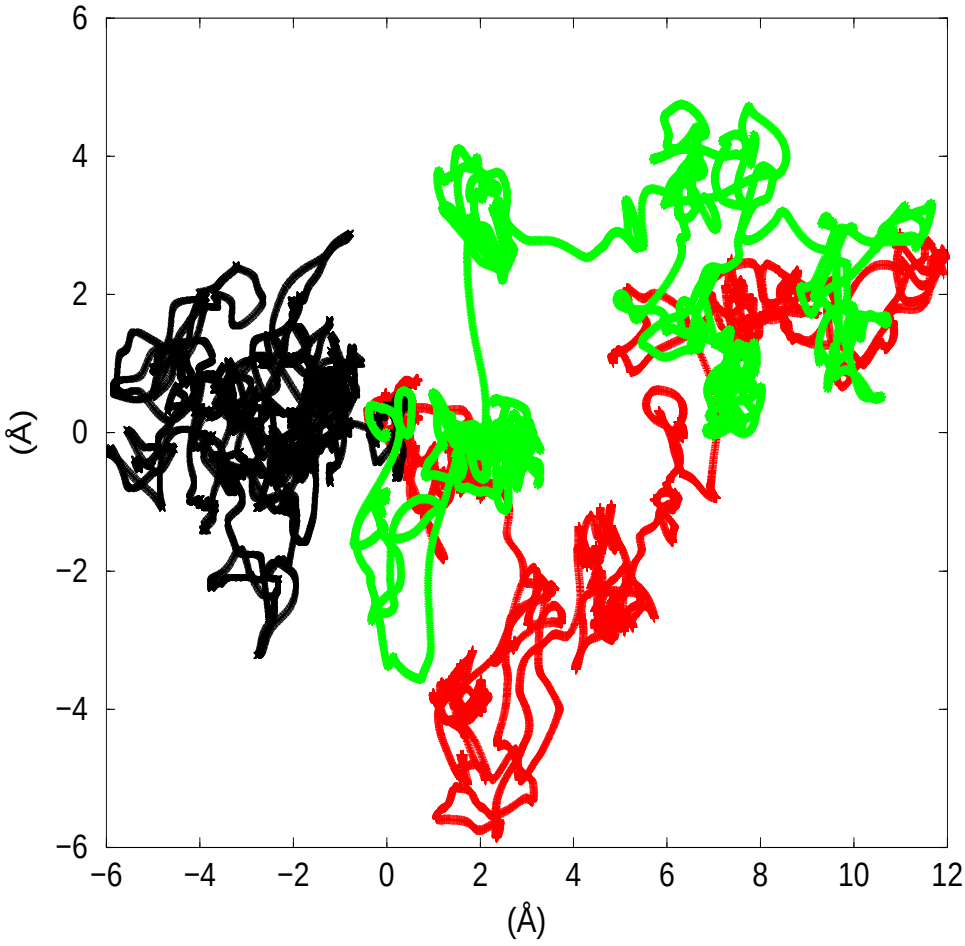

Figure 3.17: Trajectories of the most (green and red) and least (black) mobile Ag atoms in $(GeSe_3)_{0.85}Ag_{0.15}$ glasses (T=1000 K). The axes are labeled in angstroms.

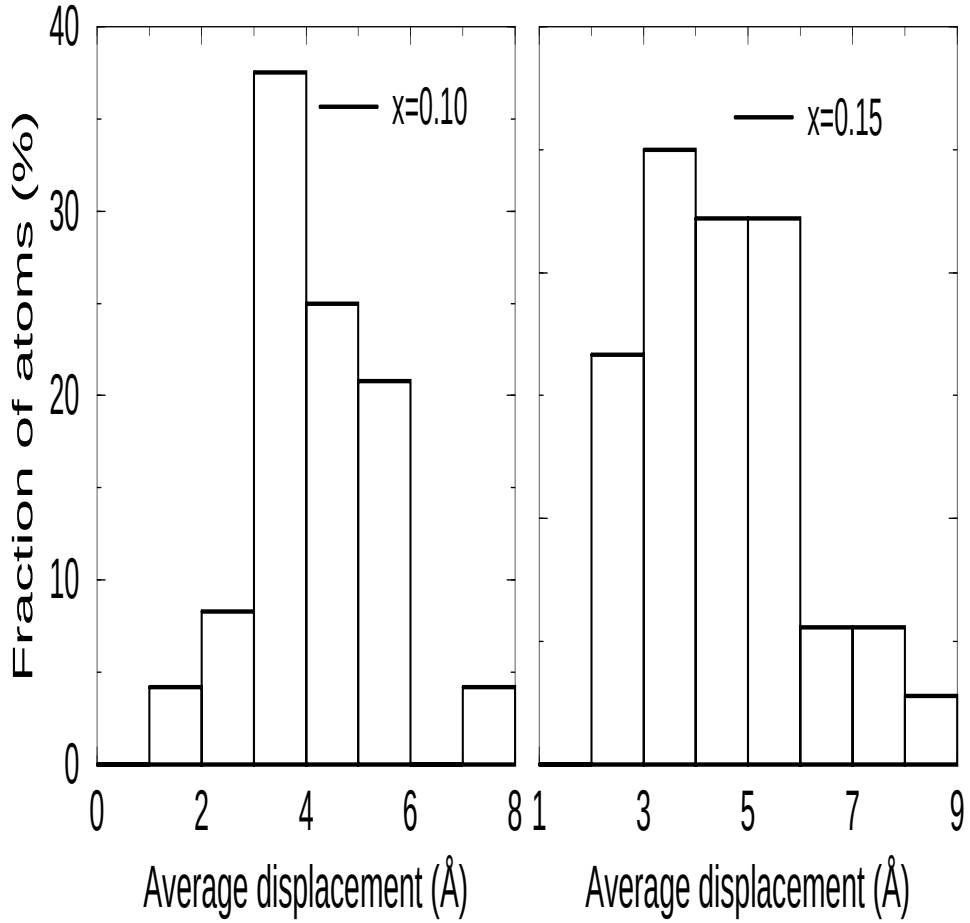

Figure 3.18: Histogram of RMS displacements of Ag ions in both models. Left panel, 10% Ag, right panel 15% Ag. 39ps of constant temperature MD at 1000K was used to accumulate these statistics.

Table 3.10: Estimates for the trap size r_{tr}, trap lifetime t_{tr}, and the self-diffusion coefficient D_{Ag} as a function of temperature T.

	T (K)	r_{tr} (Å)	t_{tr} (ps)	D_{Ag} (cm^2/s)
$x = 0.10$	640	0.81	5.89	-
	800	1.41	3.31	1.29×10^{-7}
	1000	1.78	2.73	1.59×10^{-5}
$x = 0.15$	640	0.94	5.58	1.52×10^{-6}
	700	1.34	4.67	1.82×10^{-6}
	800	1.40	3.80	6.50×10^{-6}
	1000	1.84	2.66	2.06×10^{-5}

D, and, in particular, estimates for the self-diffusion coefficient of Ag, D_{Ag}. The estimated values of D_{Ag} as a function of temperature are listed in Table 3.10. These results are qualitatively reasonable when compared to the recent (room temperature) experiments of Ureña *et al*[77] with the appropriate exponential activation factor included. The probability of correlated motion of Ag^+ will of course increase with increasing Ag concentration in agreement with decrease of the activation energy for conductivity.[78].

The dynamics is sensitive to the temperature. We performed additional simulations at temperatures ranging from 640K to 1000K. In Fig. 3.19 we illustrate the hopping, which is qualitatively like the high temperature hopping, and the traps are very well defined. We note that even the most mobile Ag ions spend a substantial time in the traps, and appear to hop very efficiently (quickly) between traps.

To further study the trapping centers[79] we also obtained estimates of trap sizes and trap lifetimes as a function of temperature. In our calculations, we consider only particles that experience more than one traps. To calculate the size of the traps we enclose the particle trajectories of each trap in a sphere of radius r_{tr} centered on the average position of the particle in the trap. Then, we determine the displacement of the particle trajectories in the trap with respect to the average trajectory, and

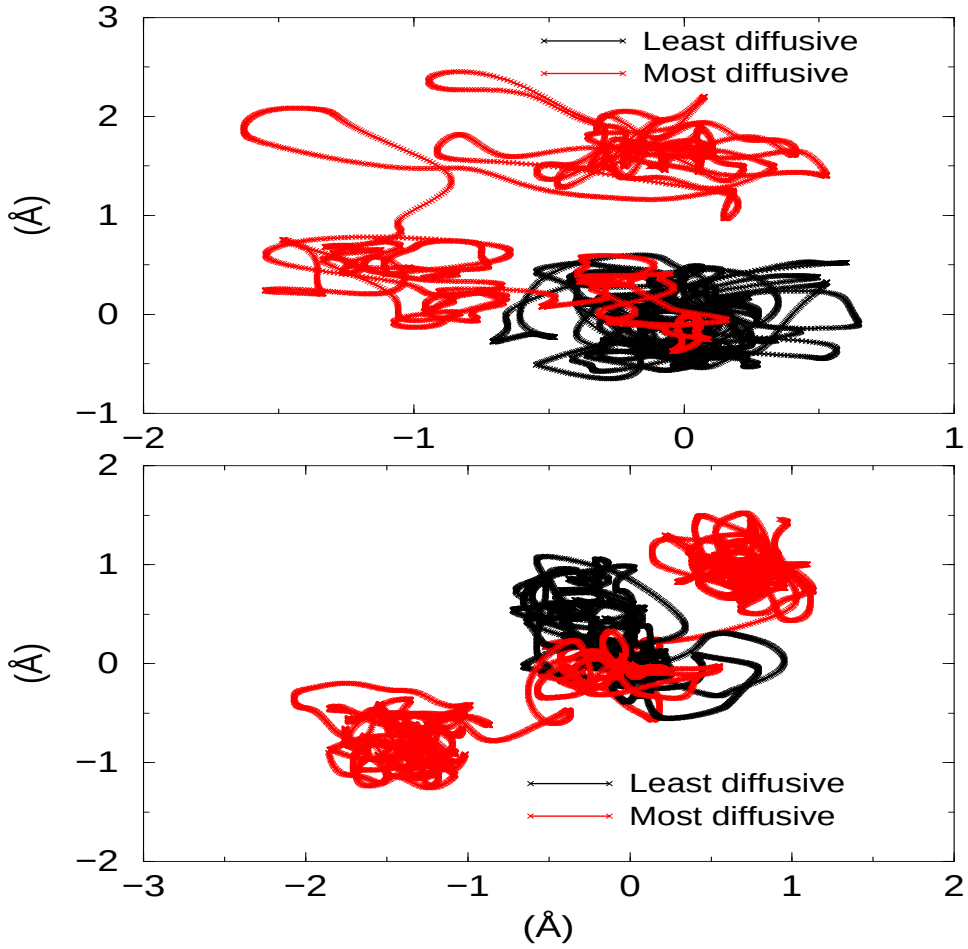

Figure 3.19: Trajectories of the most and least mobile Ag atoms in $(GeSe_3)_{0.90}Ag_{0.10}$ (top panel) and $(GeSe_3)_{0.85}Ag_{0.15}$ (bottom panel) glasses (T=640 K). The axes are labeled in angstroms.

average over all the displacements. The trap size r_{tr} is then obtained by averaging over different traps. Knowing the trap sizes, their lifetimes can be easily determined. In Table 3.10, we give an estimate of the trap sizes and trap lifetimes as a function of temperature. As T increases, the trap sizes increase and their lifetimes decrease. The averaged trap radii range from about 0.8 to more than 1.8 Å, and the averaged lifetimes extend from about 2.5 to more than 5 ps. The individual trap radii can be as large as 2.4 Å and the lifetimes as long as 7 ps. We have also used the MSD method[80] to estimate trap sizes, and obtain results within a factor of ~ 2 from our simple geometrical approach.

Further insight into the mechanism of diffusion in $(Ge_xSe_{1-x})_{1-y}Ag_y$ can be found by studying the behavior of the molar volume of particular regions containing silver atoms. Hence we calculate the local density of the most and least mobile silver atoms as a function of time, then compare them to the density of the glass. To do so, we draw a sphere of radius R=4 Å. The center of the sphere is the position of the Ag atoms we are tracking at a time t (the center of the sphere varies as a function of time). Then we calculate the mean density of atoms inside the sphere. Fig. 3.20 illustrates the local density of a few Ag atoms as a function of time. As seen on the figure, the more mobile Ag atoms are consistently located in regions with a lower local density (lower local volume fraction) and higher disorder. This argues in part for a free volume picture, but it is also clear that the Ag ions "seek out" the lower density volumes[81], as one can see especially in the top panel of Fig. 3.20. On the other hand, as we showed by direct calculation, there is little if any correlation between the trajectory-averaged mean density and the tendency to diffuse for the Ag atoms. On the other hand, perhaps unsurprisingly, we found also explored correlations between the average displacement of mobile Ag ions and the standard deviation of their local density ($\sigma_i = \sqrt{\langle \rho_i^2 \rangle - \langle \rho_i \rangle^2}$, where ρ_i is the local density of the Ag ion i, and $\langle\rangle$ means trajectory average). We found that as the average displacement increases, the standard deviation becomes larger (see Fig. 3.21). The correlations are perhaps linear with much noise. This implies that the diffusive Ag ions are exploring a wide variety of densities and the weakly-diffusing Ag sample a restricted density range.

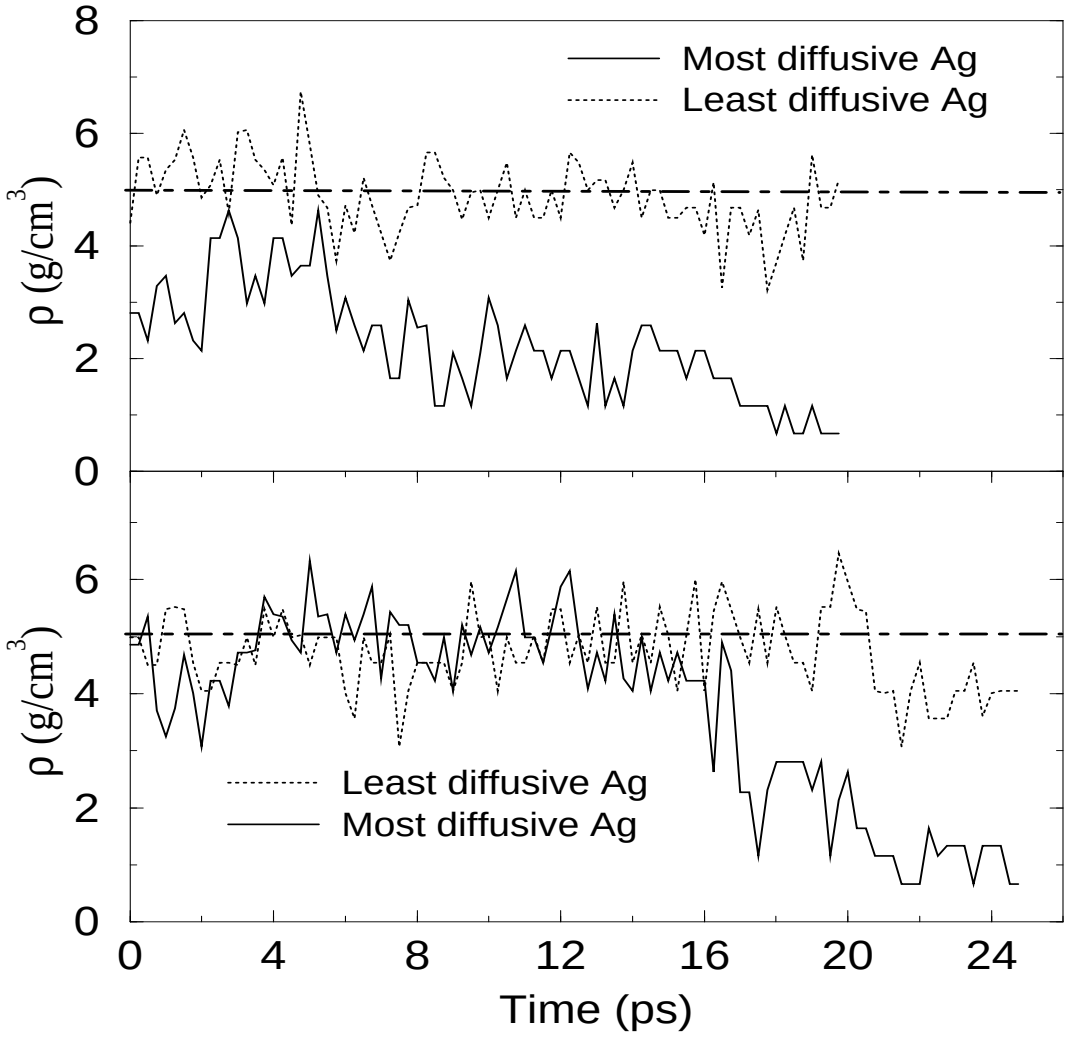

Figure 3.20: Local density of the most and least mobile Ag atoms as a function of time in $(GeSe_3)_{0.90}Ag_{0.10}$ (top panel) and $(GeSe_3)_{0.85}Ag_{0.15}$ (bottom panel) glasses.

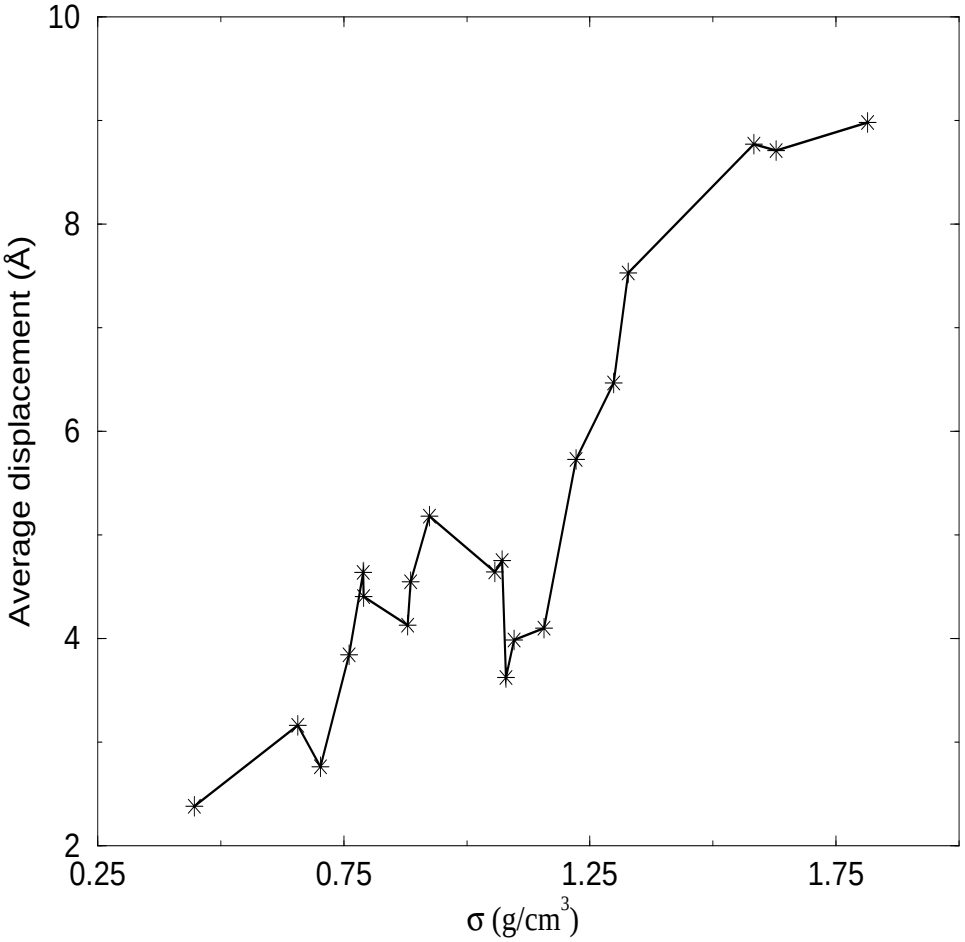

Figure 3.21: Average displacement of the mobile Ag ions as a function of standard deviation of the local density in $(GeSe_3)_{0.90}Ag_{0.10}$ and $(GeSe_3)_{0.85}Ag_{0.15}$ glasses. The figure suggests that the more mobile Ag ions sample a wider range of local densities (see text).

We have presented *ab initio* models of GeSe glasses heavily doped with Ag and studied the dynamics of the network with an emphasis on the motion of Ag ions. The models reproduce structural data, including reasonably subtle features in the diffraction data including the first peak (or shoulder) in S(Q). Wavelet method helps significantly in revealing intermediate range real-space correlations in the glasses. The atomistic motion of Ag^+ ions is detailed for short times with a reliable first principles interaction. We have shown by direct calculation that trapping centers exist, and have shown that local basis *ab initio* MD can provide direct insight into the processes of transition metal dynamics in amorphous chalcogenide materials.

Chapter 4

New Modeling Schemes for Binary IV-VI Glasses

The modeling of complex materials based upon molecular dynamics simulation has been one of the remarkable recent advances in theoretical condensed matter physics. Whether the potentials chosen are empirical or *ab initio*, remarkable insights have accrued for diverse problems in materials physics and beyond. There is however an unsatisfying point to the logic of MD simulation: it does not make use of all the information available about a material under study – notably the information implied by experiments. Simulations often cannot achieve agreement with experiment because of short simulation times, small system sizes or inaccuracies in the interactions. Successful prediction of *new* properties is more likely for models in agreement with existing data. Imposition of experimental information may be important in phase-separated or other complex materials for which obtaining a suitable starting structure may be difficult.

To produce realistic models, Nakhmanson, Zhang, and Drabold [82] have found it useful to include primitive *a priori* information about the chemical order and coordination in model construction because of the limitations of molecular dynamics (MD) simulation time scales. For Ge_xSe_{1-x}, the limitation of the quench from the melt method appears to be an incorrect static structure factor S(Q), for large Q. To overcome the sampling limitations of MD, we have recently developed new schemes

that emphasize the importance of correct topology of starting structure for successful modeling. Among them, the "decorate and relax" (DR) [83] approach is a perfect candidate for modeling binary glasses beginning with models of tetrahedral amorphous semiconductors. This approach is extremely simple and faster than traditional quench from the melt simulations. The other approach is the "experimentally constrained molecular relaxation" (ECMR) [68] that merges the power of *ab initio* molecular simulation with the hybrid reverse Monte Carlo method. We also developed the idea of inferring complex "building blocks" [84, 85] analogous to what is present in the stoichiometric glasses to model $GeSe_{1.5}$. We have made a comparison of such models to those obtained from quench from the melt process. Good agreement with the existing experimental data was obtained especially for large Q behavior of S(Q)[83]. For large Q, S(Q) for quench from the melt models decays away too rapidly relative to experiment [86]. These methods are general and can be extended to other complex materials.

4.1 Decorate and Relax

We made models of $GeSe_2$, $SiSe_2$ and SiO_2 glasses by starting with a defect-free (fourfold coordinated) 64 atom supercell model of a-Ge made with the WWW method [11, 87]. Characteristic of an amorphous column IV material, this model has bond angles tightly centered on the tetrahedral angle, and has a topology presumably unrelated to g-$GeSe_2$, g-$SiSe_2$ and g-SiO_2. We decorated all the IV-IV bonds with a bond-center VI, and rescaled the coordinates to the experimental density of g-$GeSe_2$, g-$SiSe_2$ and g-SiO_2 respectively. The 192 atom models of g-$GeSe_2$ and g-$SiSe_2$ were then quenched with FIREBALL to the nearest minimum. The 192 atom model of g-SiO_2 was relaxed with SIESTA. We name this scheme "decorate and relax". The resulting models are in some ways superior to the best models in existence, are remarkably easy to generate, and preliminary work with Chubynsky and Thorpe suggests that the approach may be extended to off-stoichiometry compositions. Such networks have been introduced and explored by Chubynsky and Thorpe[88] to study the vibrational excitations of chemically ordered networks. Vink and Barkema have

also explored some related methods in silica[89]. We then extended the calculations to decorated models with 648 atoms (starting with 216 atom WWW cells).
We employed SIESTA for silica because of concerns about the extreme ionicity of the material, and also to easily check the importance of density functional, basis set and spin polarization. In the end, we found that relatively simple approximations (self-consistent LDA and a single zeta basis) were adequate. Even using soft pseudopotentials, we found that a 150 Ry cutoff was needed for evaluation of the multicenter matrix elements.

4.1.1 $GeSe_2$ glass

The decorated models have general similarities and origins that we illustrate with the case of $GeSe_2$. In Fig. 4.1 we report the static structure factor for the unrelaxed decorated diamond (simply Ge on a diamond lattice with bond center Se added, without relaxation and rescaled to the experimental density of glassy $GeSe_2$) and WWW *a*-Ge similarly decorated and rescaled. In both models we note the presence of a strong, sharp prepeak in S(Q). In the crystalline decorated diamond model, the so-called first sharp diffraction peak (FSDP) arises from the $\langle 111 \rangle$ Bragg peak of the structure. This prepeak is very similar to the prominent FSDP feature of glasses. The existence of this peak in both models shows that our starting models already exhibit the intermediate range order associated with the FSDP. Relaxation tunes the topology of the models in order to give the topology and chemistry suited to the particular glass. Other interesting properties of our models are that all have large state-free gaps and good vibrational density of states. The relaxation is substantial enough to create small amounts of chemical disorder and both edge and corner sharing tetrahedra in $GeSe_2$ and $SiSe_2$.

The structure of these models are analyzed by computing the partial Faber-Ziman structure factors. In preliminary work, we compared the results for the Faber-Ziman structure factors S(q) vs experiment [90, 91], the earlier model of g-$GeSe_2$ [92, 93] and the new model (Fig. 4.2). The decorated model is at least as good as the previous model and comparable to the models of Massobrio and co-workers [31]. While the new model has strong similarities manifested in the partial structure factors, and

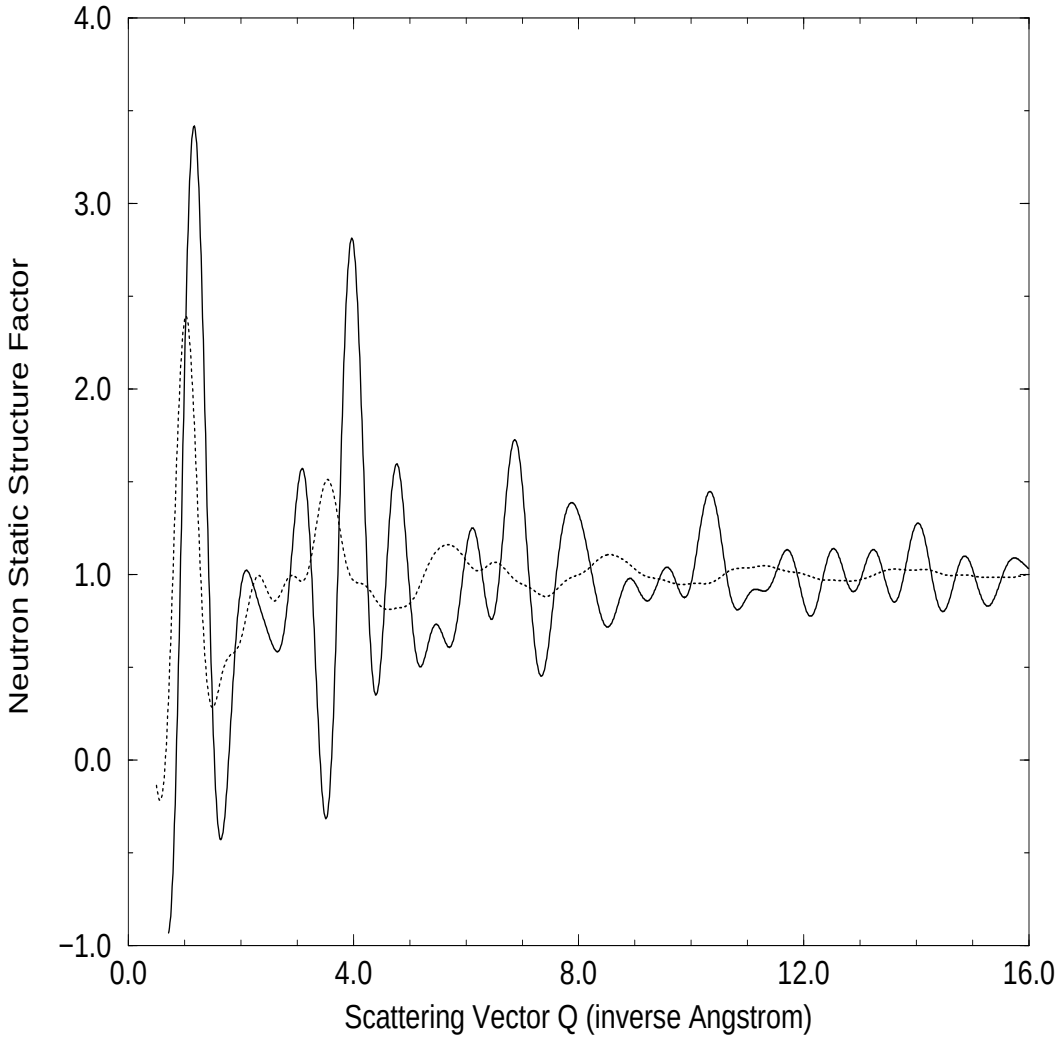

Figure 4.1: Calculated total neutron structure factor S(Q) of unrelaxed "decorated" glassy $GeSe_2$ (dotted line) and unrelaxed "decorated" crystal $GeSe_2$ (solid line).

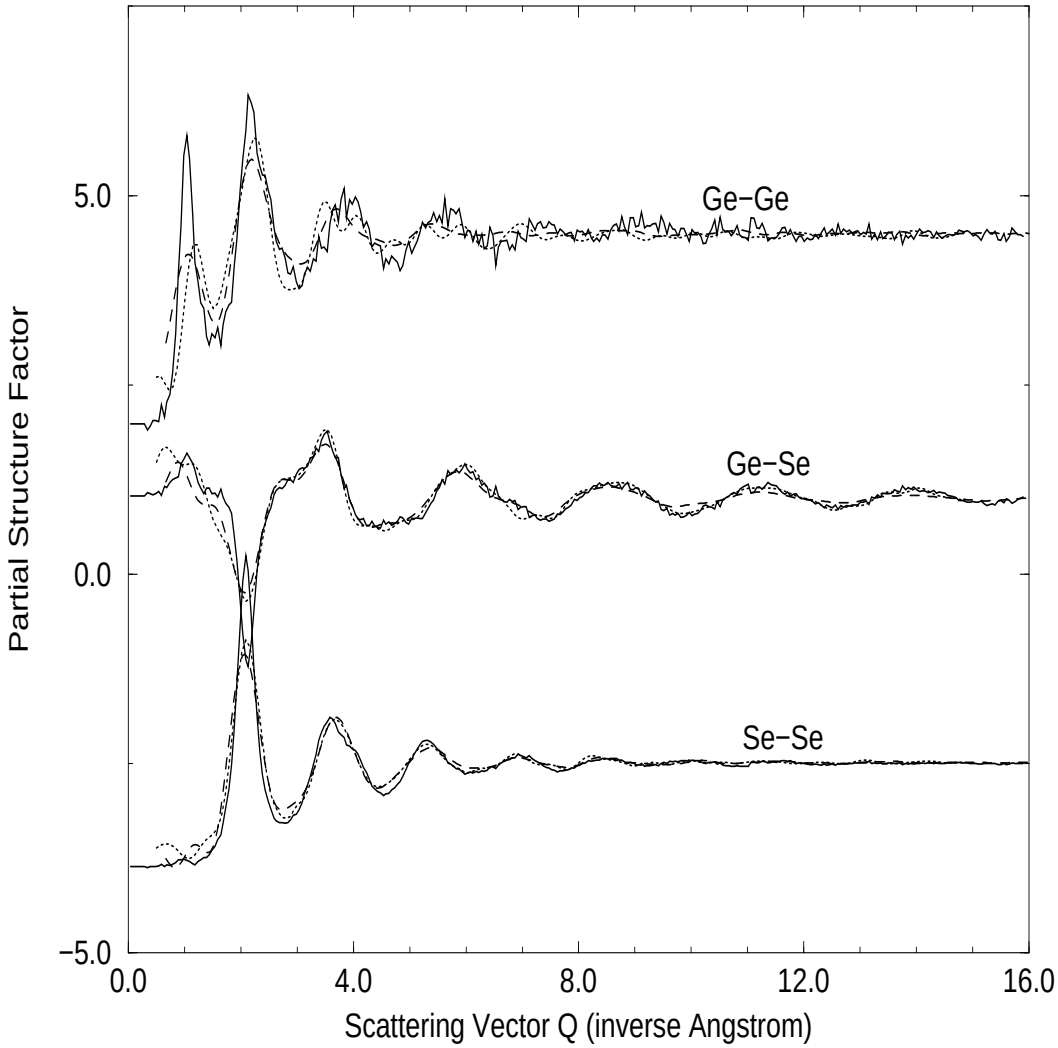

Figure 4.2: Partial structure factors S(Q)for glassy GeSe2. The solid curves are from experiment(see [90]), the dashed curves are from the "cook and quench" model (see [92, 93]), and the fine dotted curves are from the decorated WWW model (see text). The units of the scattering vector Q are Å^{-1}.

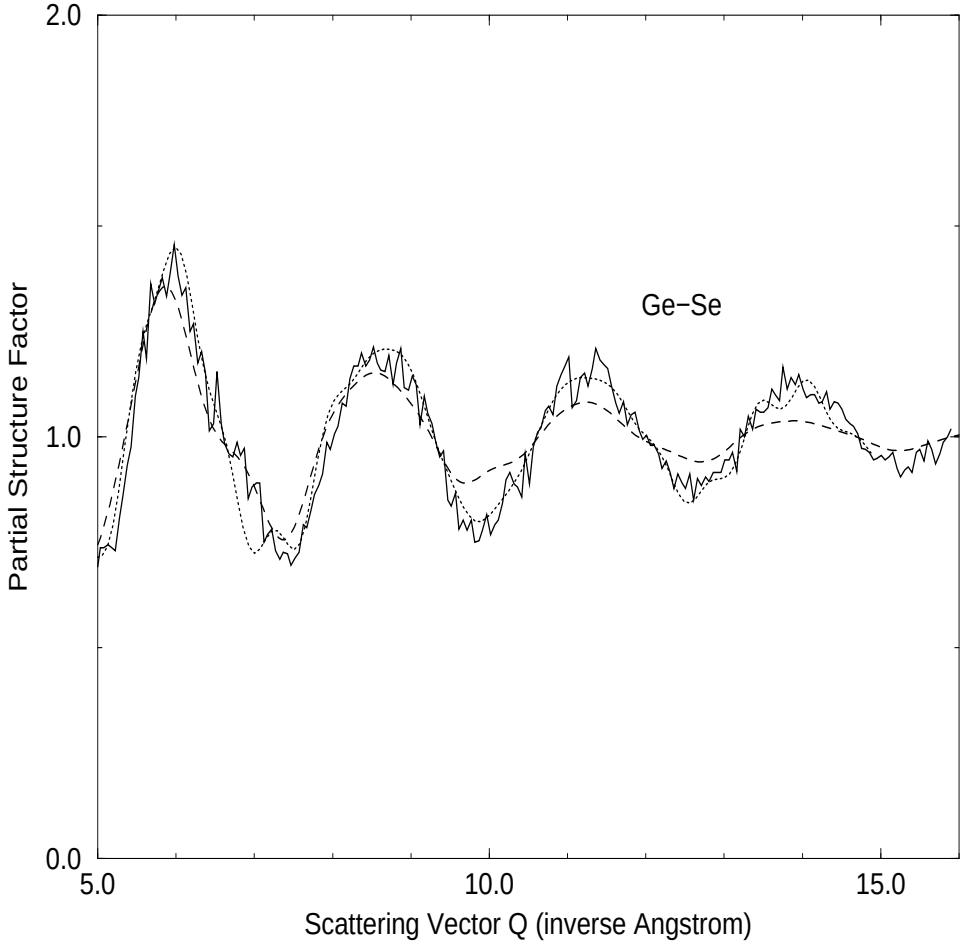

Figure 4.3: A blow up of the Ge-Se partial structure factor for glassy $GeSe_2$. Note the rapid decay of S(Q) for the quenched model (see [92, 93]) and improved agreement with experiment (see [90])for the decorated WWW model. The curve styles are as in Fig. 4.2.

Table 4.1: The positions of the A_1, A_2, A_3 and B peaks in the EDOS of our "decorated" model of g-$GeSe_2$ compared to experimental [41] and "cook and quench" [93] results.

(eV)	A_1	A_2	A_3	B
Decorate	-1.36	-2.8	-4.5	-7.2
Experiment	-1.38	-3.0	-4.6	-7.8
Cook and quench	-1.4	-2.7	-4.6	-7.0

essentially similar topological/chemical ordering to the quench from the melt model, a key difference of the "decorated" model is the persistence of correlations in S(Q) beyond 10 $Å^{-1}$ in unique and pleasing agreement with experiment, whereas the earlier model displays a more rapid decaying amplitude for large Q (see Fig. 4.3). Our interpretation of this is that the quench from the melt model was too "liquid like" - precisely the kind of artifact one might expect from rapidly quenching a liquid on the computer. The new model has 86% heteropolar bonds, with the homopolar bonds Se-Se (13.5%), except for a single bond (0.5%). Ge was 78% fourfold, 19% threefold and 3% twofold, numbers quite consistent with the earlier model. We also computed the vibrational and electronic states densities (EDOS) and found them to be very similar to the earlier model of Cobb[93]. The peaks in the EDOS are discussed in Table 4.1 and plotted in Fig. 4.4.

4.1.2 $SiSe_2$ glass

We extended the method to g-$SiSe_2$. In Fig. 4.5 we display the calculated total neutron structure factor of our 648-atom model of g-$SiSe_2$ along with the experimental [94] total neutron structure factor and the 192-atom model from decorate and relax [83]. The agreement is good over the entire Q range, the positions of maxima and minima being properly reproduced (though the amplitudes are not perfect). Our calculated partial structure factors show an FSDP at 1.0 $Å^{-1}$ in $S_{Si-Si}(Q)$ and $S_{Si-Se}(Q)$, and at 1.1 $Å^{-1}$ in $S_{Se-Se}(Q)$. The largest value of the first sharp diffraction

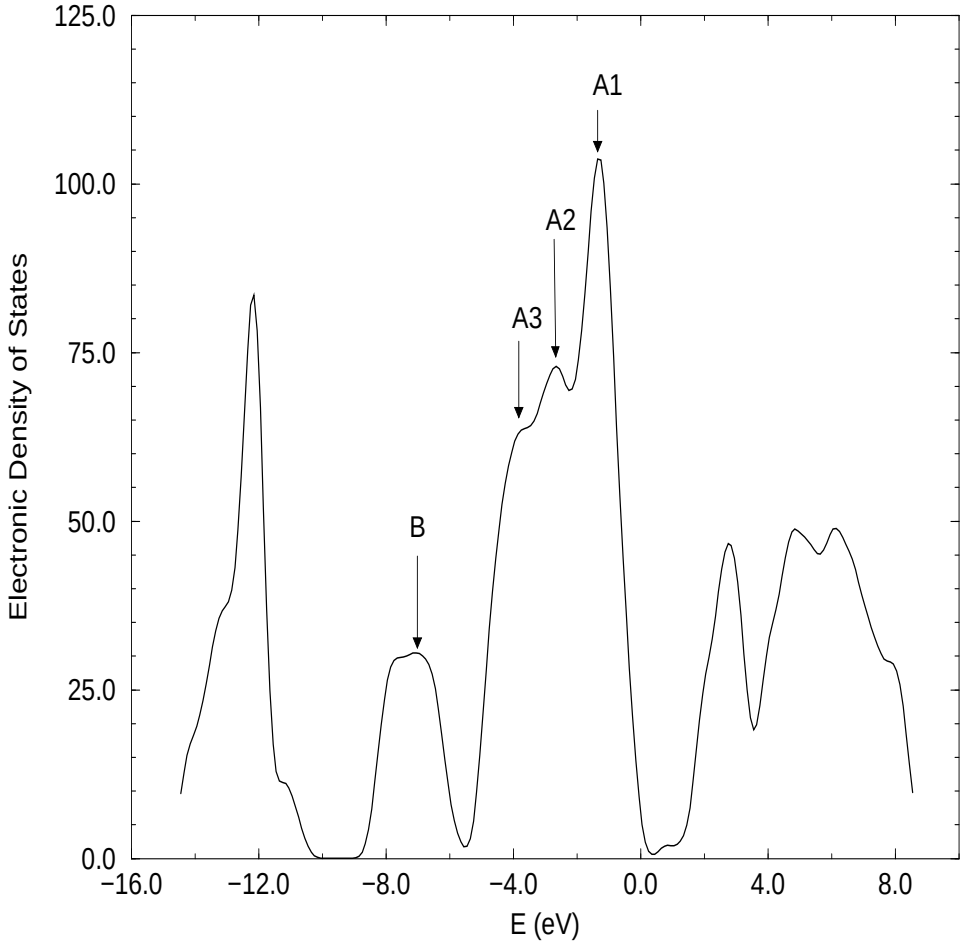

Figure 4.4: Electronic density of states for g-$GeSe_2$.

peak is observed in $S_{Si-Si}(Q)$ which is primarily responsible for its appearance in the total neutron structure factor. In Celino and Massobrio's calculations [95] the FSDP was absent in the calculated Se-Se partial structure factor. To our knowledge, no experimental partial structure factors are currently available.

The MD partial pair correlation functions $g_{\alpha\beta}(r)$ for the 648-atom model are not so different from the 192-atom model [83] except for the appearance of a peak at around 3 Å in $g_{Si-Si}(r)$ (see Fig. 4.6). This peak is entirely due to correlations arising from ES tetrahedra. The atomic structure of our model consists of both corner-sharing and edge-sharing $SiSe_4$ tetrahedra. The percentage of Si atoms forming homopolar bonds are less than 0.1 %. On the other hand 6 % of Se atoms are involved in homopolar bonding. Considering only the chemically ordered $SiSe_4$ and $SiSe_2$, about 80 % of Si and 83.3 % of Se atoms are respectively fourfold and twofold. Neutron diffraction and EXAFS experiments have suggested that the network of tetrahedra is mostly chemically ordered, but a small amount of homopolar bonds should not be ruled out [96].

Few MD studies have determined ring statistics in amorphous $SiSe_2$ [97, 98]. Analysis of ring distributions (see Table 4.2) reveals that threefold, fourfold, and eight-fold are most abundant. In their calculations, Antonio *et al* [98] found that threefold and eight-fold rings were the most abundant, and chain-like fragments were revealed predominantly in eight-fold rings. The appearance of odd number rings is due to homopolar bonds. There is also a significant amount of six-fold rings which together with the fourfold units are responsible for the chemical order in the glass.

In Fig. 4.7 we display the VDOS along with the principal peak positions in glassy $SiSe_2$. The general shape of the density of states agrees well with the inelastic neutron scattering measurements made on the high-resolution medium-energy chopper spectrometer (HRMECS) [99]. In the HRMECS experiment, the acoustic band reveals considerable structure, with three peaks, approximately centered at 48, 81,and 113 cm^{-1}. In our theoretical calculation, these peaks are respectively found at 47.5, 70, and 112 cm^{-1}; numbers quite consistent with inelastic neutron scattering experiment and Raman measurements [96, 38, 100, 101]. In the intermediate band two peaks appear at 215 and 240 cm^{-1}. On Raman measurements the 48 cm^{-1} peak is unresolved.

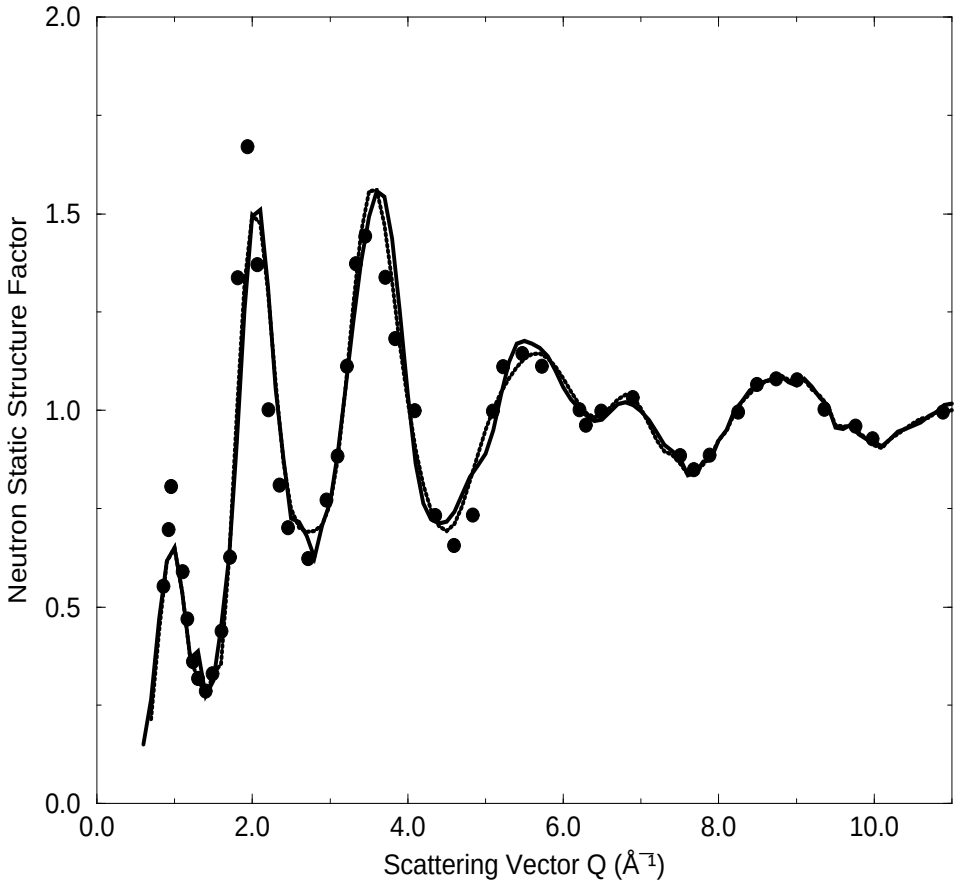

Figure 4.5: Calculated total neutron static structure factor S(Q) of glassy $SiSe_2$ (dotted lines are for 192-atom model and solid lines are for 648-atom model) compared to experimental data [94] (filled circles).

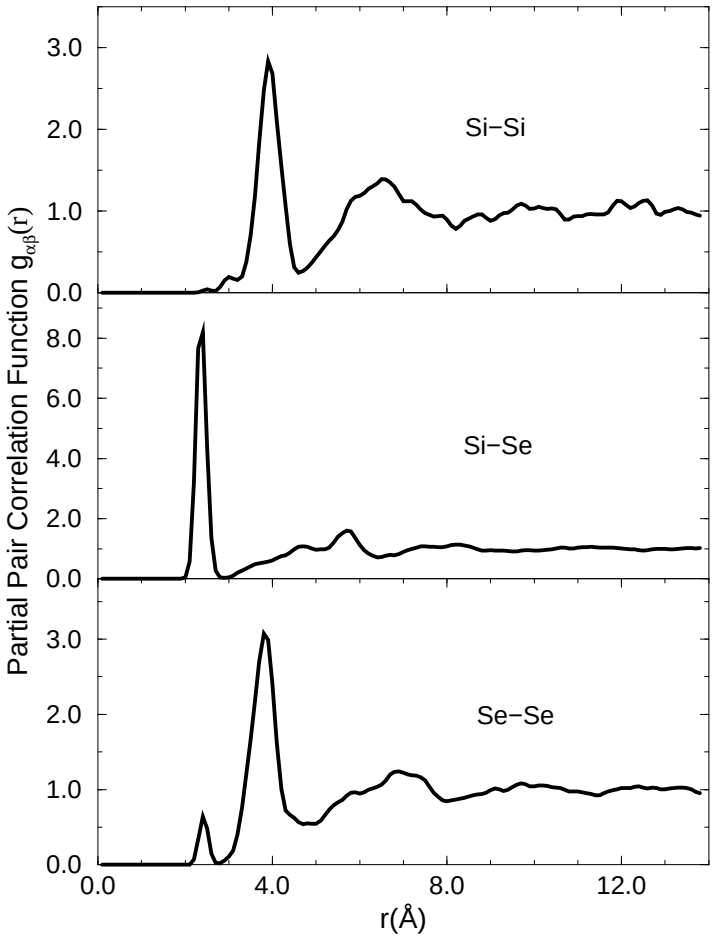

Figure 4.6: The calculated real space partial pair correlation function $g_{\alpha_\beta}(r)$ of g-$SiSe_2$.

Table 4.2: Ring statistics in $SiSe_2$ and SiO_2 glasses. The number of n-membered rings, n=3 through n=9.

Ring size	3	4	5	6	7	8	9
SiO_2	0	7	0	6	0	15	0
$SiSe_2$	15	14	4	11	5	12	9

Based on Raman measurements, Susman *et al* [96] associated the 70 cm^{-1} peak with the edge-sharing tetrahedra while Griffiths *et al* [100] associated it to an A_g mode. More peaks are observed in the spectrum of the VDOS of g-$SiSe_2$. In our model these peaks occur around 215, 240, 303, 358, 387 and 469 cm^{-1}. Sugai [38] assigned the 213 and 222 cm^{-1} Raman peaks to the A_1 (corner sharing) and the 240 and 248 cm^{-1} (not present in our model) to the ES modes. Jackson and Grossman [102] confirmed this result by assigning the 214 cm^{-1} peak to A_1 modes of CS-connected tetrahedra, either isolated or in chains.

The calculated EDOS and the species projected density of states are reported in Fig. 4.8. The valence band of the EDOS consists of two main bands. The upper band is from 0 to about -5 eV below the highest occupied molecular orbital (HOMO). For instance the Γ point optical gap of our model is of the order of 1.7 eV. As usual in local density approximation (LDA) calculations, the experimental gap is substantially underestimated. To our knowledge, experimental information about the EDOS is unavailable for g-$SiSe_2$, so the curve in Fig. 4.8 is actually a *prediction*. The states can be classified in the following way: the states at about -14 eV are Se s states; the states from -8.3 eV to -3.3 eV are bonding states between Si sp^3 hybrids and Se p nonbonding orbitals. There is a distinctive peak deriving mainly from Se atoms. The leading peak is attributed to the lone-pair band of Se [42], which is similar to topmost valence band of Se [103]. By analogy to $GeSe_2$, four peaks can be identified as A_1, A_2, A_3, and B peaks respectively. Their values are listed on Table 4.3.

In Fig. 4.9 we plot the localization of electronic eigenstates for g-$SiSe_2$ in the band gap region. We also plot some of the characteristic defect types causing localization of electronic eigenstates in the band gap region. Eigenstates in the region [-6, -5.3]

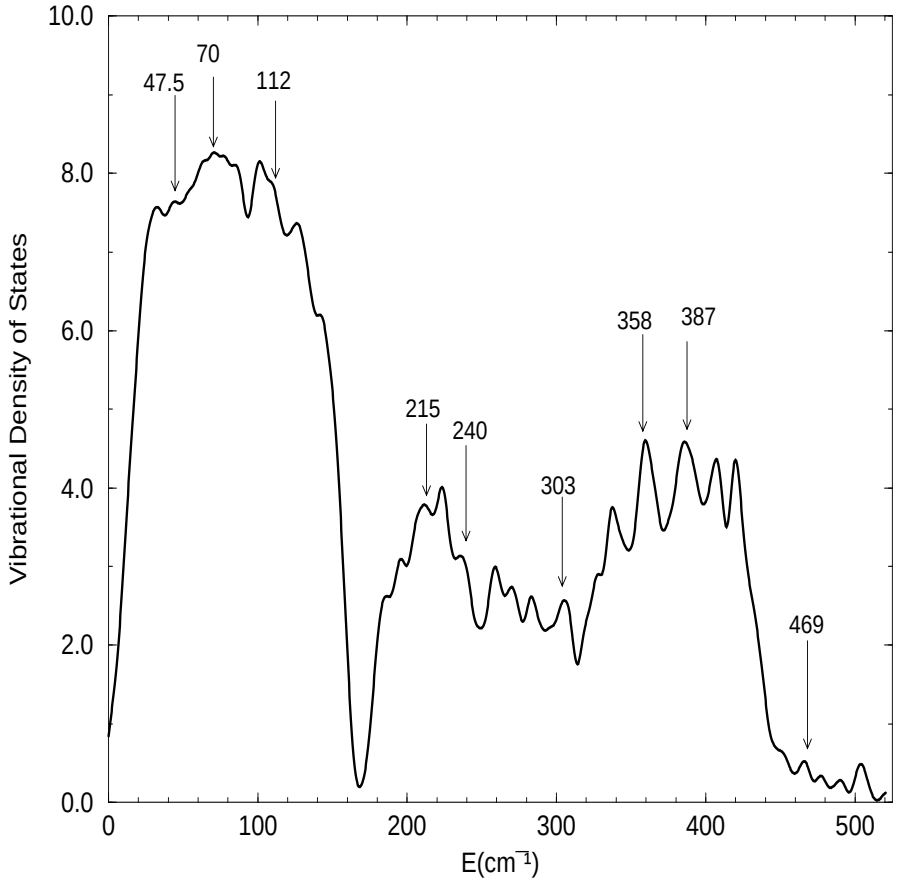

Figure 4.7: Calculated vibrational density of states of g-$SiSe_2$. Principal peaks positions are shown.

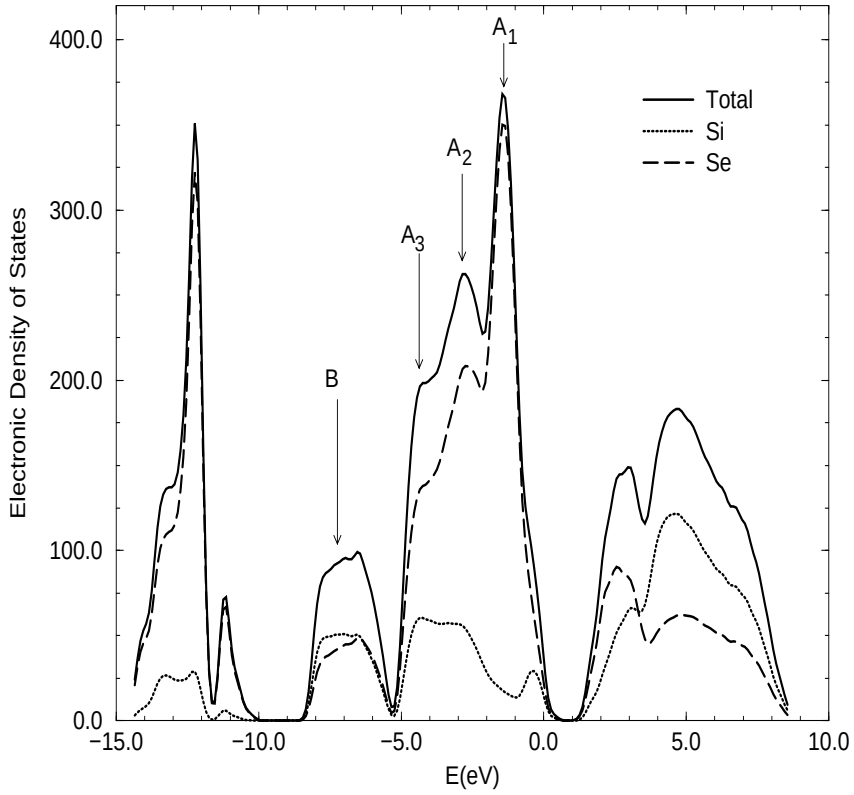

Figure 4.8: Predicted electronic density of states (solid lines) and species projected electronic density of states for Se (dashed lines) and Si (dotted lines) for g-$SiSe_2$. The Fermi level is at E=0.

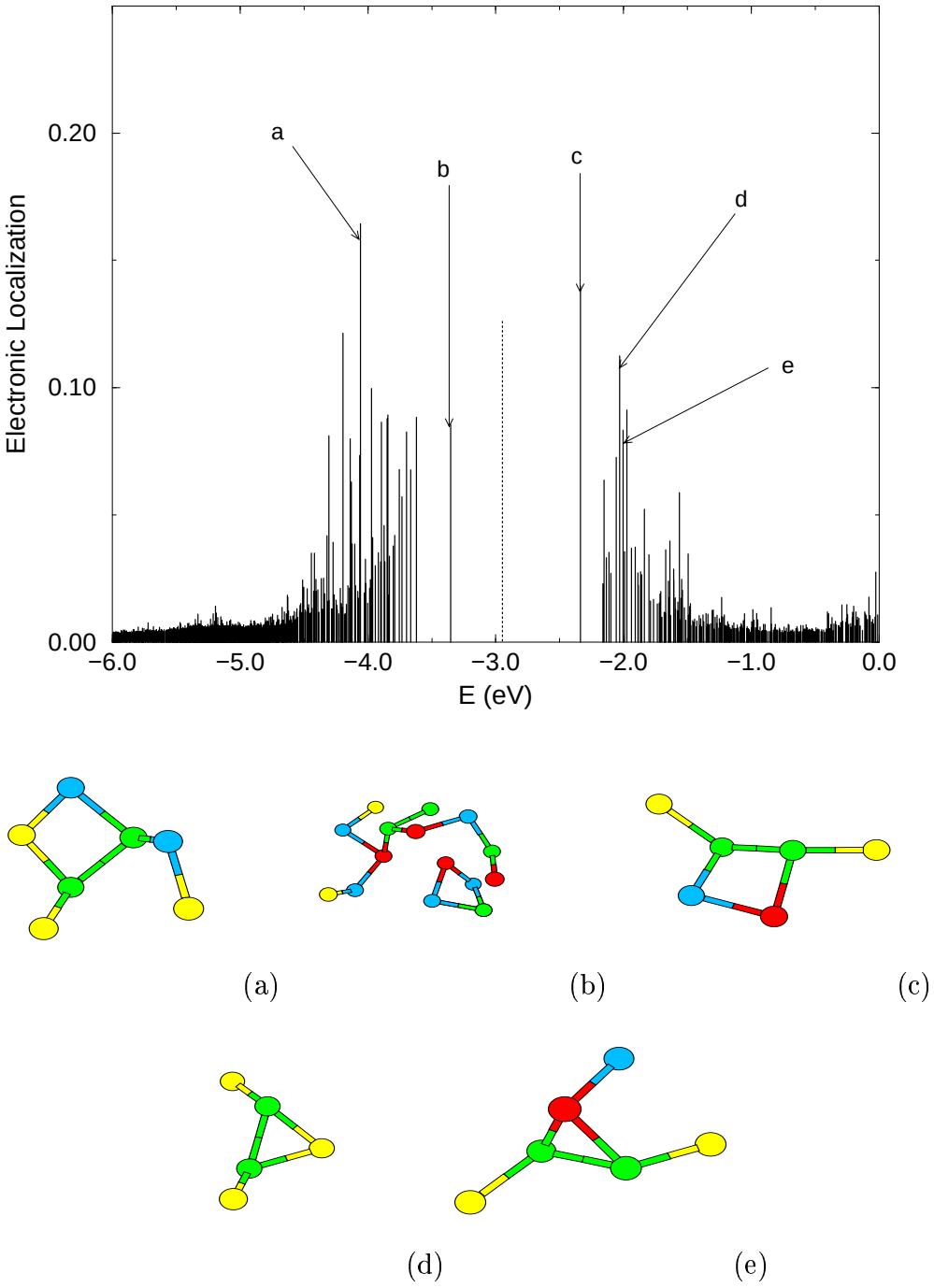

Figure 4.9: Inverse participation ratio along with the characteristic defect types causing localization of electronic eigenstates in the band gap region of g-$SiSe_2$. The vertical dotted lines indicates the position of the Fermi level. The color codes are defined as threefold Si atoms (red), fourfold Si atoms (yellow), threefold Se atoms (green), and twofold Se atoms (blue).

Table 4.3: The positions of the A_1, A_2, A_3 and B peaks in the EDOS of $GeSe_4$ and $SiSe_2$ glasses compared to experimental results of $GeSe_2$ [41].

(eV)	A_1	A_2	A_3	B
Experiment $GeSe_2$	-1.38	-3.0	-4.6	-7.8
Decorate $SiSe_2$	-1.4	-2.86	-4.4	-7.3

eV of the valence band are quite extended, but as one approaches the valence band edge the eigenstates become increasingly localized. At the conduction band edge the states are also localized. As one moves away from the conduction band edge the states become less and less localized. By examining the localized states at the band edges we found that the localized states mostly derive from under-coordinated (threefold) Si atoms and over-coordinated threefold Se atoms involved with Se-Se homopolar bonds. The localized states at the conduction band edge are mostly due to over-coordinated (threefold) Se atoms involved with homopolar bond. The Se and Si IPR's reveal that the localization is more pronounced on Se atoms than on Si. We can conclude that Se-Se wrong bonds cause more localized states than the geometrical defectives structures.

4.1.3 Amorphous silica, SiO_2

Structural properties

In Fig. 4.10. we compare the structure factor S(Q) of our 648-atom model of g-SiO_2 with the S(Q) of our 192-atom model [83] and the S(Q) extracted from neutron diffraction experiments [104]. There is nearly perfect agreement with experiment over the entire range of Q. The height and the position of the peaks coincide with the experimental results. The discrepancy between the 192 and the 648-atom models arises from finite size effects, since the same Hamiltonian and modeling procedure were used to generate both models. It is of some interest that the only substantial difference between the 192 and 648 atom models was near 2.0 $Å^{-1}$, at the minimum after the FSDP. The only notable remaining discrepancy between theory and experiment

Table 4.4: Location, and in parentheses the FWHM of the angles O-Si-O and Si-O-Si as determined from the simulation and experiments.

	Theory		Experiment	
	Decorate	Ref. [108]	Ref. [106]	Ref. [107]
OSiO	109.5° (9°)	108.3° (12.8°)	109.5°	109.7°
SiOSi	140° (25°)	152° (35.7°)	144° (38^o)	144°, 152°

appears near 12 Å^{-1}, and is similar to both models (and so is not due to a finite-size effect).

The origin of various peaks in S(Q) can be inferred from partial structure factors. The results for partial static structure factors are shown in Fig. 4.11. The second peak in S(Q) arises from Si-Si and O-O correlations with partial cancellation arising from Si-O anticorrelations. Since S(Q) is weighted by concentrations and scattering lengths, the O-O contributions in this region are comparable to those of Si-Si. The third, and fourth peaks receive contributions from Si-Si, O-O and Si-O correlations. The real space pair correlation functions of our vitreous silica models are illustrated in Fig. 4.12. The agreement between the experiment and theory is quite good. The peak position and the bond lengths are well reproduced and comparable to experimental values from neutron diffraction data. On average, miscoordinated atoms in our 648-atom model occurred with a probability of 2.16 %. These consisted of fivefold coordinated Si (3.2 % of Si) and of threefold coordinated O (1.6 % of O). Where chemical order is concerned, our model has 100 % heteropolar bonding as one would expect from the chemistry of silica. The resulting amorphous model is characterized by the presence of chemically ordered bond network in which Si-atom-centered tetrahedra are linked by CS O atoms.

For vitreous silica we also compute the bond angle distribution. Fig. 4.13 shows the distribution function for the tetrahedral angle O-Si-O and Si-O-Si. The O-Si-O angle has a mean value of 109.5° which is near the tetrahedral angle Θ_T=109.47°, and a full width at half maximum (FWHM) of the order of 9°. On the other hand the Si-O-Si angle-distribution is much broader with an average value of 140° with an

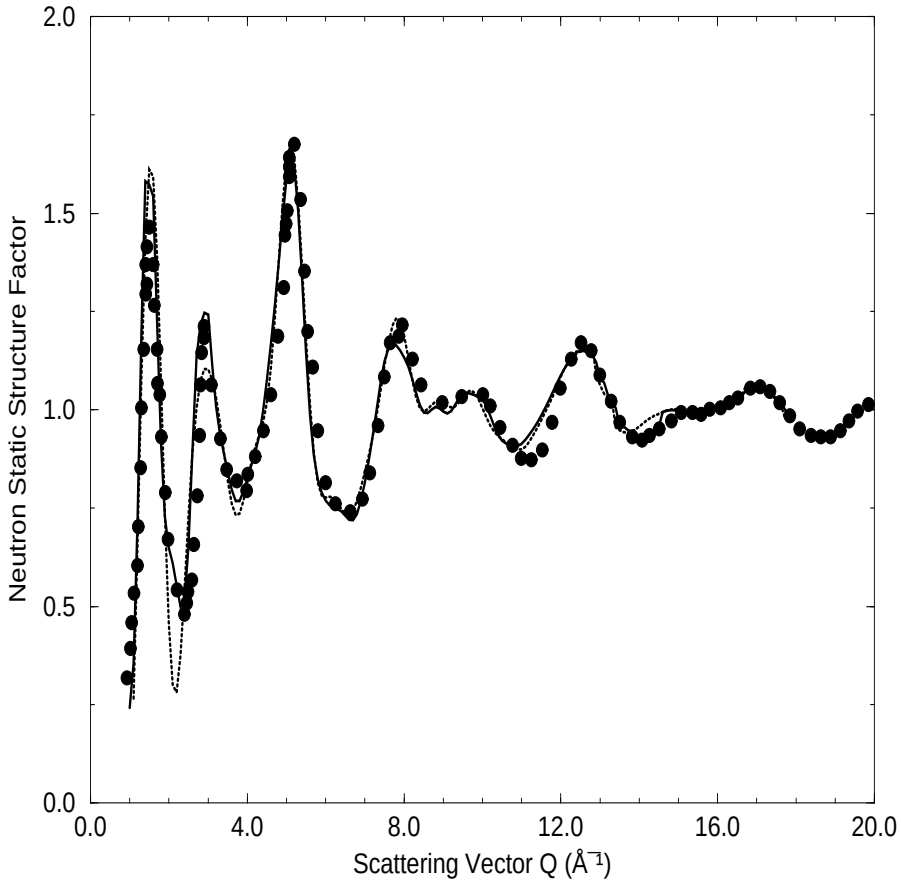

Figure 4.10: Calculated total neutron static structure factor S(Q) of glassy SiO_2 (dashed lines are for 192-atom model and solid lines are for 648-atom model) compared to experimental data [104] (filled circles). Note the close coincidence of the 648-atom model with the data.

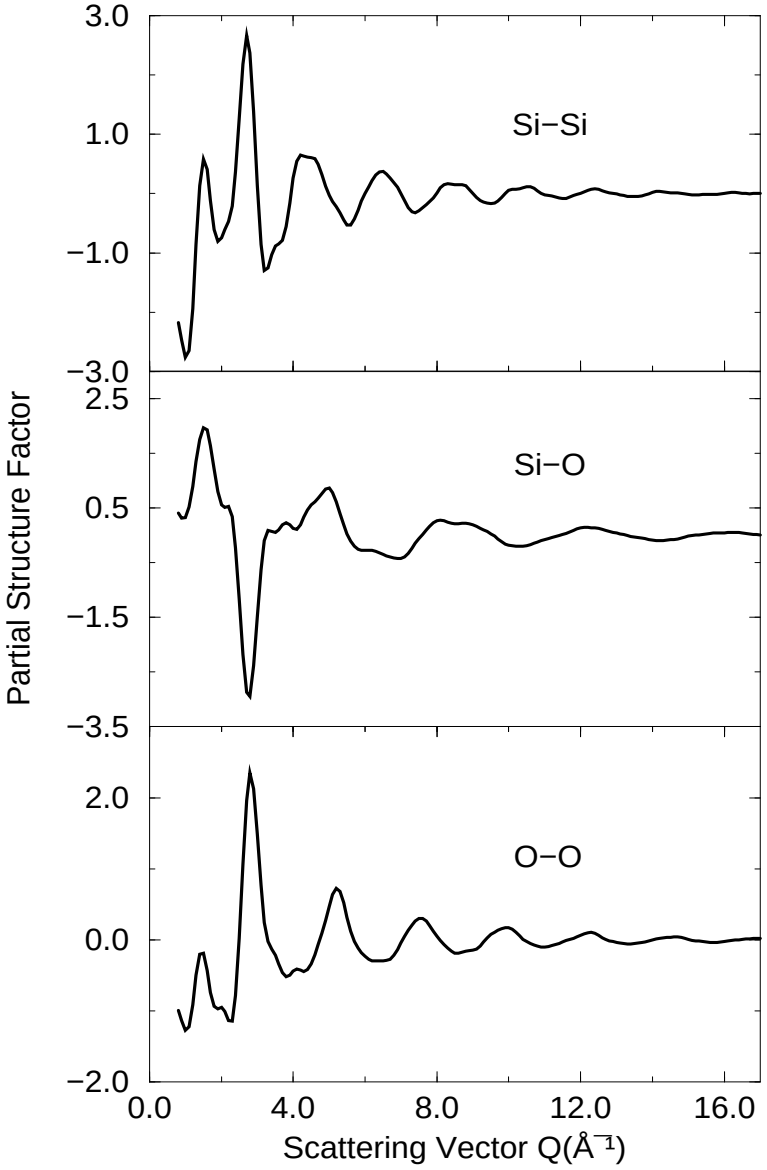

Figure 4.11: Calculated partial structure factors $S_{\alpha\beta}(Q)$ of glassy SiO_2.

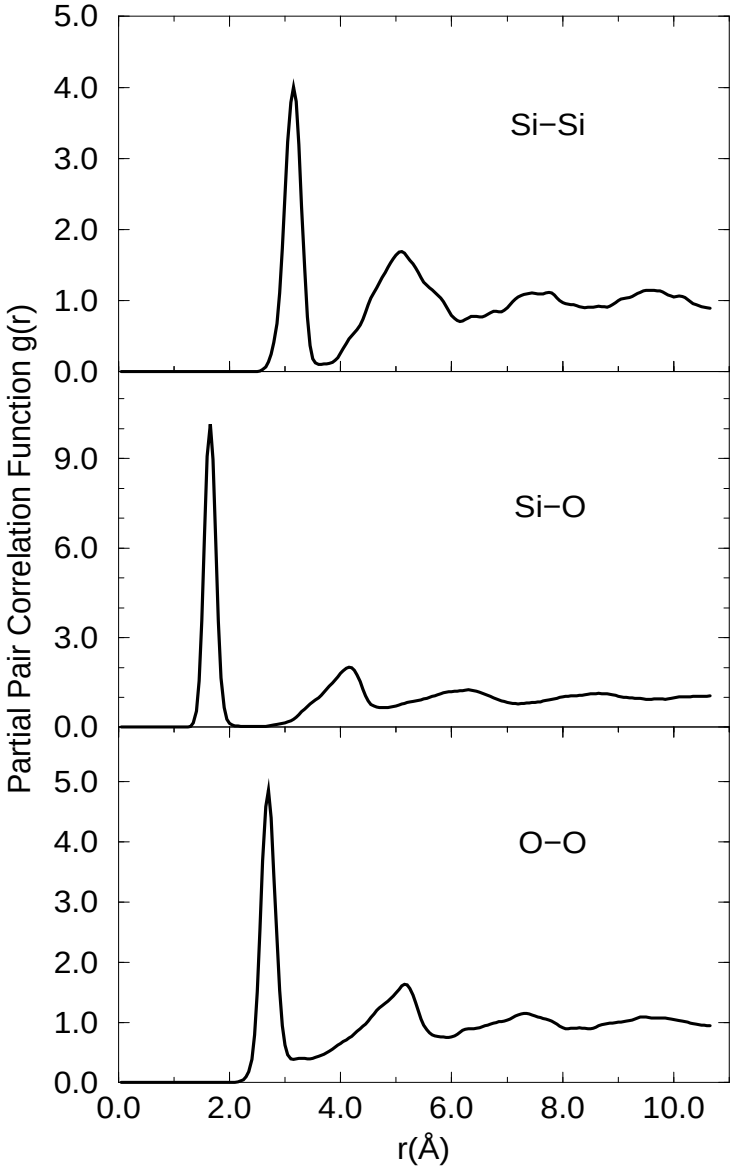

Figure 4.12: The calculated real space partial pair correlation function $g_{\alpha_\beta}(r)$ of g-SiO_2.

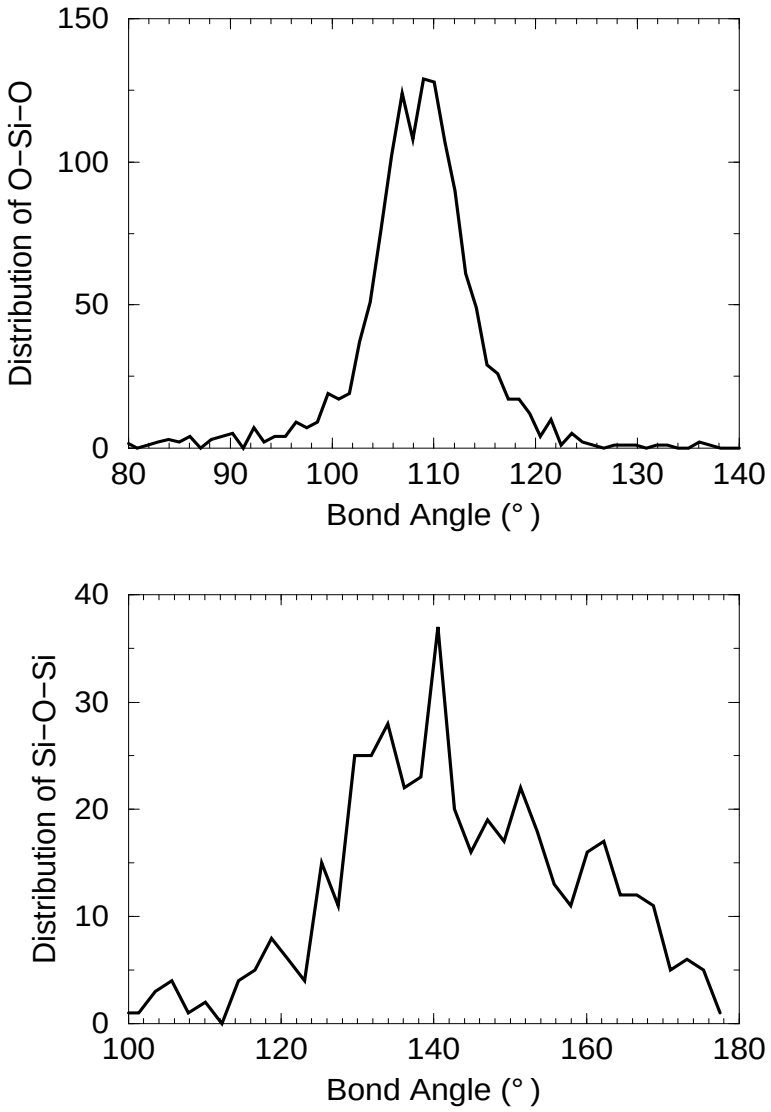

Figure 4.13: Bond-angle distribution function O-Si-O (top panel) and Si-O-Si (bottom panel).

FWHM close to 25°. In their experiment [105], Pettifer *et al* obtained an average value of 142° for the angle Si-O-Si with an FWHM of the order of 26°. In Table 4.4 we compare our results for the bond angle distribution with experiments [106, 107] and theoretical results [108]. The location and the width of the peaks are in good agreement with experimental values. The topology of our model is also examined through the ring structure. In Table 4.2 we report the distribution of the rings in our sample. We notice that there is no contribution from odd rings. This reiterates the absence of wrong bonds.

Vibrational properties

Amorphous silica has been extensively characterized via vibrational spectroscopies, including inelastic neutron scattering [109], infrared absorption [110], and Raman scattering experiments [111]. It was found that the spectrum shows several peaks. In order to show the validity of the vibrational features of our model, we report in Fig. 4.14 the VDOS for the 192-atom model of g-SiO_2 (the dynamical matrix for the 648 atom model has not yet been calculated) along with the neutron scattering experimental results of Carpenter *et al* [109]. Shapes and positions of the principal peaks are well reproduced with low-frequency bands at 400 and 495 cm^{-1}, and an intermediate frequency band at 790 cm^{-1}. In the high frequency band there is a peak at 1070 cm^{-1} and the other peak appears at 1200 cm^{-1}. With respect to experiment [109, 111, 112], and the size of our model (192 atoms) the calculated VDOS shows good agreement as regards the location of the principal peaks and the distribution of their intensities. We emphasize that trouble in first bands may be due to size effects.

Electronic properties

Here we report the calculated EDOS for the 648-atom model of g-SiO_2. The EDOS (Fig. 4.15) is in very good agreement with the x-ray photoemission spectra (XPS) [113, 114] and is comparable to the model of Sarnthein and coworkers [115]. Experimentally [113, 116, 117], the electronic structures of crystalline and amorphous SiO_2 are known to be very similar. In the occupied states three regions can be distinguished; the low-energy region at -20 eV is associated with oxygen $2s$ states.

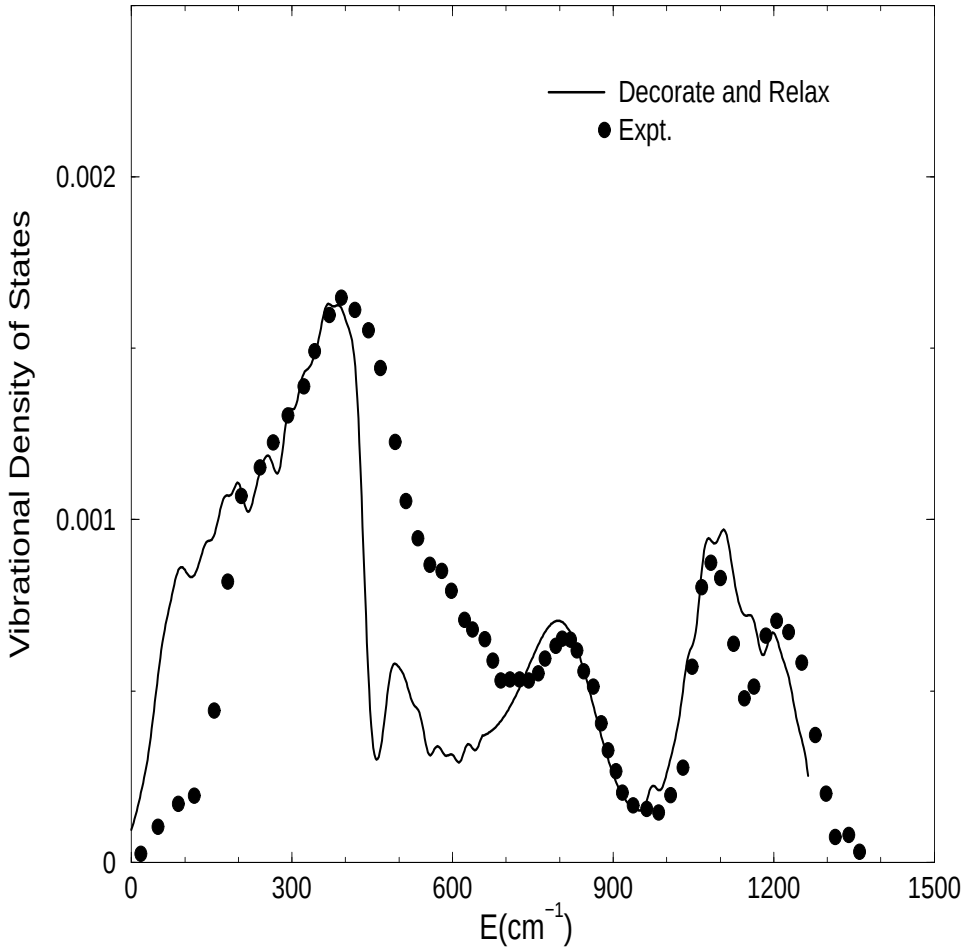

Figure 4.14: Calculated vibrational density of states of 192-atom model of g-SiO_2 compared to neutron scattering experiments [109].

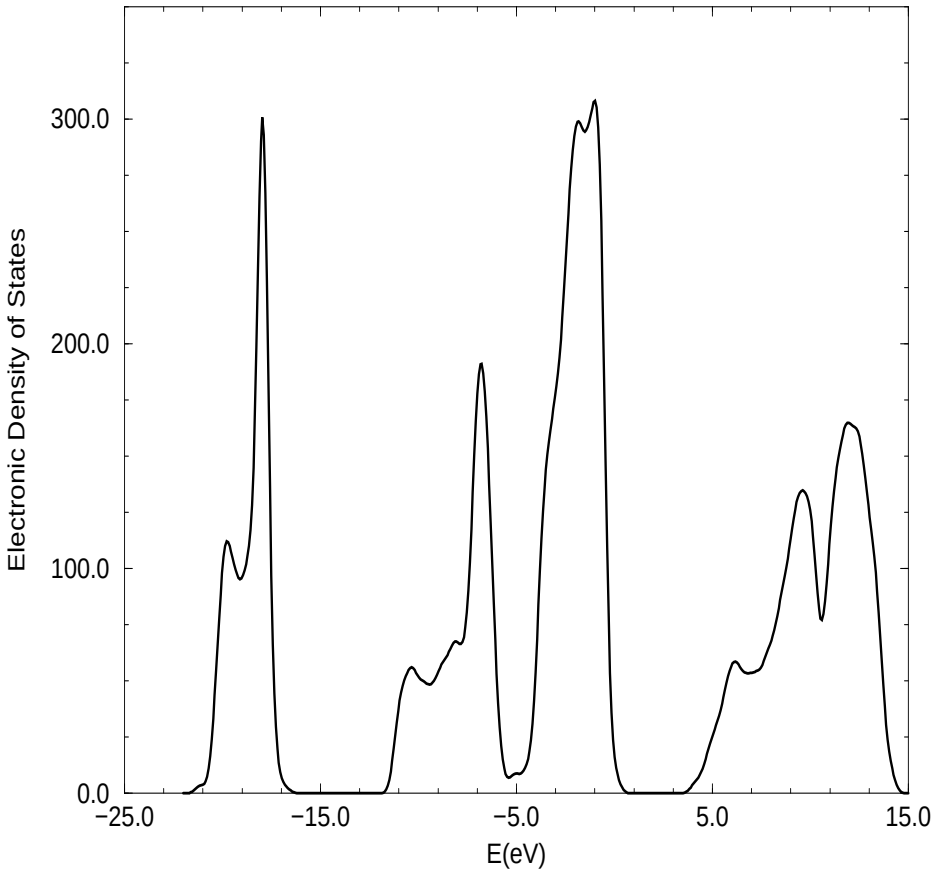

Figure 4.15: Electronic density of states of g-SiO_2. The Fermi level is at E=0.

The intermediate-energy region, -11 to -5 eV, which is strong bonding in character, involves bonding states between Si *sp* hybrids and O *p* orbitals; whereas the highest energy band composed of both weak-bonding and lone pair states (above -5 eV) arises from O *p* nonbonding orbitals.

4.1.4 Discussion and conclusion

Collaborative work with Chubynsky and Thorpe suggests that the method might be readily extended to non-stoichiometric glasses. These workers provided us with a decorated and unrelaxed model of glassy g-$GeSe_4$ based as before on a WWW model, but with additional Se added at random. The properties of the model were described in Ref.[83]. The structural properties of the model were in good agrement with experimental data. Comparing its VDOS with experiment obtained by neutron inelastic scattering [36], the spectrum exhibited the same features. Mainly two bands could be distinguished: a low energy acoustic band involving mainly extended interblock vibrations and a high energy optic band consisting of more localized intrablock vibrations. The two main bands were clearly separated by the tetrahedral breathing (A_1-A_{1c}) band.

We have presented the results of a large scale computer simulation using a different approach from the usual quench from melt scheme for modeling some binary glasses. We have shown that for certain binary IV-VI glasses (especially silica), decoration of bond-centered column VI atoms on tetrahedral amorphous networks leads with appropriate re-scaling and relaxation to highly realistic models of the IV-VI binary glasses. We investigated the topological structure, dynamics, and electronic structure of silica and silicon diselenide and compared with the experiments. Excellent agreement is found with the experimental data in the high Q region for all the S(Q) indicating that the short-range order is well reproduced for all configurations. In the low Q region, the appearance of the first sharp diffraction peak (peak amplitude and position) in S(Q) and its partials describes the intermediate-range order. In the Bhatia-Thornton concentration-concentration structure factor of g-$SiSe_2$, an FSDP is observed, indicating concentration fluctuations over intermediate-range distances.

SiO_2 is strikingly good unlike $GeSe_2$, $SiSe_2$ which are reasonable but not nearly so perfect. This may be due to the fact that silica consists entirely of corner sharing tetrahedra since our starting configuration already contains higher number of corner sharing, it makes easier to eliminate the few edge sharing present in the system. A simple decoration scheme works quite well for this system.

Overall the decorated scheme is much faster than the traditional methods (at least 10 times faster for a given interatomic interaction). To the extent that no scheme including "cook and quench" can be claimed to mimic the *physical* process of glass formation (because of the profoundly limited non-ergodic sampling of configuration space), this method should be evaluated by its success in reproducing the known experimental information.

4.2 Experimentally Constrained Molecular Relaxation: The Case of Glassy $GeSe_2$

A different approach to model construction implemented by McGreevy[14] and colleagues is the so-called "Reverse Monte Carlo" (RMC) method. Here, one explicitly sets out to make an atomistic model which agrees with experiments. RMC has been widely used to model a variety of complex disordered materials. This is accomplished by making Monte Carlo moves which drive a structural model toward exact agreement with one or more experiments. RMC is the ideal method to explore the *range* of configurations which are consistent with experiment(s). Without adequate limitation to a "physical" subspace of configuration space, it is unlikely to produce a satisfactory model. That is, only a subset of RMC models [which match the experiment(s)] is physically realistic (consistent with accurate interatomic interactions). The imposition of topological/chemical bonding constraints in RMC can ameliorate this problem, but not remove it entirely[18]. The mathematical structure of constrained RMC is a constrained optimization "traveling salesman" problem. In a previous implementation of constrained RMC Biswas *et al*[18] formed a positive definite (quadratic) cost or "penalty" function ξ, which was then minimized (ideally, but not practically) to zero for a structural model which exactly satisfies all constraints

imposed by Eq. 2.1. The method is easy to implement, though care must be taken to include the minimum number of independent constraints possible to reduce the likelihood of getting "stuck" in spurious minima. They have shown that inclusion of suitable constraints leads to models of a-Si much improved compared to RMC models using only the structure factor (first term of Eq. 2.1) as constraint[18].

As the creation of models of complex materials is a difficult task, it is of obvious advantage to incorporate *all* possible information in fabricating the model. We assert that an ideal model of a complex material should (1) be a minimum (metastable or global) of a suitable energy functional faithfully reproducing the structural energetics, (2) should contradict no experiments. When stated in these terms, our criterion seems quite obvious, yet current simulation schemes do not simultaneously accommodate both criteria, but focus only on one or the other.

In this section, we merge the power of *ab initio* molecular simulation with the *a priori* information of experiments to create models consistent with experiments and the chemistry implied by accurate interatomic interactions. To obtain joint agreement, we unite MD with the Reverse Monte Carlo (RMC) method. We name the scheme "Experimentally Constrained Molecular Relaxation" (ECMR). One can understand our scheme as a way to "tune" a structural model using MD within the space of *experimentally realistic* models as defined by RMC. We choose a troublesome and complex material with a long experimental and modeling history: g-$GeSe_2$.

From an algorithmic perspective, our scheme has important advantages. For example, to model a glass like $GeSe_2$ or SiO_2 using first principles methods, the method of choice is to form an equilibrated liquid, use some dissipative dynamics to simulate an (unphysically) rapid quench of the liquid into an arrested phase and finally to relax this to a local energy minimum, presumably at astronomical fictive temperature (high potential energy). Usually some repeated "annealing' cycles are also used. If one is interested in a glassy phase all the work of forming and equilibrating the liquid is redundant, and it is a pious hope that the arrested liquid will resemble a real glassy phase. Evidently the likelihood for success is strongly affected by topological and chemical similarity of the melt to the physical amorphous phase. If complex ordering "self-organization" or phase separation occurs in the physical amorphous

phase, the short simulations of conventional *ab initio* schemes will surely miss these important structural features. In this vein, we have used ECMR to construct models of a-Si with intermediate range order on a nanometer length scale[118] by inclusion of Fluctuation Electron Microscopy[119]. We note that successful techniques do exist to tackle the time-scale problem[120, 121], though these do not enable the inclusion of experimental information. Our method is efficient enough to enable the creation of a 647 atom model of g-GeSe2 using only a workstation. The method is at least a factor of five faster than a comparable quench from the melt simulation, with its inherent limitations.

4.2.1 Method

The obvious means to incorporate interatomic interactions into an RMC simulation is to add a constraint to minimize the magnitude of the force on all the atoms according to some energy functional or to minimize the total energy. For an *ab initio* Hamiltonian this is expensive, since Monte Carlo minimization of Eq. 2.1 requires a large number of energy/force calls. Thus, we have instead employed a simple "self consistent" iteration scheme (indicated in Fig. 4.16): (1) starting with an initial configuration C_1, minimize ξ to get C_2, 2) Steepest-descent quench C_2 with an *ab initio* method to get C_3, (3) subject the resulting configuration to another RMC run (minimize ξ again), repeat steps (2) and (3) until both the MD relaxed model and RMC models no longer change with further iteration. For the RMC component of the iteration, we make the conventional choice of using Monte Carlo for the minimization. This is simple and does not require gradients (and thus allows the use of non-analytic terms in Eq. 2.1 [122], if desired.

We emphasize that our method is *flexible*. Its logic suggests that one should include whatever experimental information is available. In this work, we limit ourselves to the pair-correlation functions. In principle, other experiments could be included as well. These might be costly to include (for example to compel agreement with the vibrational density of states, the dynamical matrix would be required at each iteration). The method is equally suited to fast empirical potentials, which would allow studies of very large models. It is also possible to force a close fit to some

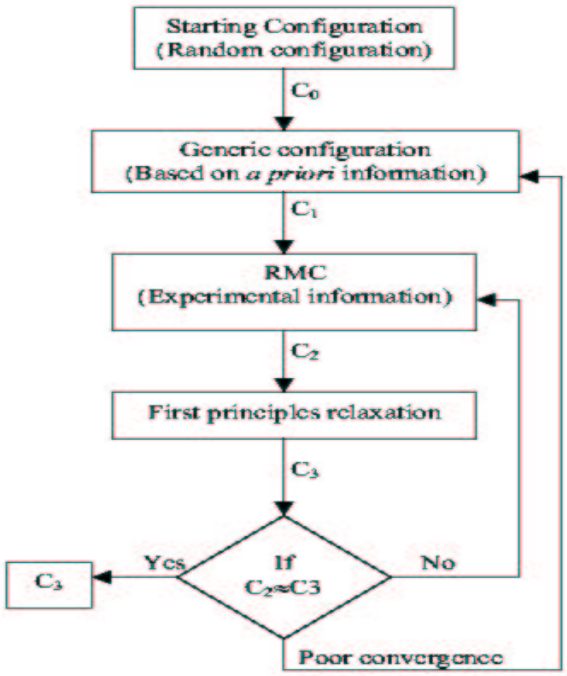

Figure 4.16: Flow diagram for the "Experimentally Constrained Molecular Relaxation" method of this paper.

restricted range of data, and a less precise fit elsewhere if desired. Our scheme also provides insight into the topological signatures of different constraints (experimental or otherwise). Chemical and or topological constraints could also be maintained as part of the RMC iteration.

Our method can be understood as a way to minimize an effective potential energy function $V_{eff}(R) = V(R) + \Lambda\zeta(R)$, where $V(R)$ is the potential energy of the configuration (denoted by R), $\Lambda > 0$, and ζ is a non-negative cost function enforcing experimental (or other) constraints as in Eq. 2.1. Empirically, we find that it is possible to find configurations that simultaneously approximately minimize both terms (which implies that the choice of Λ is not very important). It is also clear that our method is really *statistical*: in general one should generate an ensemble of conformations using ECMR. For adequately large models, self averaging can be expected; in this study of large (647 atom) models of g-$GeSe_2$ we find similar results for two runs; for small systems a proper ensemble average is required.

Our method is new and as such needs to be studied and developed in a number of ways. Nevertheless, we show in this work that it is relatively easy to model a particularly challenging material with significant advantages in both experimental plausibility of the model and computational efficiency of the algorithm.

4.2.2 Application to glassy $GeSe_2$

We apply ECMR to glassy $GeSe_2$, a classic glass forming material with challenging physical and technical issues: (1) it displays nanoscale order: a "first sharp diffraction peak" (FSDP) is observed in neutron diffraction measurement, (2) the packing of GeSe tetrahedra involves both edge- and corner- sharing topologies; (3) the material has interesting photoresponse (understanding of which requires the electronic structure, (4) the material is difficult to simulate with *ab initio* techniques[31, 83, 93, 92]. The model used in our calculation consists of 647 atoms of Ge and Se in a cubic box of size 27.525 Å.

In the nomenclature of Fig. 4.16, C_1 is obtained by constraining the coordination number (2 for Se, 4 for Ge) and the bond-angle distribution of Se-Ge-Se to an approximate Gaussian with an average bond angle 109.5°. The initial network was "generic"

and included none of the detailed chemistry of Ge and Se aside from the coordination constraint. Using the method of isotopic substitution, Salmon and Petri [90] were able to separately measure the three (Ge-Se, Ge-Ge and Se-Se) partial structure factors of g-$GeSe_2$. We enforced all three partials (in real space) in the RMC component of the loop in Fig. 4.16. The MD relaxation was done with FIREBALL[21]. It was found that after the fourth iteration, S(Q) hardly changed.

Structure

In Fig. 4.17, we compare the RMC, ECMR and experimental structure factors. While the agreement is very good, it is not perfect. This is to be expected for three reasons: (1) consistency between data and Hamiltonian is never exact; (2) our cell contains 647 atoms, which is compared to the thermodynamic limit and (3) we chose to constrain our model using real space data, which involves Fourier transforms and windowing (this introduces only small errors in this data set). In Fig. 4.17 we highlight the differences between experiment[90], a quench from the melt model[93] and the new ECMR model. In the inset of Fig. 4.17, we also illustrate the level of agreement using a pure RMC approach, which is similar to the ECMR result and notably better than quench from the melt. For reference, we have reproduced the full partial structure factors elsewhere[118].

Note in Fig. 4.17 that the first sharp diffraction peak (FSDP) is well reproduced, (very close in width and centering, and much improved from all previous models in height). Moreover, as for our "Decorate and Relax" (DR) method[86], the large Q structure closely tracks experiment (unlike the experience for quench from the melt models). These features are of course "built in"; we show here that the method does preserve every important feature of the structure of the glass manifested in S(Q). In Table 4.5, we show the average force per atom at the beginning of each call to MD relaxation; good convergence is observed. Subsequent discussion in this paper is for the last step of the MD, with forces less than 1×10^{-2} eV/Å. it was not obvious to us in the beginning that RMC and first principles interatomic interactions could be made "self-consistent", but for this system at least, good convergence is possible. It

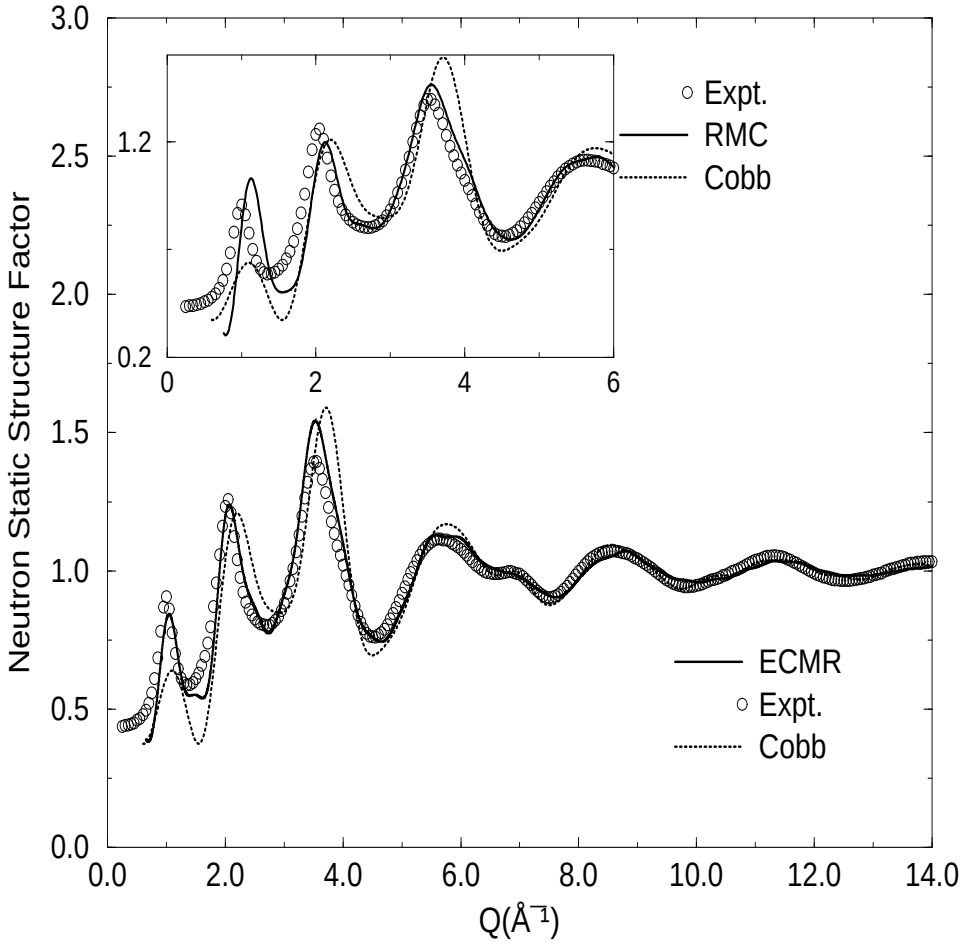

Figure 4.17: Neutron-weighted static structure factor, comparing ECMR model, experiment[90] and a quench from the melt made with the same Hamiltonian used with ECMR[93]. Inset: blowup of small-Q region showing RMC model (eg, without ECMR iterations), experiment[90] and quench from the melt[93]. The first sharp diffraction peak is closely reproduced by ECMR and RMC, and is present but weak in the quenched model.

Table 4.5: The convergence of ECMR described in the text.

ECMR iteration	Average force/atom (eV/Å)
1	2.242×10^{-3}
2	7.365×10^{-3}
3	6.518×10^{-4}
4	5.019×10^{-4}
5	4.773×10^{-4}
6	4.903×10^{-4}
7	4.686×10^{-4}
8	4.642×10^{-4}

is likely that some initial conformations C_1 will get "stuck" and require a new start, but we have not encountered difficulty with this yet.

An important indicator of network topology of $GeSe_2$ glass is the presence of edge sharing and corner sharing tetrahedra. Raman spectroscopy [123] and Neutron diffraction [32] studies have indicated that 33% to 40% of Ge atoms are involved in edge sharing tetrahedra. The fraction in our model is found to be 38%. This was not "built in" to our modeling, and is a pleasing prediction arising from the procedure. We also have observed that 81% of Ge atoms in our model are four-fold coordinated of which approximately 75% form predominant Ge-centered structural motifs $Ge(Se_{\frac{1}{2}})_4$ while 6% are ethane-like $Ge_2(Se_{\frac{1}{2}})_6$ units. The remaining Ge atoms are three-fold coordinated and are mostly found to be bonded as Ge–Se_3 units. On the other hand, the percentage of two-, three- and one-fold coordinated Se atoms are 72%, 18% and 10% respectively. Mössbauer experiments, where Sn was used as a Ge probe [124], estimated that the fraction of Ge involved in dimers is 16% which is again in favor of our model.

By integrating partial radial distribution functions via Fourier transform of structure factors Petri and Salmon[90] obtained nearest neighbor coordination numbers $n_{Ge-Ge} = 0.25$, $n_{Se-Se} = 0.20$, and $n_{Ge-Se} = 3.7$ that corresponds to average coordi-

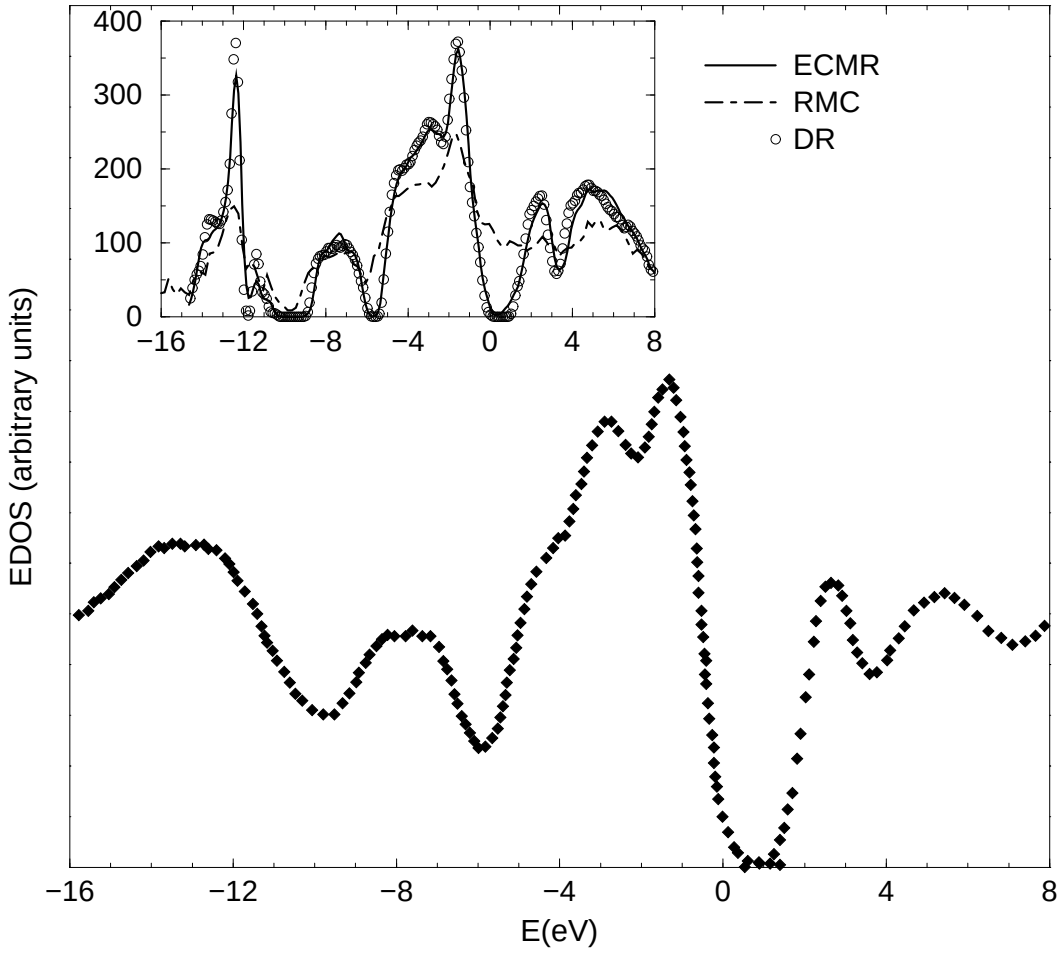

Figure 4.18: The electronic density of states (Gaussian-broadened Kohn-Sham eigenvalues) for ECMR model of $GeSe_2$, along with the RMC model (not using *ab initio* information) and a "decorate and relax" (DR) model made with the same Hamiltonian (inset). The XPS[40] and IPES[125] data show the occupied (valence band) and unoccupied (conduction band) part of the spectrum. See Table 4.6 for numerical comparison of the peaks. The Fermi level is at E=0. Both DR and ECMR reproduce the state density closely, while the RMC model lacks an optical gap.

nation number $\bar{n} = 2.68$. The corresponding values from our model are: $n_{Ge-Ge} = 0.17$, $n_{Se-Se} = 0.30$, $n_{Ge-Se} = 3.68$, and $\bar{n} = 2.66$. The partial and total coordination numbers, therefore, agree well with experiments (as expected) and are consistent with the 8-N rule which predicts $\bar{n} = 2.67$. The percentage of homopolar bonds present in our model is found to be about 6.2 % which is again very close to the value 8 % noted by Petri and Salmon [90].

Electronic density of states

Having studied structural properties, we now briefly analyze electronic properties of our model. Since structural and electronic properties are intimately related, an examination of electronic density of states provides an additional test of the validity of the model which is derived jointly from structural information and a suitable interatomic interaction. The electronic density of states (EDOS) is obtained by convoluting each energy eigenvalue with suitably broadened Gaussian. The ECMR EDOS in the inset of Fig. 4.18 agrees quite well with experimental results obtained from x-ray photo-emission [40] (XPS), inverse photo-emission spectroscopy [125] (IPES) and ultraviolet photo-emission spectroscopy [41] (UPS) measurements as well as with those obtained in recent theoretical studies [126, 127, 93, 83]. It is remarkable that the Kohn-Sham eigenvalues (obtained in the Harris approximation) agree so well with the photoelectron spectroscopy[128], particularly as the energy-dependent matrix element is not included in the calculation. The substantial splitting between the first two peaks of the valence bands named the A_1 and A_2 peaks is also well-pronounced. The position of the principal peaks obtained from the different models and experiment are tabulated in Table 4.6. The similarity of experiment and theory suggests the utility of a study of the Kohn-Sham eigenvectors to enable atomistic identification of defects and bands illustrated in Fig. 4.18.

We also compare the EDOS for an RMC model (making no use of an *ab initio* Hamiltonian, only the static structure factor, the 8-N rule, and the initial heteropolar bonding). The RMC model does very poorly, without even showing an optical gap, despite the excellent static structure factor (obtained by construction). By contrast, our DR and the quench from the melt model (not shown) are very close to experiment

Table 4.6: The positions of the A_1, A_2, A_3 and B peaks in the EDOS of $GeSe_2$ glass compared to experimental results [41].

(eV)	A_1	A_2	A_3	B
Present work	-1.55	-3.0	-4.6	-7.4
Experiment [41]	-1.38	-3.0	-4.6	-7.8
Melt and quench[93]	-1.4	-2.7	-4.6	-7.0
Decorate and relax[83]	-1.36	-2.8	-4.5	-7.2

and ECMR. This result emphasizes the need to compute the density of electron states as an important gauge of the credibility of a model.

Vibrations

It is useful to also examine the vibrational density of states (VDOS) of our ECMR model due to the close relationship to its atomic-scale structure and its dynamical properties. The computational methodology and VDOS was reported elsewhere [93]. Comparing our VDOS with experiment obtained by inelastic neutron-scattering [129], the spectrum exhibits the same features with somewhat better resolution than results we reported in Ref. [93]. Three bands can be distinguished: a low energy acoustic band involving mainly extended interblock vibrations and a high energy optic band consisting of more localized intrablock vibrations. The two main bands are clearly separated by the tetrahedral breathing (A_1-A_{1c}) band. The overall agreement is quite reasonable, including an A_1-A_{1c} splitting.

In Fig. 4.19, we compare the vibrational density of states of the ECMR model with experiment[129] and for completeness our decorate and relax model including 648 atoms along with the ECMR model. We do not present the RMC result, as the system is not at equilibrium according to FIREBALL, which would lead to many imaginary frequencies in the density of states. While generally DR and ECMR are quite similar, we note that the A_1 band for the ECMR model shows a proper A_1-A_{1c} splitting, whereas there is no such feature for the DR model. This is probably because

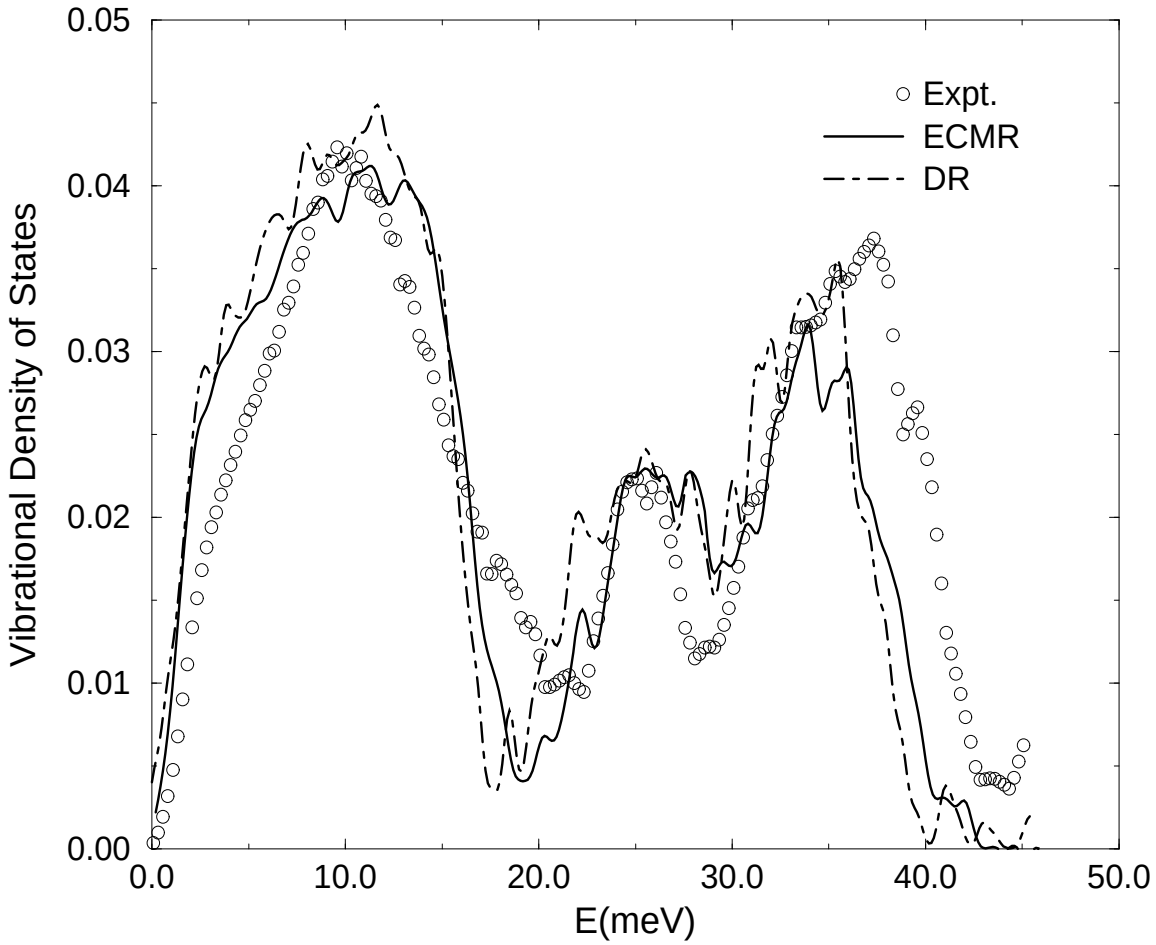

Figure 4.19: Vibrational density of states computed from dynamical matrix. Nomenclature similar to Fig. 4.18; note the lack of an A_1-A_{1c} splitting in the DR model, a consequence of very few edge sharing tetrahedra in the DR network.

the ratio of edge to corner sharing tetrahedra is very different ($\approx$ 29% of Ge atoms are involved in edge sharing tetrahedra in the DR model). This illustrates that the VDOS is a useful gauge of medium range order (tetrahedral packing) in this glass.

4.2.3 Summary

In summary, we have proposed a new method which enables the inclusion of *a priori* information (experimental or otherwise) into molecular simulation. We have shown that the method is effective for a challenging material, g-$GeSe_2$.

4.3 Building Blocks: The Case of $GeSe_{1.5}$

It is much more challenging to construct models at composition far from stoichiometry and overconstrained[130]. For complicated glasses, it sometimes happens that the quench from the melt technique fails to reproduce the correct structure. With no *a priori* information, models obtained either contain too many defects or their structures are very poor compared to experiments (for example, incorrect static structure factor S(Q) for large Q). In this section, we use the notion of inferring complex "building blocks" to produce model of $GeSe_{1.5}$. The idea is based on the following assumptions: the local short-range chemical order does not change dramatically between large system and small system; the chemical order of a small cell of a material can be correctly obtained by long *ab initio* MD simulation. Basically, the idea[131] is to use accurate *ab initio* MD to produce a small nearly perfect sub-unit cell, the "pseudo-crystal", by a very extended annealing for a particular composition. This optimized structure, which includes the appropriate chemical ordering for the given composition (and should also satisfy known experimental information about coordination and chemical order for that glass) will be used to make a larger supercell, which can then be melted and quenched.

4.3.1 Model

Total energy/force code

We use FIREBALL, an approximate *ab initio* density functional code in the LDA developed by Sankey and co-workers [21]. In this method the Harris functional is used in a scheme with the mathematical structure of nonorthogonal tight-binding, and the use of no free parameters in constructing the Hamiltonian matrix. The basis set is minimal (for this system one s and three p slightly excited pseudo-atomic orbitals per site).

MD procedure

We began by randomly placing small numbers of atoms in a cubic supercell according to the desired composition [8 germanium and 12 selenium atoms] with the minimum acceptable distance between atoms 2 Å. The size of the cubic cell, 8.37 Å, was chosen to make the density of the glass close to the experimental data [29], 0.0341 $Å^{-3}$. The cell was annealed and we obtained well thermalized melt at 3500 K. We took three steps to cool the cell. First, the cell was equilibrated to 1436 K for 2.5 ps; then it was slowly cooled to 300 K for approximately 7 ps. The MD time step was 2.5 fs. In the final step, the cell was steepest descent quenched to 0 K and maximum forces smaller in magnitude than 0.02 eV/Å. The final configuration obtained played the role of the "pseudo crystal" for the bigger cell. To build a larger supercell we repeated the pseudo crystal over two periods and obtained a system of 540 atoms. We then melted the large cell at 1500 K for 4 ps, cooled over 300 K for 8 ps and quenched to 0 K. All calculations were performed at constant volume using the Γ point to sample the Brillouin zone to compute energies and forces.

4.3.2 Structural properties

Fig 4.20. shows the neutron static structure factor and pair correlation function for $GeSe_{1.5}$ from our simulation along with the experimental data [26]. Also shown are the results from the standard cook and quench method. Our calculations show good agreement with experiment. Some points of discrepancy are to be expected for

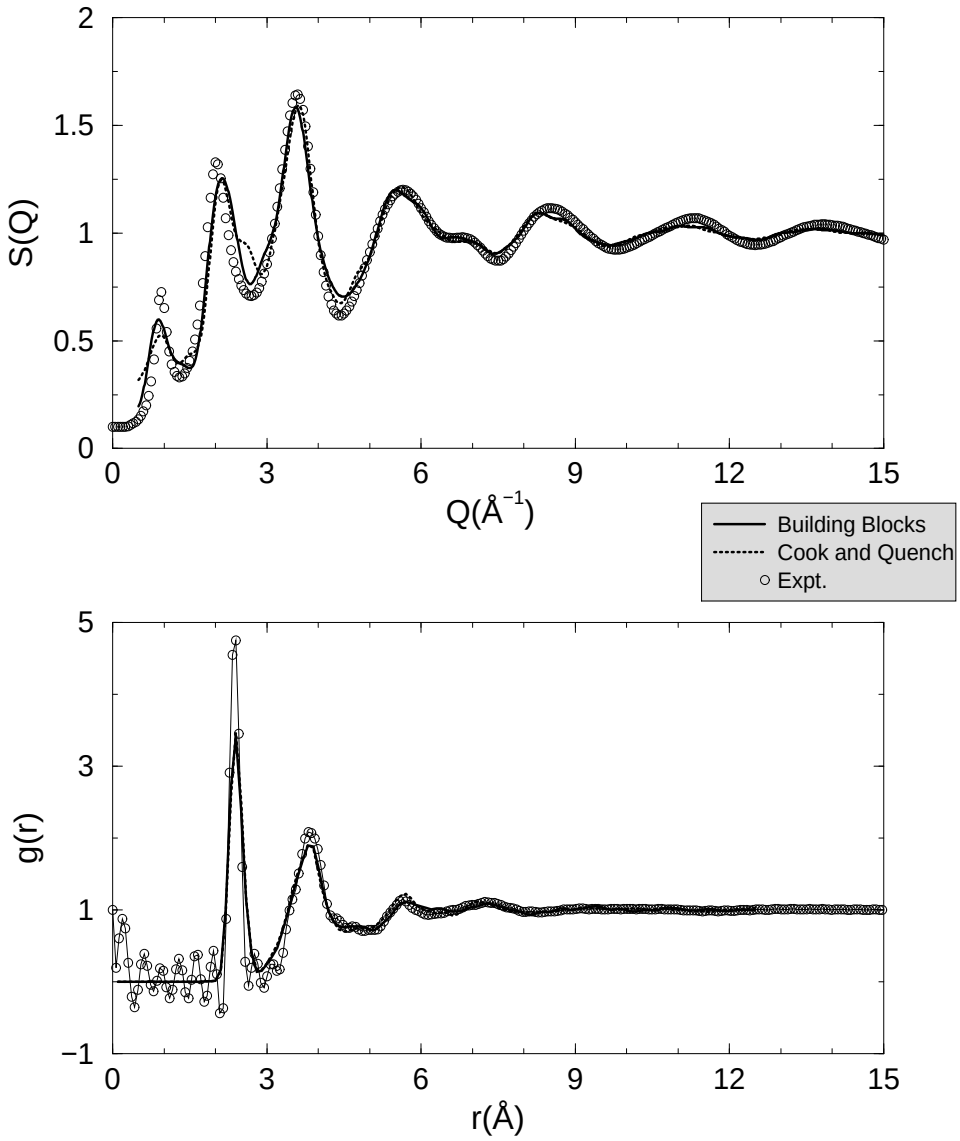

Figure 4.20: Neutron-weighted static structure factor, comparing building blocks model, a quench from the melt made with the same Hamiltonian, and experiment[26]. Also shown is the pair correlation function.

Table 4.7: Averaged bonding distances in g-$GeSe_{1.5}$. The distance is in Å.

Bond type	Building Block	Cook and Quench	Experiment[26]
Ge-Ge	2.43	2.44	2.42
Ge-Se	2.36	2.36	2.36
Se-Se	-	2.33	-

different reasons. The most obvious is the size of our models (540 atoms), which is compared to the thermodynamic limit. In Fig. 4.20 we also highlight the differences between experiment, a quench from the melt model and the building blocks model. The FSDP is well reproduced, (close in width and centering, and more improved from the melt and quench model in height). Another substantial difference between the quench from the melt and the building blocks models are near 2.5 $Å^{-1}$, at the minimum after the second peak. The first peak in g(r) occurs at a higher r value than for the other compositions (Ge_xSe_{1-x}, $0 \leq x \leq 0.4$). This can be understood in terms of the disappearance of Ge-Se and Se-Se bonds, and the appearance of additional homopolar Ge-Ge bonds. The composition of $GeSe_{1.5}$ glass is such that on an average one Ge-Ge bond will be present per Ge site.

In Fig. 4.21 we illustrate the partial structure factor and partial pair correlation function for the building block and the cook and quench models. The Ge-Se pairs provide the dominant contribution to the first shell of the pair correlation function with an average bond distance 2.36 Å. In Table 4.7, we list the averaged bonding distances present in the models and compare to experiment[26]. Our results are in good agreement with the neutron diffraction measurements.

Where coordination is concerned, we note that in the building blocks model, about 67.60% of Ge are fourfold coordinated and 31.48 % are threefold coordinated whereas 67.60% of Se are twofold, 26.54% are threefold and 5.56% are onefold coordinated. The cook and quench model is a different story: about 73.61% and 25.0% of Ge are respectively fourfold and threefold coordinated; 60.20%, 30.56% and 9.26% of Se are respectively twofold, threefold and onefold coordinated. We have also noted the

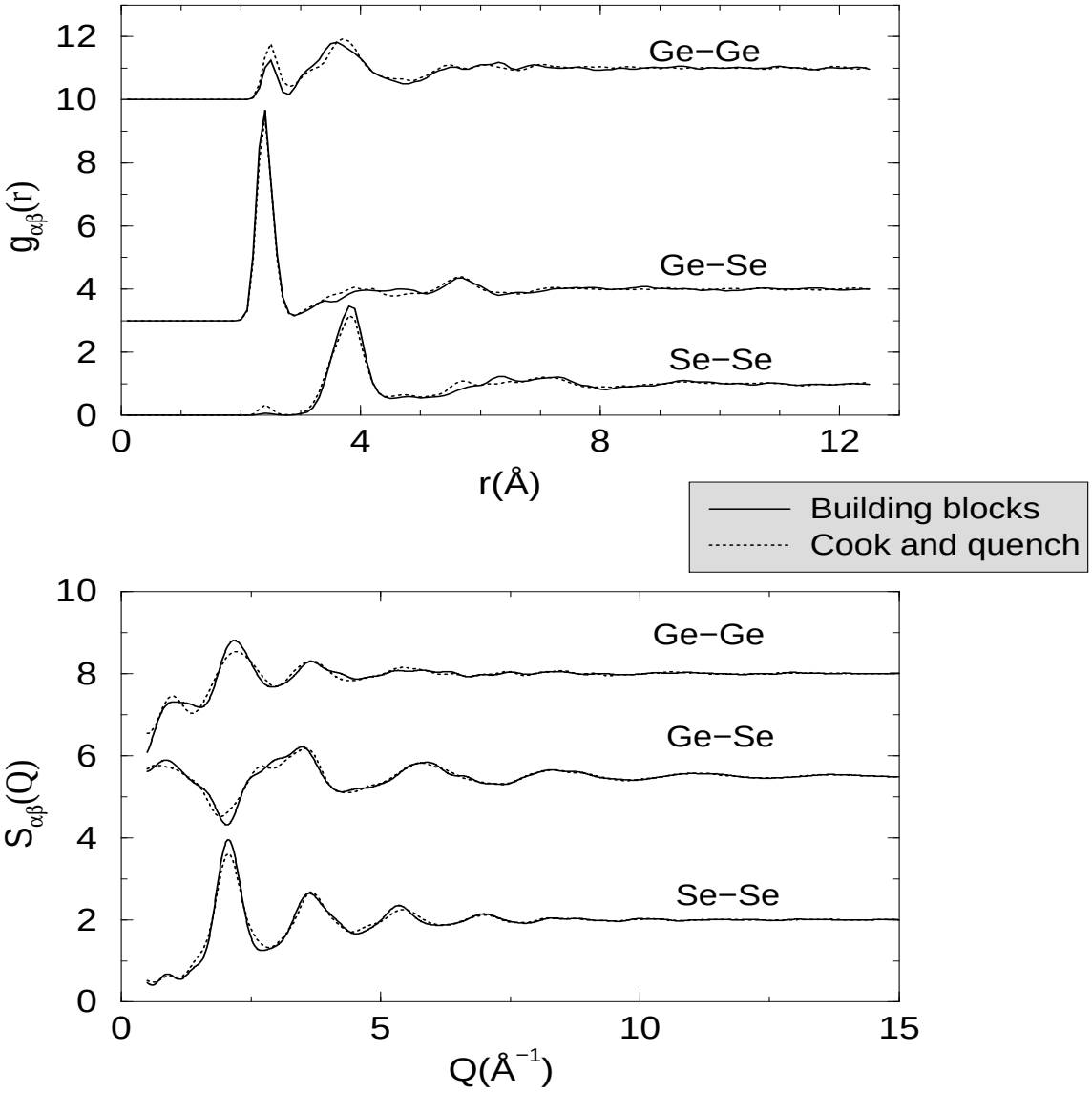

Figure 4.21: Partial pair correlation function and partial structure factor, comparing building blocks model and a quench from the melt model of g-$GeSe_{1.5}$.

presence of fivefold and twofold Ge in the cook and quench model. Where chemical order is concerned, the building blocks model has 93.91% of Ge-Se bonds and 5.43% of Ge-Ge bonds compared to the cook and quench models with 88.38% Ge-Se, 8.88% Ge-Ge and 2.74% Se-Se. The significant amount of Se-Se wrong bonds in the cook and quench model explains the presence of a significant peak in the $g_{SeSe}(r)$. In the building blocks model a fraction is observed (0.66%). This result is in accordance with the chemically ordered continuous random network model which predicts that in Ge rich glasses, Se-Se homopolar bonds are nonexistent. By integrating the pair correlation function we obtained average coordination number n. In the building blocks model we found n to be 2.80 compared to 2.81 in the cook and quench model. In EXAFS experiments Zhou *et al*[33] found a coordination number of 2.80 while Petri *et al* obtained 2.81. Our results are consistent with the presence of $Ge_2Se_{6/2}$ ethane like units in glassy $GeSe_{1.5}$.

4.3.3 Electronic properties

They are analyzed through the electronic density of states (EDOS). Fig. 4.22 shows the EDOS and the species projected density of states of the building blocks model of $GeSe_{1.5}$. Our EDOS agrees well with experimental results obtained from x-ray photo-emission spectroscopy [40] (XPS), inverse photo-emission spectroscopy [125] (IPES). All the relevant experimental features are also found in the calculated EDOS, providing further support for the reliability and accuracy of the method. The Γ point optical band gap of our model is 1.67 eV. It is quite remarkable that there are no states in the band gap considering the number of topological defects in our model.

4.3.4 Vibrational properties

The vibrational properties of our model are analyzed through the vibrational density of states (VDOS). Fig. 4.23 shows the VDOS and the species projected density of states of $GeSe_{1.5}$. The VDOS can be divided in three bands. A low-energy acoustic band, sensitive to connectivity, goes up to 20 meV, and a high energy optic band

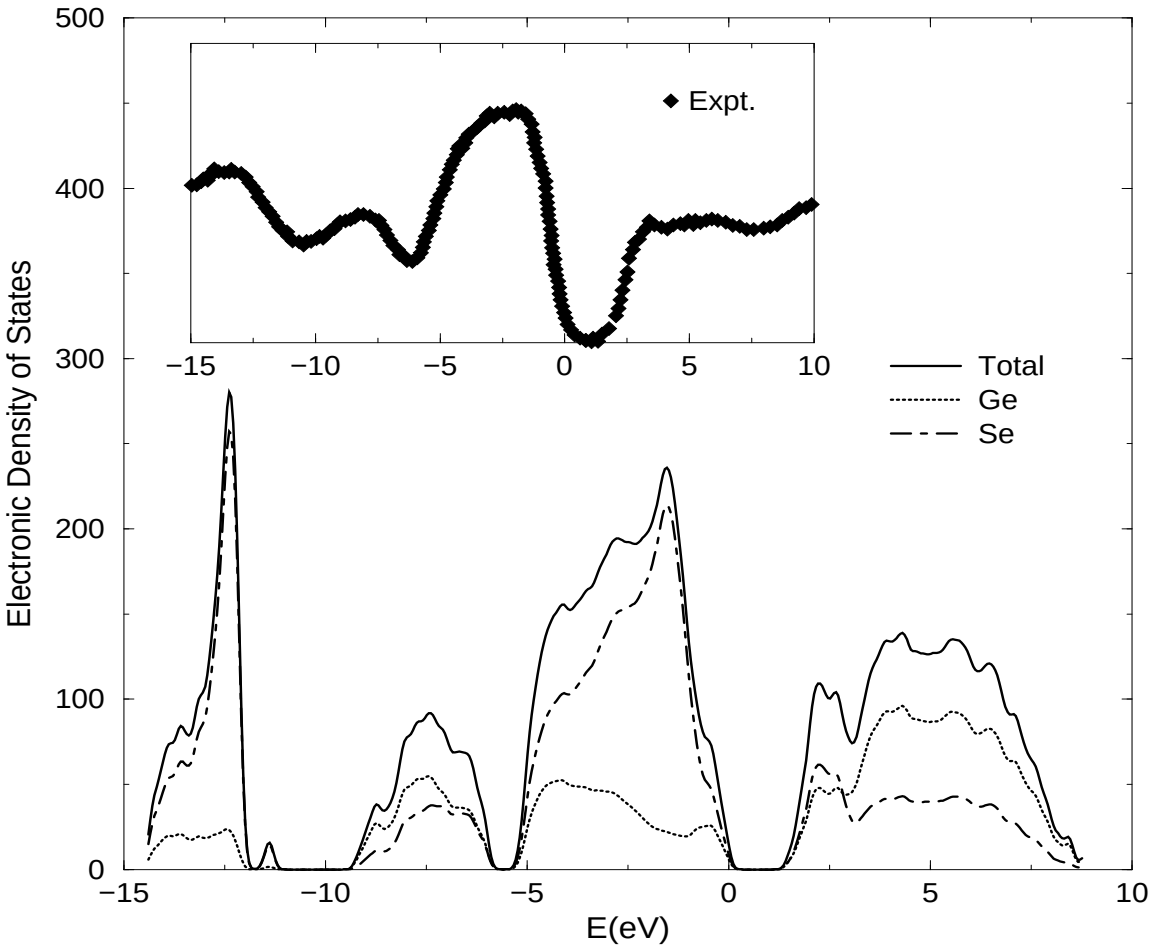

Figure 4.22: Electronic density of states (solid lines) and species projected electronic density of states for Se (dot-dashed lines) and Ge (dotted lines) for g-$GeSe_{1.5}$ obtained from *ab initio* simulations and compared to the XPS[40] (valence band) and IPES[125] (conduction band).

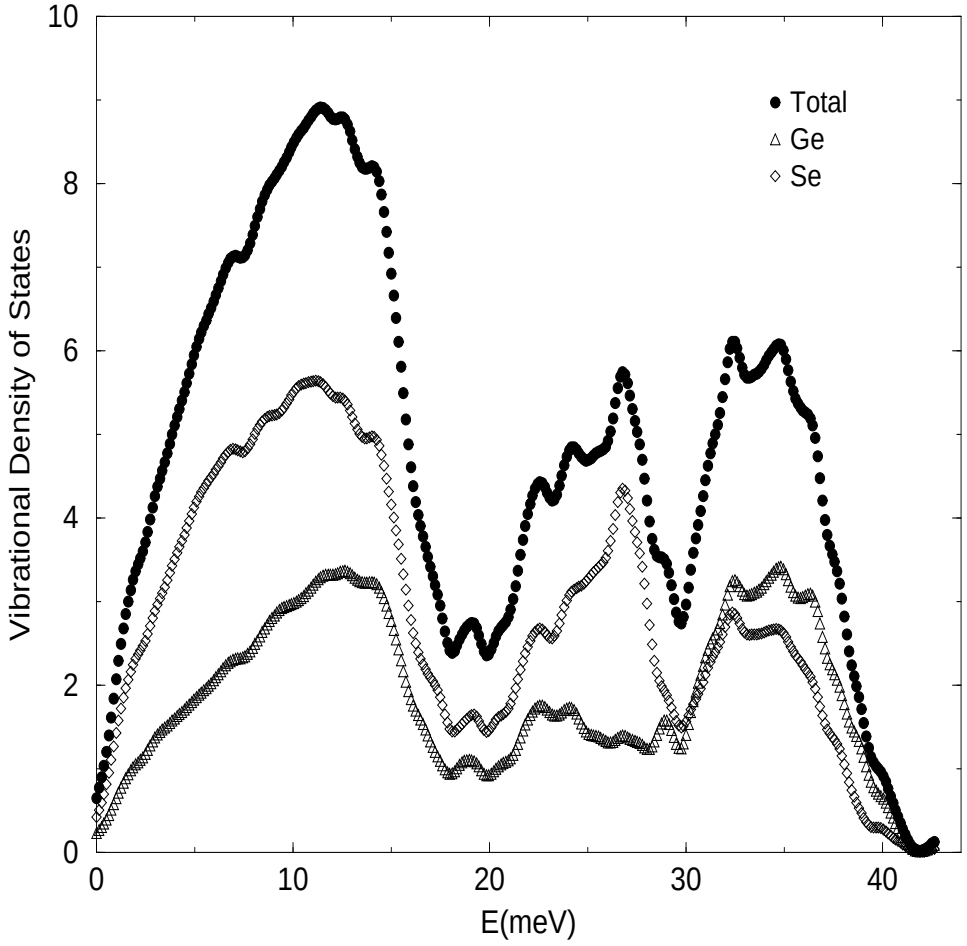

Figure 4.23: Vibrational density of states and species projected vibrational density of states for Se and Ge for g-$GeSe_{1.5}$ obtained from *ab initio* simulations.

that decays near 40 meV, consisting of more localized intrablock vibrations. The two main bands are clearly separated by the tetrahedral breathing (A_1-A_{1c}) band. Experimentally [37], it has been shown that this band is a function of Ge concentration in Ge_xSe_{1-x} glasses. As Ge concentration increases, the A_1 mode rises in the gap.

4.3.5 Discussion

The notion of inferring building blocks has been used by a few authors to model amorphous materials. For example Ouyang and Ching[132] constructed a model of amorphous Si_3N_4 based on a judicious choice of elementary subunits which satisfy local bonding. The subunits were then connected carefully to meet the bonding requirements of the corner atoms. The randomness was introduced through the random distribution of different subunit types. Although appealing by its simplicity, this approach suffers from long-range crystalline correlations and consequently cannot lead to satisfactory models of amorphous materials[133]. Our method is different from theirs. In our approach the subunit cell called "pseudo-crystal" was built from first principle and the unphysical correlations between the subunit cell was destroyed through the melting process.

Overall the structural properties of the building blocks model were in excellent agreement with experimental data. The discrepancy in the height of the FSDP in S(Q) is probably linked to the model size. There is no evidence that a better hamiltonian will reproduce the first peak correctly. This pattern has also been observed in $GeSe_4$. In the cook and quench model, the FSDP is less pronounced and the model contains more structural defects.

The approach of inferring building blocks has proven to be successfull and can easily be applied to non stoichiometric and complicated glasses. In their work, Zhang and Drabold[131] made improved models of Ge-As-Se glasses. The models had a state free optical gap and a satisfactory vibrational spectrum. By contrast a direct quench from the melt approach *with the same total energy functional* starting with randomly placed produced highly unrealistic results, for the pair distribution and with far too many electronics defects.

4.4 Conclusion

In this chapter we have presented new modeling schemes for binary IV-VI glasses. We have applied these approaches to produce realistic models of glasses. The models obtained agree with an array of experiments. While the three approaches differ from one to another they have something in common: the inclusion of primitive *a priori* information. The starting point for the decorate and relax (DR) is a WWW model of *a*-Si or *a*-Ge where all the Si or Ge atoms are fourfold coordinates, whereas for the ECMR and building blocks are a random configuration and pseudo crystal respectively. In the ECMR the *a priori* information is added in the cost function. The pseudo crystal obtained from the quench from the melt already contains the basis structure of the glass.

Decorate and relax is the simplest, and fastest approach compared to the two others. It works well for IV-VI_2 compositions, especially silica. Also it gets large Q behavior of S(Q) right. The method is very efficient computationally. The ECMR which is a combination of RMC and first-principles MD is much faster and more efficient than the building blocks method. It improves significantly the intensity of the FSDP. The building blocks is slower because it derives from the quench from the melt. The resulting models are better than the standard quench from the melt models. The models can be improved if the pseudo crystal is generated from either DR or ECMR. In that case, the resulting pseudo crystal will have the large Q behavior of S(Q) right and a much improved FSDP.

Chapter 5

Conclusion and Further Considerations

5.1 Conclusion

In this work, we have presented the results of large scale computer simulations using different approaches ranging from the usual quench from the melt to the building blocks method. Using the quench from the melt we were able to produce realistic models of non-stoichiometric binary glasses, $GeSe_4$ and $GeSe_9$. The models are in good agreement with all the structural properties, vibrational properties and electronic density of states. A detailed analysis of the atomic structure of these glasses shows that the Ge-centered tetrahedra are the predominant coordination motifs in g-$GeSe_4$ and that the structure of g-$GeSe_9$ consists of Se-chain segments which are cross-linked by $Ge(Se_{1/2})_4$ tetrahedra.

The quench from the melt has also been used to produce models of Ge-Se glasses heavily doped with Ag ($(GeSe_3)_{0.90}Ag_{0.10}$ and $(GeSe_3)_{0.85}Ag_{0.15}$). We studied the dynamics of the network of these glasses with an emphasis on the Ag ions. We highlighted the existence of trapping centers and explicitly illustrated the trapping and release process from thermal MD simulation. The models appear to be in excellent agreement with an array of experiments and should be useful for subsequent studies of these interesting materials.

Providing *a priori* information in the starting model also serves as a useful alternative. We have developed new methods to overcome the limitations of the quench from the melt method (time scales shorter in the simulation and large Q behavior in S(Q)). For certain binary IV-VI glasses, especially silica, decoration of bond-centered column VI atoms on tetrahedral amorphous networks leads with appropriate re-scaling and relaxation to highly realistic models of IV-VI binary glasses. The models obtained present some additional features such as a proper asymptotic behavior in S(Q) for large Q. The method has been used to produce other models such as $GeSe_2$ and $SiSe_2$. The other two methods developed are the experimentally constrained molecular relaxation (ECMR) that combines a reverse Monte Carlo approach with approximate first-principles molecular dynamics, and the notion of inferring complex building blocks. We have shown that the ECMR is effective for a challenging material, g-$GeSe_2$. The building block approach has been successfully applied to produce a realistic model of Ge-rich glass $GeSe_{1.5}$. A comparison with a model obtained from a direct quench from the melt technique shows a significant improvement in the structural properties of $GeSe_{1.5}$.

The new methods developed here are general and can be extended to other complex materials. With the success of Ge-Se glasses heavily doped with Ag, it prove possible to compute the inputs into phenomenological hopping/trapping models from first principles dynamical simulation. It also shows that first principles simulation is a powerful tool to reveal the motion of ions in glass, in particular in solid electrolytes which are of practical interest. With respect to the flexibility of the ECMR, the method can also be extended to liquids and DNA.

5.2 Further Considerations

The inclusion of *a priori* information in the model making is useful to overcome the limitations of MD simulation time scales. Following this idea, we developed methods to produce realistic models of complex glasses. The simplest one, DR, works well for IV-VI_2 compositions. But its general applicability remains unclear. It is worthwhile to further explore the method. The other method, ECMR, has been successfully

applied to generate g-$GeSe_2$. The flexibility of its cost function makes the approach very efficient and can be extended to study medium-range order (MRO) in binary glasses such as g-$GeSe_2$. It has been suggested that the MRO is sensitive to the ratio of edge to corner sharing tetrahedra. This can be done by constructing a cost function comprising a fluctuation electron microscopy (FEM) signal.

The notion of inferring building blocks has proven to be efficient in producing amorphous materials. The starting point is a pseudo crystal obtained from the standard quench from the melt technique. One might extend the scope of this technique by constructing the pseudo crystal using either the DR or the ECMR technique. Indeed the pseudo crystal will have a large Q behavior of S(Q) right and much improved structural properties.

Having reliable models of GeSe glasses heavily doped with Ag, one can study the photodiffusion of the Ag into Se-rich chalcogenide glasses. Such glasses are the active element in programmable metallization cell (PMC) devices. These devices rely on ion transport in the solid-state electrolyte produced to create electrically programmable resistance states. It is also worthwhile to further study the hopping/trapping mechanism in order to describe the ion conductivity between the ionic states in the solid-state electrolyte.

Bibliography

[1] I.D. Aggarwal, J.S. Sanghera, J. Optoelectron. Adv. Mat. **4**, 665 (2002).

[2] M. Mitkova, in *Amorphous Semiconductors and Insulators*, edited by P. Boolchand, World Scientific Press LTD, 2000, p. 813.

[3] S.R. Ovshinsky, in *Non-Crystalline Materials for Optoelectronics*, edited by G. Lucovsky and M. Popescu, INOE, 2004, p. 1.

[4] M.F. Thorpe, D.J. Jacobs, M.V. Chubynsky and J.C. Phillips, J. Non-Cryst. Sol. **266**, 859 (2000).

[5] P. Boolchand, D.G. Georgiev, and B. Goodman, J. Optoelectron. Adv. Mat. **3**, 703 (2001).

[6] P. Boolchand, D.G. Georgiev, and M. Micoulaut, J. Optoelectron. Adv. Mat. **4**, 823 (2002).

[7] T. E. Faber and J. M. Ziman, Phil. Mag. **11**, 153 (1965).

[8] P. Ordejón, D. A. Drabold, R. M. Martin, and S. Itoh, Phys. Rev. Lett. **75**, 1324 (1995).

[9] D. A. Drabold, Jun Li, and De Nyago Tafen, J. Phys.: Condens. Matter **15**, S1529 (2003); Jun Li and D. A. Drabold, Phys. Rev. Lett. **85**, 2785 (2000).

[10] G. Fabricius, E. Artacho, D. Sanchez-Portal, P. Ordejon, D. A. Drabold, and J. M. Soler, Phys. Rev. B **60**, R16283 (1999).

[11] F. Wooten, K. Winer, and D. Weaire, Phys. Rev. Lett. **54**, 1392 (1985).

[12] N. Mousseau and G. T. Barkema, Phys. Rev. B **61**, 1898-1906 (2000).

[13] G. T. Barkema and N. Mousseau, Phys. Rev. Lett. **77**, 4358 (1996); G. T. Barkema and N. Mousseau, Phys. Rev. Lett. **81**, 1865 (1998).

[14] R. L. McGreevy, J. Phys.: Condens. Matter **13**, R877 (2001).

[15] D. A. Keen and R. L. McGreevy, Nature **344**, 423 (1990).

[16] R. L. McGreevy and L. Pusztai, Mol. Simul. **1**, 359 (1988).

[17] M. G. Tucker, M. T. Dove, and D. A. Keen, J. Appl. Cryst. **34**, 630 (2001).

[18] P. Biswas, R. Atta-Fynn, and D. A. Drabold, Phys. Rev. B **69**, 195207 (2004).

[19] P. Hohenberg and W. Kohn, Phys. Rev. B **136**,864 (1964); W. Kohn and L. J. Sham, Phys. Rev. **140** A, 1133 (1965).

[20] D. A. Drabold,*Electronic structure methods with applications to amorphous semiconductors*, M.F. Thorpe and M. I. Mitkova Eds, NATO Advanced Study Institute Series, Kluwer, Dordrecht 1997.

[21] O.F. Sankey and D.J. Niklewski, Phys. Rev. B **40**,3979 (1989); O.F. Sankey, D.A. Drabold, and G.B. Adams, Bull. Am. Phys. Soc. **36**,924 (1991).

[22] J.M. Soler, E. Artacho,J.D. Gale,J. Junquera, P. Ordejon and D. Sanchez-Portal, J. Phys. Cond. Matt. **14**, 2745 (2002) and references therein.

[23] J. Harris, Phys. Rev. B **31**, 1770 (1985).

[24] D. A. Drabold, in *Insulating and Semiconducting Glasses*, edited by P. Boolchand (world Scientific, Singapore, 2000), pp. 607-652.

[25] J. P. Lewis, K. R. Glaesman, G. A. Voth, J. Fritsch, A. A. Demkov, J. Ortega, and O. F. Sankey, Phys. Rev. B **64**, 195103 (2001).

[26] I. Petri and P. S. Salmon, Phys. Chem. Glasses, **43C** 185 (2002).

[27] M. Mitkova and M. N. Kozicki, J. Non. Cryst. Sol. **299** 1023 (2002).

[28] N.R. Rao, P.S.R. Krishna, S. Basu, B.A. Dasannacharya, K.S. Sangunni, and E.S.R. Gopal, J. Non-Cryst. Solids **240**, 221 (1998); N.R. Rao, K.S. Sangunni, E.S.R. Gopal, P.S.R. Krishna, R. Chakravarthy, and B.A. Dasannacharya, Physica B **213 & 214**, 561 (1995).

[29] Z. U. Borisova, *Glassy Semiconductors*, 1981, Plenum, New York.

[30] P. Vashishta, R.K. Kalia, J.P. Rino, and I. Ebbsjö, Phys. Rev. B **41**, 12197 (1990).

[31] C. Massobrio, A. Pasquarello, and R. Car, Phys. Rev. Lett. **80**, 2342 (1998); C. Massobrio, A. Pasquarello, and R. Car, Comput. Mater. Sci. **17**, 115 (2000a).

[32] S. Susman, K. J. Volin, D. G. Montague, and D. L. Price, J. Non-Cryst. Solids **125**, 168 (1990).

[33] W. Zhou, M. Pasesler, and D.E. Sayers, Phys. Rev. B **43**, 2315 (1991).

[34] G. Lucovsky, T.M. Hayes, *Amorphous Semiconductors*, edited by M.H. Brodsky, Springer, Berlin, 1979, p. 125.

[35] XMOL, version 1.3.1, 1993, Minnesota Supercomputer Center, Inc., Minneapolis, MN 55415.

[36] B. Effey and R.L. Cappelletti, Phys. Rev. B **59**, 4119 (1999).

[37] W.A. Kamitakahara, R.L. Cappelletti, P. Boolchand, B. Halfpap, F. Gompf, D.A. Neumann, and H. Mutka, Phys. Rev. B **44**, 94 (1991).

[38] S. Sugai, Phys. Rev. B **35**, 1345 (1987).

[39] P.M. Bridenbaugh, G.P. Espinosa, J.E. Griffiths, J.C. Phillips, and J.P. Remeika, Phys. Rev. B **20**, 4140 (1979).

[40] E. Bergignat, G. Hollinger, H. Chermette, and P. Pertosa, Phys. Rev. B **37**, 4506 (1988).

[41] S. Hino, T. Takaharshi and Y. Harada, Solid State Communi. **35**, 379 (1980).

[42] M. Schlüter, J.D. Joannopoulos, and M.L. Cohen, Phys. Rev. Lett. **33**, 89 (1974); N.J. Shevchik, J. Tejeda, M. Cardona, and D.W. Langer, Solid State Commun. **12**, 1285 (1973).

[43] S. B. Mamedov, N. D. Aksenov, L. L. Makarov, and Y. F. Batrakov, J. Non-Cryst. Solids **195**, 272 (1996).

[44] X. Feng, W. J. Bresser, and P. Boolchand, Phys. Rev. Lett. **78**, 4422 (1997).

[45] Y. Wang, O. Matsuda, K. Inoue, O. Yamamuro, T. Matsuo, and K. Murase, J. Non-Cryst. Solids **232-234**, 702 (1998).

[46] M. Mitkova, Y. Wang, and P. Boolchand, Phys. Rev. Lett. **19**, 3848 (1999).

[47] Y. Wang, M. Mitkova, D.G. Georgiev, S. Mamedov, and P. Boolchand, J.Phys.: Condens. Matter **15**, S1573-S1584 (2003).

[48] C.A. Angell, Ann. Rev. Phys. Chem. **43**, 693 (1992).

[49] M. Mitkova and M. N. Kozicki, J. Non-Cryst. Sol. **299-302**, 1023 (2002).

[50] A. Pradel, N. Kuvata, M. Ribes, J. Phys.: Condens. Matter **15**, S1561-S1571 (2003).

[51] A. Fischer-Colbrie, A. Bienenstock, P.H. Fuoss, M.A. Marcus, Phys. Rev. B **38**, 12388 (1988).

[52] A. Piarristeguy, M. Fontana and B. Arcondo, J. Non-Cryst. Sol. **332**, 1 (2003).

[53] J.H. Lee, A.P. Owens, S.R. Elliott, J. Non-Cryst. Sol. **164-166**, 139 (1993).

[54] J.M. Oldale, J. Rennie, and S.R. Elliott, Thin Solid Films **164**, 467 (1988).

[55] R. J. Dejus, D.J. Le Poire, S. Susman, K. J. Volin, and D. L. Price, Phys. Rev. B **44**, 11705 (1991).

[56] R. J. Dejus, S. Susman, K. J. Volin, D. G Montague, and D. L. Price, J. Non-Cryst. Sol. **143**, 162 (1992).

[57] J.D Westwood, P. Georgopoulos, and D.H. Whitmore, J. Non-Cryst. Sol. **107**, 88 (1988).

[58] D. M. Ceperley and B. J. Alder, Phys. Rev. Lett. **45**, 566 (1980).

[59] J. P. Perdew and A. Zunger, Phys. Rev. B **23**, 5048 (1981).

[60] N. Troullier and J. L. Martins, Phys. Rev. B **43**, 1993 (1991).

[61] M. Fuchs and M. Scheffler, Comput. Phys. Commun. **119**, 67 (1999).

[62] R. L. Cappelletti, M. Cobb, D. A. Drabold, W. A. Kamitakahara, Phys. Rev. B **52** 9133 (1995).

[63] Jun Li, D. A. Drabold, S. Krishnaswami, G. Chen, and H Jain, Phys. Rev. Lett. **88**, 046803 (2002).

[64] H. Iyetomi, P. Vashishta, and R. K. Kalia, J. Non-Cryst. Sol. **262**, 135 (2000).

[65] F.H.M. Van Roon, C. Massobrio, E. de Wolff and S.W. de Leeuw, J. Chem. Phys. **113**, 5425 (2000).

[66] Drabold *et al* have made several models of non-stoichiometric GeSeAg and GeAsSe glasses with "quench from the melt" and accurate density functional MD calculations with SIESTA and VASP (including gradient corrections). These models have been disappointing, with an unphysical concentration of defects.

[67] J. C. Phillips, J. Non-Cryst. Sol **34** 153 (1979); M. F. Thorpe, J. Non-Cryst. Sol. **57** 355 (1983).

[68] P. Biswas, D. N. Tafen, R. Atta-Fynn and D. A. Drabold, J. Phys. Cond. Matt. **16** S1573 (2004); P. Biswas, D. N. Tafen and D. A. Drabold, Phys. Rev. B **71** 054204 (2005).

[69] M. Kastner, Phil. Mag. **37**, 127 (1978).

[70] F.A. Cotton, G. Wilkinson, C.A. Morillo, and M. Bochmann, *Advanced Inorganic Chemistry*, edited by John Wiley & Sons, Inc., New York, 1999, Sixth Edition, p. 14.

[71] H. Fritzsche, Rom. J. of Physics **51**, 183 (1999).

[72] T. Uchino, J. D. Harrop, S. N. Taraskin and S. R. Elliott, Phys. Rev. B **71** 014202 (2005); J. D. Harrop, S. N. Taraskin and S. R. Elliott, Phys. Rev. E **66** 026703 (2002); **68** 019904 (2003).

[73] The authors note that for sharp features in k-space, a Fourier transform is a crude estimator for spatial correlations. By exploiting multi-resolution continuous wavelet transform methods (preceding reference), they are able to compute explicitly the real-space correlations for each of the major features in k-space. The code is available in the form of a Mathematica notebook from Flying Frog Consultancy (http://www.ffconsultancy.com)

[74] S. I. Simdyankin, M. Elstner, T. A. Niehaus, Th. Frauenheim and S. R. Elliott, cond-mat/0504207 (2005).

[75] M. Kawasaki, J. Kawamura, Y. Nakamura, and M. Aniya, Sol. State Ion. **123**, 259 (1999).

[76] D. Chandler, *Introduction to Modern Statistical Mechanics* (Oxford University Press, New York, 1987), pp.246-252.

[77] M. A Ureña, A. A. Piarristeguy, M. Fontana, B. Arcondo, Sol. State Ion. **176**, 505 (2005). Using the diffusion coefficient of Ag at room temperature and the parameters obtained by these authors, we extrapolate the diffusion coeffient of Ag at 1000 K, 800 K, 700 K, and 640 K. We obtained diffusion coefficient of the order 1/10 times the theoretical values for T=1000 and 640 K. In view of the short simulation times and small models, this is reasonably consistent with experiment.

[78] M. Gutenev, A. Tabolin, and T. Rykova, Phys. Chem. Glasses **17**, 36 (1991).

[79] J. C. Phillips, Rep. Prog. Phys. **59**, 1133 (1996).

[80] E. R. Weeks and D. A. Weitz, Phys. Rev. Lett. **89**, 095704 (2002).

[81] J. C. Phillips (private communication).

[82] S. Nakhmanson, 2001, Theoretical studies of amorphous and paracrystalline silicon *Dissertation* Ohio University, Athens, OH http://www.phy.ohiou.edu/ drabold/serge.

[83] D. N. Tafen, D. A. Drabold, Phys. Rev. B **68**, 165208 (2003).

[84] J. Li and D. A. Drabold, Phys. Rev. B **64**, 104206 (2001).

[85] Recent work by Jackson and coworkers has enabled quantification and identification of "building blocks" from computation of the Raman spectrum (not simply the vibrational DOS) in some SiSe and GeSe glasses. K.A. Jackson and S. Grossman, Phys. Rev. B **65**, 012202 (2002); *ibid* **60**, R14985 (1999).

[86] D. A. Drabold, J. Li, and D. N. Tafen, J. Phys.: Condens. Matter **15**, 1529 (2003).

[87] N. Mousseau, Private Communication.

[88] M. Chubynsky and M. F. Thorpe, in *Physics and Applications of Disordered Materials*, edited by M. Popescu (INOE, Bucharest, 2002), p. 229.

[89] R. L. C. Vink and G. T. Barkema, Phys. Rev. B **67**, 245201 (2003).

[90] I. Petri, P. S. Salmon and H.E. Fischer, Phys. Rev. Lett. **84**, 2413 (2000).

[91] P. S. Salmon and I. Petri, J. Phys.: Condens. Matter **15**, 1509 (2003).

[92] X. Zhang and D.A. Drabold, Phys. Rev. B **62**, 15695 (2000).

[93] M. Cobb, D. A. Drabold and R. L. Cappelletti, Phys. Rev. B **54**, 12162 (1996).

[94] R. W. Johnson, D. L. Price, S. Susman, M. Arai, T.I. Morrison and G.K. Shenoy, J. Non-Cryst. Solids **83**, 251 (1986).

[95] M. Celino, Ph.D. dissertation, Université Louis Pasteur Strasbourg, 2002.

[96] S. Susman, R.W. Johnson, D.L. Price, and K.J. Volin,*Defects in Glasses*, Mat. Res. Soc. Symp. Proc. N_o. 61, edited by F.L. Galeener, D.L. Griscom, and M.L. Weber (MRS, Boston, 1986),p.91.

[97] M. Celino and C. Massobrio, Phys. Rev. Lett. **90**, 125502 (2003).

[98] G.A. Antonio, R.K. Kalia, A. Nakano, and P. Vashishta, Phys. Rev. B **45**, 7455 (1992).

[99] M. Arai, D.L. Price, S. Susman, K.J. Volin, and U. walter, Phys. Rev. B **37**, 4240 (1988).

[100] J.E. Griffiths, M. Malyj, G.P. Espinosa, and J.P. Remeika, Phys. Rev. B **30**, 6978 (1984); M. Malyj, G.P. Espinosa, and J.E. Griffiths, *ibid.* **31**, 3672 (1985).

[101] M. Tenhover, M.A. Hazle, and R.K. Grasselli, Phys. Rev. Lett. **51**, 404 (1983); M. Tenhover, M.A. Hazle, and R.K. Grasselli, and C.W. Tompson, Phys. Rev. B **28**, 4608 (1983); M. Tenhover, R.S. Henderson, D. Lukco, M.A. Hazle, and R.K. Grasselli, Solid State Commun. **51**, 455 (1984).

[102] K. Jackson and S. Grossman, Phys. Rev. B **65**, 012206 (2001).

[103] K.S. Liang, J. Non-Cryst. Solids **18**, 197 (1975).

[104] P.A.V. Johnson, A.C. Wright and R.N. Sinclair, J. Non-Cryst. Solids **58**, 109 (1983).

[105] R.F. Pettifer, R. Dupree, I. Farnan, and U. Sternberg, J. Non-Cryst. Solids **106**, 408 (1988).

[106] R.L. Mozzi and B.E. Warren, J. Appl. Cryst. **2**, 164 (1969).

[107] P.G. Coombs, J.F. De Natale, P.J. Hood, E.K. McElfresh, R.S. Wortman, and J.F. Schackelford, Philos.Mag. **51**, L39 (1985).

[108] K. Vollmayr, W. Kob, and K. Binder, Phys. Rev. B **54**, 15808 (1996).

[109] M.J. Carpenter and D.L. Price,Phys. Rev. Lett. **54**, 441 (1985).

[110] C.T. Kirk, Phys. Rev. B **38**, 1255 (1988).

[111] F.L. Galeener and G. Lucovsky, Phys. Rev. Lett. **37**, 1474 (1976).

[112] A. Kucirková and K. Navrátil, Appl. Spectrosc. **48**, 113 (1994).

[113] B. Fischer, R.A. Pollak, T.H. DiStefano, and W. D. Grobman, Phys. Rev. B **15**, 3193 (1977).

[114] R.B. Laughlin, J.D. Joannopoulos, and D.J. Chadi, Phys. Rev. B **20**, 5228 (1979).

[115] J. Sarnthein, A. Pasquarello, and R. Car, Phys. Rev. Lett. **74**, 4682 (1995).

[116] H.R. Phillip, Solid State Commun. **4**, 73 (1966); J.Phys. Chem. Solid **32**, 1935 (1971).

[117] E. Loh, Solid State Commun. **2**, 269 (1964); G. Klein and H.U. Chun, Phys. Status Solidi B **49**, 167 (1972).

[118] P. Biswas, D.N. Tafen, R. Atta-Fynn, and D. A. Drabold, J. Phys.: Condens. Matter **16**, 1 (2004).

[119] M. M. J. Treacy, J. M. Gibson, Acta Cryst. A **52**, 212 (1996).

[120] G. T. Barkema and N. Mousseau, Phys. Rev. B **62**, 4985 (2000).

[121] G. Henkelman and H. Jonsson, J. Chem. Phys. **113**, 9978 (2000); G. Henkelman, B. P. Uberuaga, and H. Jonsson, J. Chem. Phys. **113**, 9901 (2000).

[122] It is possible that suitable gradient-based methods could provide more rapid convergence, a point we do not investigate here.

[123] K. Jackson, A. Briley, S. Grossman D.V. Porezag, and M.R. Pederson, Phys. Rev. B **60**, R14985 (1999).

[124] P. Boolchand, J. Grothaus, W.J. Bresser, and P. Suranyi, Phys. Rev. B **25**, 2975 (1982).

[125] S. Hosokawa, Y. Hari, I. Ono, K. Nishihara, M. Taniguchi, O. Matsuda, and K. Murase, J. Phys.: Condens. Matter **6**, L207 (1994).

[126] S.G. Louie, Phys. Rev. B **26**, 5993 (1982).

[127] W. Pollard, J. Non-Cryst. Solids **144**, 70 (1992).

[128] R. M. Martin, *Electronic Structure, Basic Theory and Practical Methods*, Cambridge University Press, Cambridge (2004). page 144.

[129] R.L. Cappelletti, M. Cobb, D.A. Drabold, and W.A. Kamitakahara, Phys. Rev. B **52**, 9133 (1995).

[130] M. F. Thorpe, D. J. Jacobs, M. V. Chubynsky, and J. C. Phillips, J. Non Cryst. Solids **266-269**, 872 (2000).

[131] X. Zhang, Ph.D. Dissertation, Ohio University (unpublished).

[132] L. Ouyang and W. Y. Ching, Phys. Rev. B **54**, R15594 (1996).

[133] N. Mousseau, Phys. Rev. B **56**, 14190 (1997).